

REPORT DOCUMENTATION PAGE

Form Approved
OMB No. 0704-0188

Public reporting burden for this collection of information is estimated to average 1 hour per response, including the time for reviewing instructions, searching existing data sources, gathering and maintaining the data needed, and completing and reviewing the collection of information. Send comments regarding this burden estimate or any other aspect of this collection of information, including suggestions for reducing this burden, to Washington Headquarters Services, Directorate for Information Operations and Reports, 1215 Jefferson Davis Highway, Suite 1204, Arlington, VA 22202-4302, and to the Office of Management and Budget, Paperwork Reduction Project (0704-0188), Washington, DC 20503.

1. AGENCY USE ONLY (Leave blank)		2. REPORT DATE May 1989	3. REPORT TYPE AND DATES COVERED Final, 01 SEP 86 - 30 NOV 88	
4. TITLE AND SUBTITLE COMPUTER AIDED DESIGN OF MONOLITHIC MICROWAVE AND MILLIMETER WAVE INTEGRATED CIRCUITS AND SUBSYSTEMS			5. FUNDING NUMBERS AFOSR-86-0339 2305/C1 611021F	
6. AUTHOR(S) PROFESSOR WALTER H. KU			7. PERFORMING ORGANIZATION NAME(S) AND ADDRESS(ES) University of California, San Diego LaJolla, CA 92093	
8. PERFORMING ORGANIZATION REPORT NUMBER AFOSR-TR-89-1266			9. SPONSORING/MONITORING AGENCY NAME(S) AND ADDRESS(ES) AFOSR/NE Building 410 Bolling AFB, DC 20332-6448 Dr Witt	
10. SPONSORING/MONITORING AGENCY REPORT NUMBER			11. SUPPLEMENTARY NOTES	
12a. DISTRIBUTION/AVAILABILITY STATEMENT APPROVED FOR PUBLIC RELEASE; DISTRIBUTION UNLIMITED			12b. DISTRIBUTION CODE DTIC SELECT 20728 1989	
13. ABSTRACT (Maximum 200 words) The objectives of this research are to develop analytical and computer-aided design techniques for monolithic microwave and millimeter-wave integrated circuits (MMIC & MIMIC) and subsystems and to design and fabricate those ICs. Emphasis was placed on heterojunction-based devices, especially the High Electron Mobility Transistor (HEMT), for both low-noise and medium-power microwave and millimeter-wave applications. Circuits to be considered include monolithic low-noise amplifiers, power amplifiers, and distributed and feedback amplifiers. Interactive computer aided design programs have been developed, which include large-signal models of InP MISFETs and InGaAs HEMTs. Further, a new unconstrained optimization algorithm-POSM has been developed and implemented in the general-purpose Analysis and Design program for Integrated Circuit (ADIC) for assistance in the design of large-signal non-linear circuits.				
14. SUBJECT TERMS			15. NUMBER OF PAGES 98	
16. PRICE CODE			17. SECURITY CLASSIFICATION OF REPORT UNCLASSIFIED	
18. SECURITY CLASSIFICATION OF THIS PAGE UNCLASSIFIED		19. SECURITY CLASSIFICATION OF ABSTRACT UNCLASSIFIED		20. LIMITATION OF ABSTRACT N/A

AD-A213 656

Computer Aided Design of Monolithic Microwave and Millimeter Wave Integrated Circuits and Subsystems

Professor Walter H. Ku

Department of Electrical and Computer Engineering

Mail Code R-007

University of California, San Diego

La Jolla, CA 92093

(619)534-2717

arpanet: ku@sdcsvax.ucsd.edu

AFOSR-TR-89-1266

Contract No. AFOSR-86-0339

Contract Monitor :

Dr. Gerald Witt

Approved For	
NTIC	<input checked="" type="checkbox"/>
EDIC	<input checked="" type="checkbox"/>
Unrestricted	<input type="checkbox"/>
Other	<input type="checkbox"/>

A-1

Final Technical Report

May 1989

Table of Contents

	Page
Abstract	3
I Introduction	4
II Computer-Aided Design	6
2.1 Device Modeling	6
2.1.1 Analytical Model	6
2.2.2 Numerical Model	7
2.2 Circuit Simulation and Optimization	9
III Device Fabrication	11
3.1 Material and Device Process	11
3.2 Device Results	12
IV Circuit Design	13
4.1 Design Approach	13
4.2 Design of Power Distributed Amplifier	15
V Summary and Recommendations	17
References	18
List of Figures	20
List of Tables	23
Appendix A	
Appendix B	
Appendix C	
Appendix D	
Appendix E	

Abstract

The objectives of this research are to develop analytical and computer-aided design techniques for monolithic microwave and millimeter-wave integrated circuits (MMIC & MIMIC) and subsystems and to design and fabricate those ICs. Emphasis was placed on heterojunction-based devices, especially the High Electron Mobility Transistor (HEMT), for both low-noise and medium-power microwave and millimeter-wave applications. Circuits to be considered include monolithic low noise amplifiers, power amplifiers, and distributed and feedback amplifiers. Interactive computer aided design programs have been developed, which include large-signal models of InP MISFETs and InGaAs HEMTs. Further, a new unconstrained optimization algorithm-POSIM has been developed and implemented in the general-purpose Analysis and Design program for Integrated Circuit (ADIC) for assistance in the design of large-signal nonlinear circuits.

We have developed an accurate analytical drain current-voltage characteristics model for HEMT devices based on the nonlinear charge-control formulation which describes the variable offset distance of the Two-Dimensional Electron Gas (2-DEG) from the heterointerface in a more consistent manner and with greater accuracy. The simplicity of this model makes it well suited for Computer-Aided Design (CAD) applications in the analysis and design of nonlinear HEMT devices and integrated circuits. In addition, we have developed a general-purpose finite-element two-dimensional semiconductor device simulation program, which is able to analyze and simulate various device structures including homo- and hetero-junction III-V compound semiconductor-based devices with arbitrary geometries.

The work also included the synthesis, growth, characterization and device prototype development employing $\text{In}_x\text{Ga}_{1-x}\text{As}$ ternary compound semiconductor material. Pseudomorphic InGaAs HEMTs with higher currents and therefore, improved power performance in the high frequency range are suitable for millimeter wave integrated circuit applications. Single heterojunction $\text{In}_{0.2}\text{Ga}_{0.8}\text{As}/\text{GaAs}$ and double heterojunction $\text{In}_{0.15}\text{Ga}_{0.85}\text{As}/\text{GaAs}$ HEMTs of 1 μm and .25 μm gate length have been fabricated. Currents up to 310 mA/mm and 510 mA/mm have been measured for the 1 μm single and double heterojunction devices. The 0.25 μm devices had a f_{max} of 85 GHz. Also reported are a new design technique for power distributed amplifiers using large-signal S-parameters from harmonic balance analysis and design examples of distributed amplifiers using the MESFET and HEMT devices.

I. Introduction

Due to their superior high frequency and high speed capabilities, III-V compound semiconductor-based devices appear to be very attractive for microwave and millimeter wave circuit applications. New fabrication techniques such as Molecular Beam Epitaxy, high-resolution Electron Beam Lithography, ... *etc.* allow novel high performance devices to be realized in the laboratory.

Computer aided design techniques have to keep abreast of the fabrication technology and precedes it, if possible, because the whole design must be made a priori and the circuit performance are simulated via CAD tools, if we adopt a monolithic integrated circuit approach. The computer-aided design of microwave circuit is now commonplace. Even though several commercial CAD packages are available, they are originally developed for the analysis of linear electronic circuit in the low frequency region and with limited number of device models available. Also those models are valid in a narrow operation range and are therefore limited in their applicability to the latest GaAs MMIC and MIMIC technology.

There is a growing demand for the improvement of the CAD tools available for the MMIC design and their further extensions to the applications for MIMIC design. In order to analyze MMIC's up to the millimeter-wave region, a simulator should be able to analyze a circuit design in terms of its topological and physical parameters including frequency dependence. The built-in device model of the circuit simulator should be accurate and simple in expressions even the non-linearity of the device characteristics is taken into account so that the circuit simulator could run efficiently.

The high electron mobility transistor, HEMT, has become an important device because of its high gain and performance at high frequencies. The pseudomorphic HEMT, based on the strained layer $\text{In}_x\text{Ga}_{1-x}\text{As}$ epitaxial material, in particular, has potential for being the device of choice for millimeter wave integrated circuit applications[1,2]. HEMTs employing InGaAs have higher frequency performance than the conventional AlGaAs/GaAs HEMT because of the higher electron mobility and velocity of the InGaAs compared with GaAs. The research presented is concerned with the growth of pseudomorphically strained $\text{In}_x\text{Ga}_{1-x}\text{As}/\text{GaAs}$ heterostructures and the tailoring of the composition and layer structure for HEMTs. Power performance of devices at high frequency will be an important issue for MMIC's. Prototype devices of $1\ \mu\text{m}$ and $0.25\ \mu\text{m}$ gate length, with higher currents have been fabricated and evaluated, showing the potential of these devices to meet these needs.

The distributed amplifier is based on the principles of the artificial transmission lines into which the input and output capacitances of an active device are absorbed, and then the gain-bandwidth product of the distributed amplifier can be increased. Using the pseudomorphic

InGaAs/GaAs devices reported here, several distributed amplifiers with very broad bandwidth were designed and simulated at UCSD.

II. Computer-Aided Design

With the increasing complexity in modern semiconductor device structures and integrated circuits, the use of computer programs have proven to be valuable aids in the design, development and characterization of new devices and integrated circuits. The process of CAD consists of three important segments, namely :

- I Component modeling
- II Circuit analysis
- III Optimization.

We will present the research results on these subjects in the following sections.

2.1 Device Modeling

Device modeling has played an important role in the computer analysis and simulation programs. Device models can be considered in two broad categories: analytical and numerical models. At present, the relative importance of analytical and numerical models is clearly established: the former are especially useful in circuit simulation programs, where computational efficiency is the main concern. The latter, instead, are being increasingly used for verification of analytical model and as design tools to predict the achievable performance of a new device which has not been fabricated. III-V compound semiconductor devices show great promise for use in high-performance integrated circuits. Accurate analytical modeling and numerical simulation of modern devices become quite involved and time consuming. Difficulties in the modeling of active devices have limited the use of CAD techniques at microwave and millimeter wave frequencies. To aid in understanding the physical operation of these devices and to optimize their design, accurate device models, especially for heterostructure-based devices, are required. The aim of this research is to develop simple and accurate analytical models and efficient numerical models for III-V compound semiconductor devices, which can help in design, characterization, and optimization of high-frequency microwave and high-speed digital integrated circuits.

2.1.1 Analytical model

A CAD-oriented analytical model usually contains several parameters which can be adjusted by fitting experimental data; so doing, reasonable accuracy can be achieved. However, the inadequacies of the model may be compensated by data fitting process and those parameters can hardly be traced back to their physical meaning. Thus, in order to link device performance to

the process parameters, simple models based on device physics with a minimum number of fitting parameters are more desirable. In other words, a device model suitable for MIMIC design and optimization should encompass the following features : (1) It should include the effects of process-related device parameters (dimensions, material parameters, doping profile, channel thickness, recess depth, etc.). Device-circuit interactions play an important role and can not be ignored. (2) Device models must be computationally efficient to allow for simulation of circuits in an economic fashion. (3) The model must provide the circuit designer with synthesis capability. (4) The device model must have nonlinear capability. From this point of view, we have improved the charge control models for HEMTs and MISFETs by taking the nonlinear variation into account, and which resulted in more accurate drain current-voltage characteristics models.

A. HEMT (High Electron Mobility Transistor)

The analytical models most widely used for characterizing HEMT performance are based on the linear charge control model which either neglects the variation of Fermi potential with the applied bias or assumes a constant correction distance to account for the quantization effect in the direction normal to the heterointerface plane. We have developed a simple and more accurate nonlinear charge control model [3] (see Appendix A), derived from the triangular potential well approximation. Based on the analytical nonlinear charge control formulation, we further developed an analytical HEMT drain current-voltage characteristics model [4] (see Appendix B), with which the gain compression phenomena near the pinchoff regime and the high parasitic MESFET conduction are more accurately described. Moreover, the simple and analytical form of the model expression make it very suitable for CAD applications.

B. MISFET (Metal-Insulator-Semiconductor Field-Effect Transistor)

As compared with the empirically optimized Si-SiO₂ interface, compound semiconductor I-S interfaces are generally characterized by high density of interface states with a non-uniform distribution within the energy band gap. To obtain more accurate description of the modulation of surface potential by external bias, a simple empirical distribution of interface states within energy band gap is included in the charge control formulation. The results show that the inclusion of interface states distribution profile into drain I-V characteristics model leading to a more accurate description of output characteristics of III-V MISFETs [5] (see Appendix C).

2.1.2 Numerical model

As device configuration and fabrication process steps become complicated, the analytical approach is limited in its accuracy for describing two-dimensional structures, such as recessed

gate transistors, or small-scale devices where fringing fields and other multi-dimensional effects predominate. Accordingly, numerical models are necessary, and which can serve as (1) an aid for a deeper understanding of device behavior, (2) an aid for the development and validation of CAD-oriented analytical models, (3) a predictive design tool for device performance optimization. We have developed a simple and feasible finite element discretization method [6] (see Appendix D) consistent with the exponentially fitted Scharfetter-Gummel scheme for variation of carrier densities, in our general-purpose two-dimensional Semiconductor Device Analysis program (SDA). Recently, we have extended the application of SDA program to the simulation of III-V compound semiconductor devices, including homojunction and heterojunction. The simulation results of two example devices of

A. HEMT (High Electron Mobility Transistor)

B. MESFET (Metal-Semiconductor Field-Effect Transistor)

are reported. The simulated distributions of potential and carrier confirmed the validity of the assumption of nonlinearity in the charge control formulation used in the analytical I-V model.

Two-Dimensional Finite-Element Models for HEMT and MESFET Devices

High electron mobility transistors are becoming increasingly important for the provision of superior high gain, high performance devices for microwave and millimeter-wave applications. To increase the transconductance g_m and cutoff frequency f_t , device geometries must be scaled. The future trend is to reduce the minimum feature size down to deep submicrometer dimensions. As the feature size is scaled to this range, careful consideration of short channel effects and hot carrier effects in the conduction channel is crucial. To this end, a better understanding and analysis of device operation is necessary for the successful development of device and accurate prediction of its performance. Two-dimensional numerical device models are suitable for investigating the details of intrinsic complex nonlinear characteristics in the scaled devices.

To date, papers published on full two-dimensional models for HEMT devices are very few [7-11]. In addition, these models are restricted to finite-difference methods, which are not applicable for simulating irregular structures such as recessed gate structures commonly used in the enhancement-mode HEMT devices.

Recently, we have successfully developed a general-purpose semiconductor device simulator, which is capable of simulating various device structures with arbitrary geometries, based on new finite-element discretization employing the Scharfetter-Gummel (S-G) scheme [6]. By means of this device simulator we have developed two-dimensional numerical models for HEMT and MESFET devices following the formulation for heterostructure in [12].

To demonstrate the effectiveness and accuracy of the new two-dimensional model, the simulation results of a 1 μm AlGaAs/GaAs depletion-mode HEMT device are first reported. The simulated DC current-voltage characteristics of the HEMT device, whose geometric structure and simulation mesh are shown in Fig. 1 respectively, is plotted in Fig. 2. It is obvious that the gate current plays an important role in the forward gate bias region, where in the low drain bias region the source current dominates and shows a thermionic emission current, which is suppressed in the reverse bias region. The potential and electron distribution plots are shown in Fig. 3 and Fig. 4. From the distribution plots we can see the existence of two-dimensional electron gas at the heterointerface due to the conduction band discontinuity, and its being pinched-off by the drain bias resulting in the current saturation. The next simulated device is an MESFET device with gate length of 0.7 μm , whose device dimensions and simulation mesh are shown in Fig. 5. The resulting DC drain I-V characteristics are shown in Fig. 6. Fig. 7 and Fig. 8 illustrate the potential and electron density in the device at various drain voltages, respectively.

In these new models, we have also included the energy equation to take short-channel effects and hot carrier effects into account. It is planned to extend the two-dimensional numerical model to the modeling of submicron gate length InGaAs-based pseudomorphic HEMTs and AlGaAs/InGaAs

2.2 Circuit Simulation and Optimization

As to softwares for microwave and millimeter-wave circuit design applications, we have an in-house program called NODAL for the analysis and optimization of linear high-frequency analog circuits and the commercial package TOUCHSTONE from EEsos for the same purposes. To design nonlinear large-signal circuits, we have CADNON program, which is an in-house general-purpose time-domain simulation and analysis program based on state-variable method for microwave nonlinear passive and active circuits. In addition, we have successfully ported the SPECTRE frequency-domain simulator for nonlinear circuits to Apollo workstations in our CAD laboratory. The SPECTRE, developed by U. C. Berkeley CAD group, uses the harmonic balance approach to find the large-signal response of a nonautonomous nonlinear circuit. Since we have source codes of these simulators, we can tailor these programs for our uses by incorporating our new device models.

Circuit optimization is an important stage during the design. Chen [13] has developed an effective optimization algorithm suitable for integrated circuit design. However, the resort to linear search is still frequent in Chen's method and the amount of iterations is huge. We have developed a new unconstrained optimization algorithm using the Pseudo Objective Function Substitution method (POSM) [14] (see Appendix E). This algorithm, requiring neither derivative

calculation nor linear search step, substitutes the objective function by a second-order approximated formulation, which enhances the convergence rate substantially. The algorithm has been implemented in the general-purpose analysis and design program (ADIC-2.C) for integrated circuit.

III. Device Fabrication

3.1 Material and Device Process

In addition to the higher electron mobility and velocity of InGaAs, the advantages for using i.e. InGaAs pseudomorphic HEMT are that the use of AlGaAs can be avoided or at least used with a low Al percentage (less than 20%). Because InGaAs has a smaller bandgap than GaAs, the ΔE_C , conduction band edge discontinuity, is comparable or greater than that for AlGaAs/GaAs HEMTs. As a result, the problems associated with trapping centers in AlGaAs of higher Al percentage, needed to achieve higher ΔE_C , can be reduced. Also, the wider bandgap of GaAs creates a barrier at the interface between the InGaAs and GaAs buffer and substrate. This serves to improve confinement of electrons to the InGaAs, reducing parasitic conduction or backgating through the buffer or substrate.

In order to achieve higher current gain cutoff frequencies, f_t , and increased currents, which will improve power performance for these transistors, it is desirable to increase the sheet carrier density, n_s , without degrading the electron mobility μ . This can be achieved through increasing the conduction band discontinuity, ΔE_C , by reducing the fundamental bandgap of the $\text{In}_x\text{Ga}_{1-x}\text{As}$, with larger fractional indium concentrations, x . Increasing ΔE_C also decreases the real space charge transfer back into the lower mobility doped layer. An increase in x can lead to higher electron mobility, but this may be offset by electron-electron scattering due to a larger n_s . There will also be a greater lattice mismatch, resulting in a larger strain so the thickness must be reduced below the critical thickness for the generation and displacement of dislocations at the heterojunction.

An alternative approach to increasing the sheet carrier concentration is to employ a double heterojunction. With a highly doped layer both above and below the active channel, charge transfer can occur from both sides. This is more feasible with pseudomorphic InGaAs HEMTs because the quality of the interface between InGaAs on top of GaAs is better than that of GaAs on top of AlGaAs. Results will be presented on 1 μm and 0.25 μm gate length single heterojunction $\text{In}_{0.2}\text{Ga}_{0.8}\text{As}/\text{GaAs}$ HEMT and double heterojunction $\text{In}_{0.15}\text{Ga}_{0.85}\text{As}/\text{GaAs}$ HEMT.

The $\text{In}_x\text{Ga}_{1-x}\text{As}$ is lattice mismatched to GaAs, so its thickness and composition must be chosen so that it is elastically distorted relative to its GaAs substrate thus insuring an essentially defect free heterojunction interface. It is advantageous that HEMTs be developed on GaAs substrates because they are of significantly better quality than InP substrates and are compatible with current MMIC technology. The layer thickness of the $\text{In}_{0.2}\text{Ga}_{0.8}\text{As}$ is only 135 angstroms. HEMT structures were grown with 25% and 30% In fractions, but the 1 μm devices that were fabricated had inferior performance suggesting that on a GaAs buffer, using InGaAs with In percentage

much above 20% may not be feasible due to the increased lattice mismatch and the layer thickness required to prevent dislocations.

The electron donor layer of the devices is n type GaAs, avoiding any difficulties that may exist with using AlGaAs. The doping is $2.3 \times 10^{18}/\text{cm}^3$ from Hall effect measurements. The layer structure of the single and double heterojunction device are shown in Fig. 9(a) and 9(b). The 1 μm gate length devices had gate widths of 50 μm and 150 μm . The device fabrication involves mesa isolation, AuGeNi ohmic contacts, a wet chemical gate recess, and TiAu gates. The 0.25 μm gates were fabricated on wafer by direct write electron beam lithography at the TRW facilities in Redondo Beach, CA.

3.2 Device Results

A comparison of the current levels of the 1 μm gate single heterojunction $\text{In}_{0.2}\text{Ga}_{0.8}\text{As}/\text{GaAs}$ device and the double heterojunction $\text{In}_{0.15}\text{Ga}_{0.85}\text{As}/\text{GaAs}$ device with the single heterojunction $\text{In}_{0.15}\text{Ga}_{0.85}\text{As}/\text{GaAs}$ device done in earlier work are favorable. The peak current of the $\text{In}_{0.2}\text{Ga}_{0.8}\text{As}/\text{GaAs}$ HEMT was 310 mA/mm, nearly 25% better than the 250 mA/mm found for the $\text{In}_{0.15}\text{Ga}_{0.85}\text{As}/\text{GaAs}$ HEMT. The double heterojunction HEMT had peak current values of up to 510 mA/mm, which indicate that charge transfer is occurring across both interfaces. These current values are taken near the peak transconductance values.

To achieve higher frequencies, HEMTs must go to submicron gate lengths. $\text{In}_{0.2}\text{Ga}_{0.8}\text{As}/\text{GaAs}$ HEMT's of 0.25 μm gate length have length have been fabricated by UCSD with a g_m of up to 500 mS/mm. One device on which s-parameter measurements were made (up to 26 GHz) had an extrapolated maximum frequency of oscillation, f_{max} , of 85 GHz and current gain cutoff frequency, f_t , of 40 GHz. The maximum available gain (stability factor $k > 1$) at 26 GHz was 10.6 dB. An example of the well behaved dc characteristics of these devices is shown in Fig. 10 and a plot of the maximum available gain is presented in Fig. 11. One feature found on many of the devices has been a broad transconductance curve. This will improve the operating range of the devices. Double heterojunction $\text{In}_{0.15}\text{Ga}_{0.85}\text{As}/\text{GaAs}$ HEMT's with 0.25 μm gate have exhibited peak currents of 430 mA/mm, and a g_m of 350 mS/mm. A f_{max} of 75 GHz and f_t of 50 GHz were extrapolated from measurements on one device. The increase in f_t reflects the higher current of the device. The dc characteristics are shown in Fig. 12 and the plot of maximum available gain is found in Fig. 13.

IV. Circuit Design

4.1 Design Approach : A Systematic Approach to Design of Distributed Amplifier

The idea behind the design of distributed amplifier is to avoid the input and output capacitances of active devices being frequency limiting parasitics by incorporating these capacitances into the per-unit-length capacitance of the artificial transmission lines which serially connect all the input ports and all the output ports together in a distributed manner. The topology of a distributed amplifier is shown in Fig. 14. This approach allows the gain of active device to be paralleled without the corresponding paralleling of the device input and output capacitances, and, thus, enhances the overall gain-bandwidth product. Previously we developed analytical and computer aided design techniques for broadband high frequency distributed FET amplifier design, and implemented in the analysis and design program (DFETA) [16]. The approach employed in the DFETA program can be summarized as follows. For simplicity, a unilateral simplified model of FET is adopted. The gate transmission line is modeled by cascaded lumped low-pass filter sections which have the same characteristic impedance and cutoff frequency as that of the gate transmission line. Because of the very small drain capacitance, C_d , of FET, the corresponding characteristic impedance of the drain transmission line is too large for a realistic design of output matching circuit. We included a series inductance to C_d to construct the equivalent m -derived low-pass filter sections which emulated the drain transmission line with the same characteristic impedance and cutoff frequency of the drain transmission line. The m -derived drain transmission line can match the impedance at the output port of the circuit easily. Gain response of a DFETA can be estimated from the normalized gain curves generated by the DFETA program with the normalization parameters ($\tau_g = R_g \cdot C_g \cdot f_c$, $\tau_d = R_d \cdot C_d \cdot f_c$, and $f_n = f/f_c$). After these normalized design parameters are adjusted to achieve the desired or optimal flat gain response, we can determine the real circuit design from those parameters.

In DFETA, the characteristic impedances of gate and drain transmission line and the DC voltage gain can be expressed as follows :

$$Z_g = \frac{1.0315}{\pi f_{cg} C_g} \quad (1)$$

$$Z_{dm} = \frac{m}{\pi f_{cd} C_d} \quad (2)$$

$$V_{\text{Gain(DC)}} = \frac{1}{2} N_{g_m} (Z_g Z_{dm})^{1/2} \quad (3)$$

where

f_{cg} : the cutoff frequency of the gate transmission line

f_{cd} : the cutoff frequency of the drain transmission line

m : the m -derived parameter ($m < 1$)

C_g : the gate capacitance in the simplified model

C_d : the drain capacitance in the simplified model

g_m : the transconductance used in the simplified model

N : the number of FET devices used in the circuit

And the corresponding lumped element values can be expressed as

$$L_g = \frac{1.1474}{1.0315} \cdot Z_g^2 \cdot \frac{C_g}{2} \quad (4)$$

$$L = \frac{Z_{dm}}{\pi f_{cd}} \quad (5)$$

$$L_d = mL \quad (6)$$

$$L_{dm} = \frac{1 - m^2}{m} L \quad (7)$$

The lumped inductance can be introduced by using microstrips whose size can be determined by the following formula under the assumption that the size is much smaller than the quarter wave length at the operating frequency [17].

$$l = L \cdot v_p Z_0 \quad (8)$$

where

l : the microstrip length

L : the value of inductance L_g , L_d , or L_{dm}

Z_0 : the characteristic impedance of the microstrip

v_p : the propagation velocity of signal in the microstrip

Although we can always obtain a set of normalized design parameters for a specified or optimal gain response from the simulation results, it may not be practical for those components to be realized in a monolithic chip. For instance, we have to keep the active devices as far as possible away from each other, e.g. 300 μm , because the coupling effects among those active devices is a big concern when it comes to the monolithic IC design. However, from equation (1)-(3), it is apparent that increase in the bandwidth of a distributed amplifier will cause a reduction in both the characteristic impedances of the gate and drain transmission lines, consequently a reduction in the length of microstrip. In order to avoid unrealistic design, we developed a systematic approach to designing broadband distributed amplifier which takes the realizability in a

monolithic chip into consideration.

First, we derived the equation governing the characteristic impedance, the lumped inductance and the physical microstrip sizes of the gate and drain lines. Some example cases are derived and listed in Table I and Table II, respectively, where the L_{dm} values are omitted because it is not important as far as the realizability is concerned.

As seen from the data listed in Table I and Table II, there are restrictions imposed on the design of distributed amplifier due to the consideration of realizability. The results indicate that the DC gain can not be set as low as we wish. There is constraint on the minimum DC gain. So is the maximum bandwidth of a reasonable design. The active devices employed in our design are 0.15 μm pseudomorphic InGaAs/GaAs HEMTs which were fabricated and measured by TRW. Their small-signal equivalent circuit model and de-embedded model are shown in Fig. 15(a) and 15(b), respectively. Based on the de-embedded model, we further derive its simplified unilateral model as shown in Fig. 15(c). Referring the data in Table I and II, we use DFETA simulation program to evaluate the gain performance of the distributed amplifier design where we used four HEMTs. The best results of the distributed amplifier design using uniform gate and drain transmission lines are shown in Fig. 16. We further incorporated the tapered gate and drain lines into the DFETA simulation program in order to enhance design flexibility and to optimize the gain response, in which we set the source and load impedances of the distributed amplifier as 50 ohms. The best results of the distributed amplifier with tapered lines are shown in Fig. 16. To verify the design, we analyzed the distributed amplifier with tapered lines by the TOUCHSTONE analysis/optimization program from EEsof, where the de-embedded model, instead of the simplified model, was used. The results are shown in Fig. 17, also shown are the results after partial optimization. The results show the gain is 9.5 dB and the bandwidth is 40 GHz of the lumped distributed amplifier. Finally, we converted the lumped inductances into microstrip design on a GaAs substrate with thickness of 100 μm . The analysis results of the initial microstrip design are shown in Fig. 18, also shown are the results after partial optimization. The gain is about 8.5 dB and the bandwidth is 42 GHz. The resultant sizes of microstrips and other element values are listed in Table III.

4.2 Power Distributed Amplifier Design

We further extended the application of the systematic approach of distributed amplifier design to the design of power distributed amplifier. Because the operation region of the power device may include the nonlinear region, the S-parameter measured under the large-signal condition is a function of the input drive power. In [18], we have investigated the validity of applying conventional large-signal S-parameter in distributed amplifier design by harmonic balance

analysis. We found that the input drive power level plays an important role in determining the frequency range within which the large-signal S-parameter can be applied in the power amplifier design without causing severe discrepancy.

A nonlinear FET model was used in our initial power distributed amplifier design. The model is shown in Fig. 19(a). The DC characteristics of this nonlinear FET model are shown in Fig. 19(b). The DC operating point of the FET device is at gate bias of 0.0 volt and drain bias 4.0 volts. The large-signal S-parameter beyond 6 GHz derived at 9 dBm RF input power drive was shown to be valid in [18]. The corresponding simplified large-signal model is shown in Fig. 20. Following the systematic approach of distributed amplifier design proposed in the preceding section, we evaluated the power performance of the power distributed amplifier by DFETA program using the simplified large-signal model. The results are shown in Fig. 21 with a comparison with the results derived by Touchstone using the large-signal S-parameter rather than the simplified model. The complete microstrip design of the power distributed amplifier converted from the lumped element design, including the bias circuit, is shown in Fig. 22. The optimized output performance estimated by Touchstone is shown in Fig. 23. To evaluate the sensitivity of the power performance of the distributed amplifier design to the input RF power drive, the SPECTRE, a simulation program based on harmonic balance method, was used. The output power responses at various input drive power levels are shown in Fig. 24, where the curve with 0 dBm input power drive shows the power gain at normal or small signal operation. In Fig. 24, the curves with input drive power lower than 10 dBm indicates the device operates in the linear region. As seen from Fig. 24, there is a significant discrepancy between the power gains below 6 GHz under normal operation condition estimated by SPECTRE and calculated by Touchstone. It can be well explained that below 6 GHz the large-signal S-parameter derived at 9 dBm input power drive are no longer accurate to be applied in the broadband amplifier design, since their higher-order harmonics are too large to be assumed negligible [18]. However, higher than 6 GHz the power gain calculated by SPECTRE is almost the same as that estimated by Touchstone. The 1 dB compression points at each frequency are shown in Fig. 25, which indicates the maximally useful large-signal operation of a power distributed amplifier. These preliminary results confirmed the applicability of the proposed systematic design approach of distributed amplifier to the power distributed amplifier design by incorporating the method of deriving the accurate large-signal S-parameter by harmonic balance analysis.

V. Summary and Recommendations

Analytical and numerical device models for III-V compound semiconductor FETs have been developed. By consideration of the nonlinearity of charge control mechanism, the analytical models were able to describe the general shape of the I-V characteristics more accurately without introducing additional fitting parameters. We will further be concerned with the derivation of an appropriate gate capacitance-voltage characteristics model taking into account the nonlinear variation of channel charge with the applied electrical field and its frequency. The two-dimensional numerical models will be finished. Then the short channel devices will be investigated to further extend the applicability of the numerical model to simulation of the hot carrier effects which can not be modeled accurately by analytical approach. Also, the power performance of those devices will be evaluated.

The initial results are very encouraging for the use of pseudomorphic InGaAs HEMT's in millimeter wave integrated circuits. With $\text{In}_{0.15}\text{Ga}_{0.85}\text{As}/\text{GaAs}$ HEMT material grown at UCSD, TRW fabricated $0.15\ \mu\text{m}$ gate length HEMT with a maximum frequency of oscillation, f_{max} , of 125 GHz and a current cutoff frequency, f_t , of 75 GHz. $\text{In}_{0.2}\text{Ga}_{0.8}\text{As}/\text{GaAs}$ HEMT's of $0.25\ \mu\text{m}$ gate length have been fabricated by UCSD with a g_m of 500 mS/mm and f_{max} of up to 88 GHz. Double heterojunction $\text{In}_{0.15}\text{Ga}_{0.85}\text{As}/\text{GaAs}$ HEMT's with $0.25\ \mu\text{m}$ gate have exhibited a current of 550 mA/mm, a g_m of 320 mS/mm and f_{max} of 75 GHz. The next step will be fabrication of wide gate devices for increasing the current output of these pseudomorphic HEMT's for use as power amplifiers. Airbridges will be used for the interconnections.

Work in design method for distributed amplifier has come up with a new design technique for power distributed amplifiers using large-signal S-parameter derived from harmonic balance analysis. The initial designs of power distributed amplifiers using the pseudomorphic HEMT devices have shown excellent performance. The application of the new design technique to the design of distributed amplifier operating at millimeter-wave frequencies is under way.

References

- [1] P.C. Chao, et al., "0.1 micron Gate-Length Pseudomorphic HEMTs," *IEEE ELECTRON DEVICE LETTERS*, vol. EDL-8, pp. 489-491, Oct. 1987.
- [2] T. Henderson, et al., "Microwave Performance of a quarter micron gate low noise pseudomorphic InGaAs/AlGaAs modulation doped field effect transistor," *IEEE ELECTRON DEVICE LETTERS*, vol. EDL-7, pp. 649-651, Dec. 1986.
- [3] A.-J. Shey and W. H. Ku, "On the Charge Control of the Two-Dimensional Electron Gas for Analytic Modeling of HEMT's," *IEEE Electron Device Letters*, vol. 9, pp. 624-626, 1988.
- [4] A.-J. Shey and W. H. Ku, "An Analytical Current-Voltage Characteristics Model for the High Electron Mobility Transistors Based on Nonlinear Charge Control Formulation," accepted for publication in *IEEE Trans. Electron Devices*.
- [5] A.-J. Shey, W. H. Ku, and L. Messick, "Analytical and Computer-Aided Models of InP-Based MISFETs and Heterojunction Devices," *Joint NOSC/NRL InP Microwave/Millimeter Wave Technology Workshop*, San Diego, CA, January 25-26, 1989.
- [6] G.-L. Tan, X.-L. Yuan, Q.-M. Zhang, W. H. Ku, and A.-J. Shey, "Two-Dimensional Semiconductor Device Analysis Based on New Finite-Element Discretization Employing the S-G Scheme," *IEEE Trans. Computer-Aided Design*, vol. 8, pp. 468-478, 1989.
- [7] D. Widiger, K. Hess, and J. J. Coleman, "Two-Dimensional Simulation of the High Electron Mobility Transistor," *IEEE ELECTRON DEVICE LETTERS*, vol. EDL-5, pp. 266-269, 1984.
- [8] J. Yoshida and M. Kurata, "Analysis of High Electron Mobility Transistors Based on a Two-Dimensional Numerical Model," *IEEE ELECTRON DEVICE LETTERS*, vol. EDL-5, pp. 508-510, 1984.
- [9] Jeffrey Yuh-Fong Tang, "Two-Dimensional Simulation of MODFET and GaAs Gate Heterojunction FET's," *IEEE Trans. on Electron Devices*, vol. ED-32, pp. 1817-1823, 1985.
- [10] Dany Loret, "Two-Dimensional Numerical Model for the High Electron Mobility Transistor," *Solid-State Electronics*, vol. 30, pp. 1197-1203, 1987.
- [11] F. A. Buot, "Two-Dimensional Numerical Modeling of HEMT Using An Energy Transport Model," *COMPEL*, vol. 6, pp. 45-52, 1987.
- [12] Mark S. Lundstrom and Robert J. Schuelke, "Numerical Analysis of Heterostructure Semiconductor Devices," *IEEE Trans. on Electron Devices*, vol. ED-30, pp. 1151-1159, 1983.

- [13] R. M.-M. Chen, "A least pth optimization algorithm without calculating derivatives," *IEEE Trans. Circuits and System*, vol. CAS-28, pp. 331-337, 1981.
- [14] G.-L. Tan, S.-W. Pan, W. H. Ku, and A.-J. Shey, "ADIC-2.C: A General-Purpose Optimization Program Suitable for Integrated Circuit Design Applications Using the Pseudo Objective Function Substitution Method," *IEEE Trans. Computer-Aided Design*, vol. 7, pp. 1150-1163, 1988.
- [15] L. Messick et al., "High-Power High-Efficiency Stable Indium Phosphide MISFETs," *Proc. of the IEDM*, pp. 767-770, 1986.
- [16] W. H. Ku and J. Q. He, "Analysis and Design of Monolithic Distributed GaAs MESFET Amplifiers," *IEEE Cornell Conf. on High Speed Semiconductor Devices and Circuits*, Cornell Univ., pp. 80-92, Aug. 1983.
- [17] G. Matthaei, L. Young, and E. M. T. Jones, *Microwave Filters, Impedance-Matching Networks, and Coupling Structure*, New York: Graw-Hill, 1964.
- [18] S.-T. Chen and W. H. Ku, "Design of Power Distributed Amplifier Using Large-Signal S-Parameters from Harmonic Analysis," unpublished.

List of Figures

- Fig. 1 The geometric structure and the simulation mesh of a typical 1 μm HEMT device used in the two-dimensional simulation.
- Fig. 2 The simulated DC current-voltage characteristics of the HEMT device by our two-dimensional semiconductor device simulation program (SDA).
- Fig. 3 The simulated potential distribution plots of the HEMT device at zero gate bias and various drain voltages.
- Fig. 4 The simulated electron distribution plots of the HEMT device at zero gate bias and various drain voltages. The existence of the 2-DEG is obvious in this plot.
- Fig. 5 The geometric structure and the simulation mesh of a 0.7 μm MESFET device simulated by SDA.
- Fig. 6 The simulated DC current-voltage characteristics of the MESFET device.
- Fig. 7 The simulated potential distribution plots of the MESFET device at zero gate bias and various drain voltages.
- Fig. 8 The simulated electron distribution plots of the MESFET device at zero gate bias and various drain voltages.
- Fig. 9 (a) Layer structure of single heterojunction $\text{In}_{0.2}\text{Ga}_{0.8}\text{As}/\text{GaAs}$ HEMT. (b) Layer structure of double heterojunction $\text{In}_{0.15}\text{Ga}_{0.85}\text{As}/\text{GaAs}$ HEMT.
- Fig. 10 DC characteristics of the single heterojunction $\text{In}_{0.2}\text{Ga}_{0.8}\text{As}/\text{GaAs}$ HEMT.
- Fig. 11 Maximum available gain versus frequency for a 0.25 μm gate single heterojunction $\text{In}_{0.2}\text{Ga}_{0.8}\text{As}/\text{GaAs}$ HEMT.

Fig. 12 DC characteristics of the double heterojunction $\text{In}_{.15}\text{Ga}_{.85}\text{As}/\text{GaAs}$ HEMT.

Fig. 13 Maximum available gain versus frequency for a $0.25 \mu\text{m}$ gate double heterojunction $\text{In}_{.15}\text{Ga}_{.85}\text{As}/\text{GaAs}$ HEMT.

Fig. 14 The topology of a distributed amplifier built in the DFETA simulation program [16].

Fig. 15 (a) The small-signal equivalent circuit model, (b) the de-embedded model, and (c) the simplified unilateral model of a $0.15 \mu\text{m}$ pseudomorphic $\text{InGaAs}/\text{GaAs}$ HEMT.

Fig. 16 The estimated gain performance by DFETA program of the distributed amplifier employing ideal uniform gate and drain transmission lines and that employing the tapered gate and drain transmission lines.

Fig. 17 The output performances of the initial design and the optimized design by Touchstone of the distributed amplifier with tapered lines where the de-embedded model instead of the simplified model is used.

Fig. 18 The output performances of the initial design and the optimized design of the distributed amplifier with realizable microstrip sizes. The element values are listed in Table III.

Fig. 19 (a) Nonlinear FET model where $C_{gs0} = 1.05 \text{ pF}$, $C_{gd0} = 0.02 \text{ pF}$, $C_{ds} = 0.105 \text{ pF}$, $R_s = 0.73 \Omega$, $R_d = 0.73 \Omega$, $R_g = 1.17 \Omega$. (b) The simulated DC characteristics of the nonlinear FET model where $V_{t0} = -1.308$, $\text{Beta} = 0.035$, $\text{Alpha} = 2.382$, $\text{Lambda} = 0.0809$, $B = 0.0$.

Fig. 20 The simplified large-signal model at 9 dBm RF signal drive power.

Fig. 21 The output performance of the distributed amplifier design estimated by DFETA using the simplified large-signal model and that calculated by Touchstone using the large-signal S-parameter instead of the simplified model.

Fig. 22 Schematic diagram of a distributed amplifier employing microstrips and including the bias circuitry.

Fig. 23 The estimated output performance of the optimized distributed amplifier design using the large-signal S-parameter.

Fig. 24 Output power responses as a function of RF input power level.

Fig. 25 A plot of the 1 dB compression points of the power distributed amplifier.

List of Tables

- Table I The conversion table of the gate inductance into a high impedance microstrip line. The width of microstrip line is $18 \mu\text{m}$ on a semi-insulating GaAs substrate with thickness of $100 \mu\text{m}$. Z_g is the characteristic impedance of the gate transmission line used in DFETA [16], and L_g is the corresponding lumped inductance in the simplified low-pass filter section of the gate line.
- Table II The conversion table of the drain inductance into a high impedance microstrip line. The width of microstrip line is $18 \mu\text{m}$ on a semi-insulating GaAs substrate with thickness of $100 \mu\text{m}$. Z_d is the characteristic impedance of the drain transmission line used in DFETA [16], and L_d is the corresponding lumped inductance in the simplified low-pass filter section of the m-derived drain line.
- Table III The sizes of microstrips and other element values of the distributed amplifier whose output performance shown in Fig. 18. The elements refer to the circuit topology in Fig. 14.

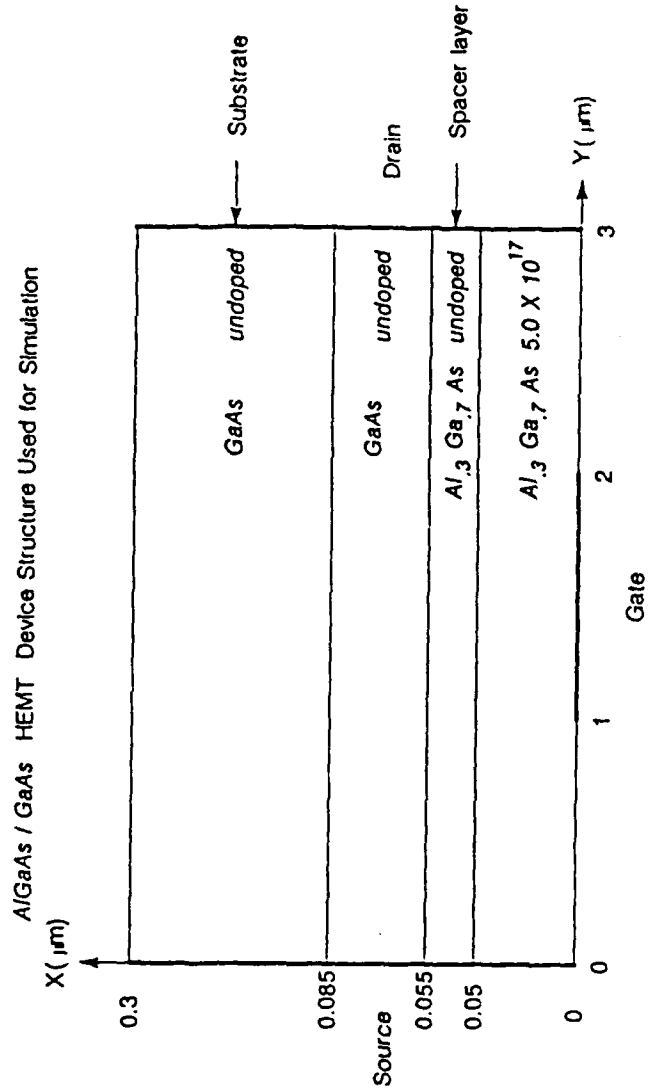
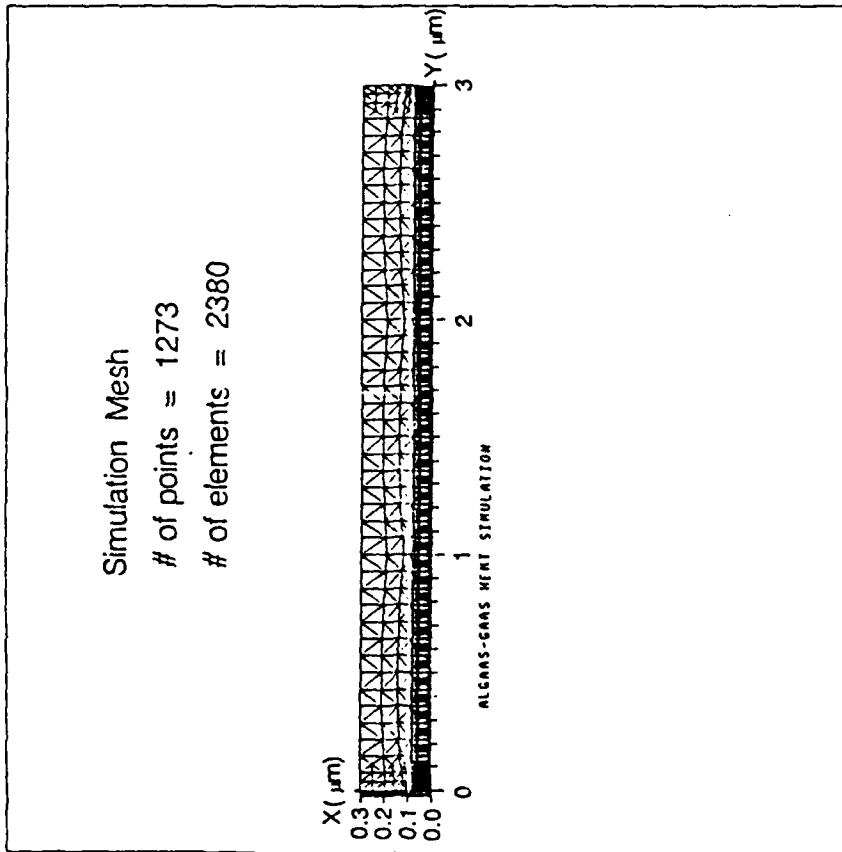


Fig. 1

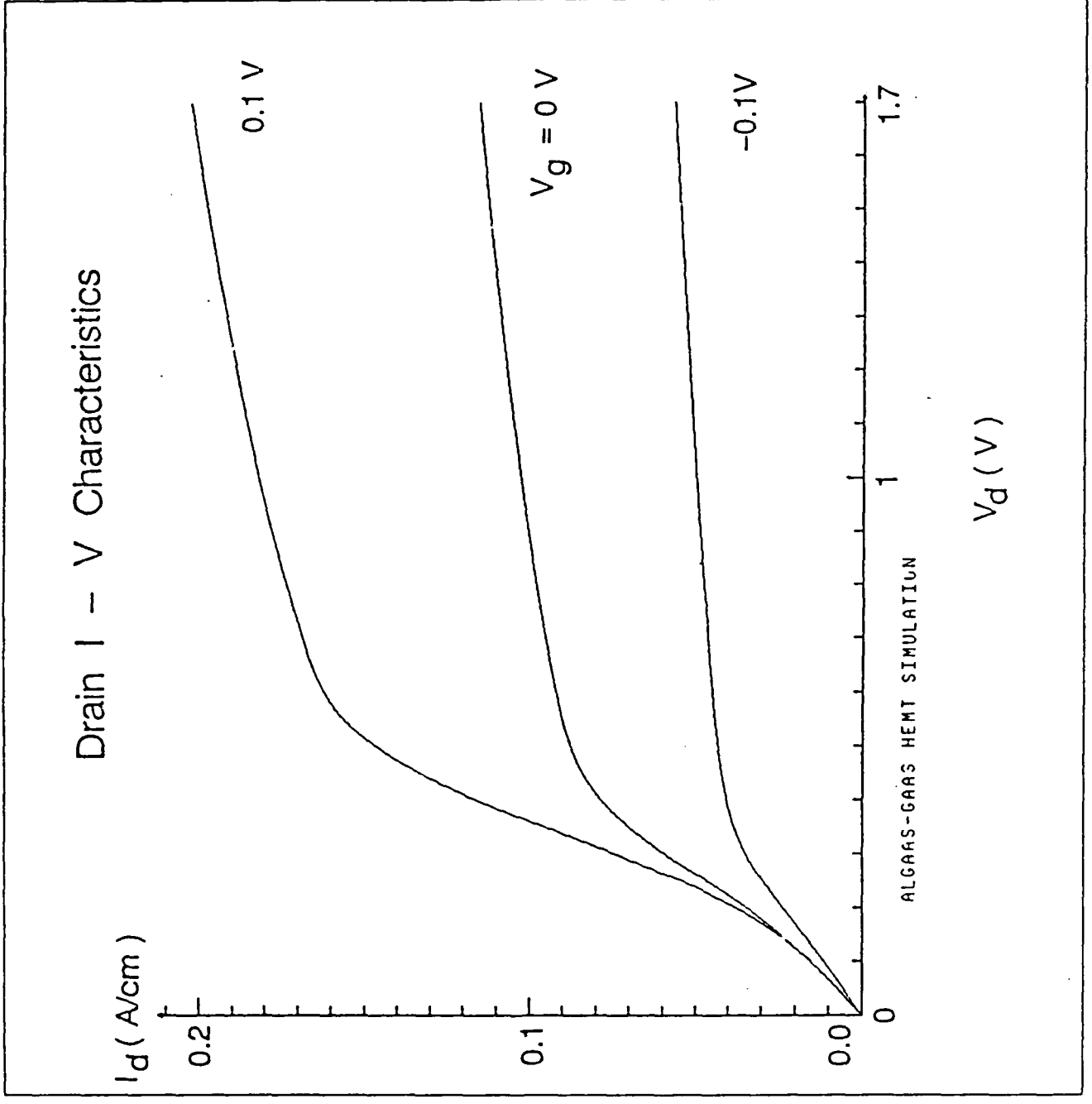
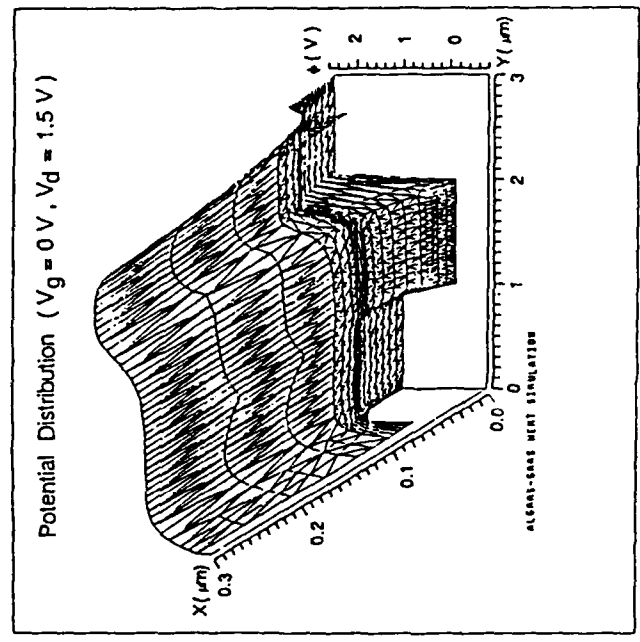
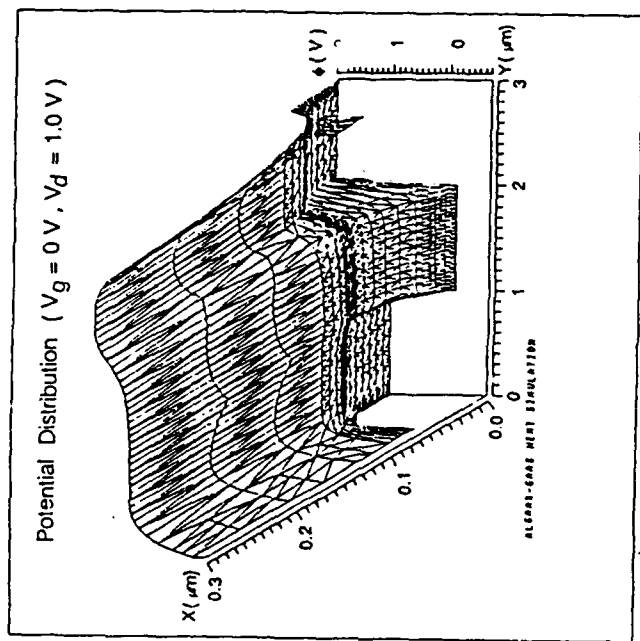
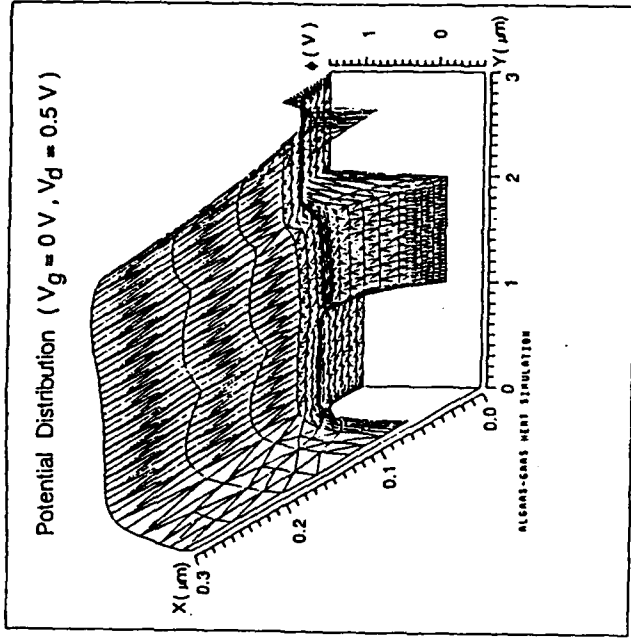
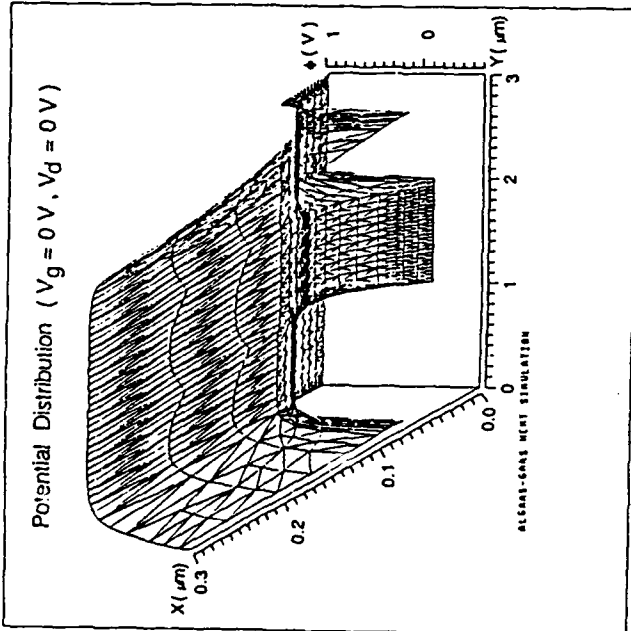


Fig. 2



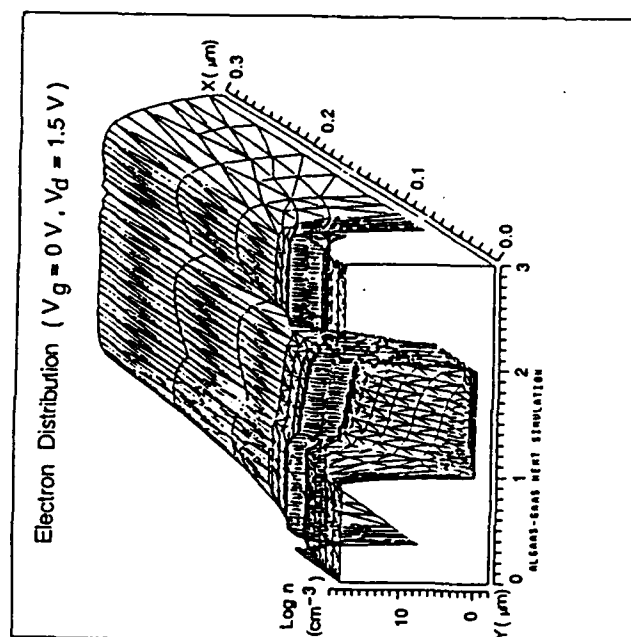
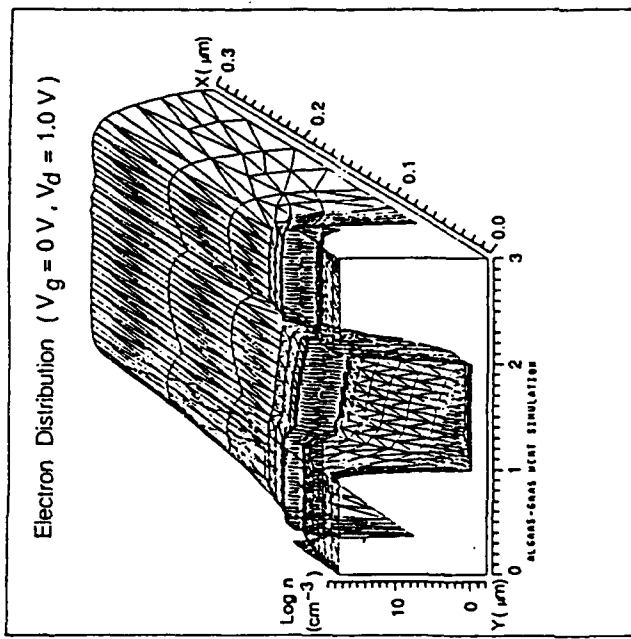
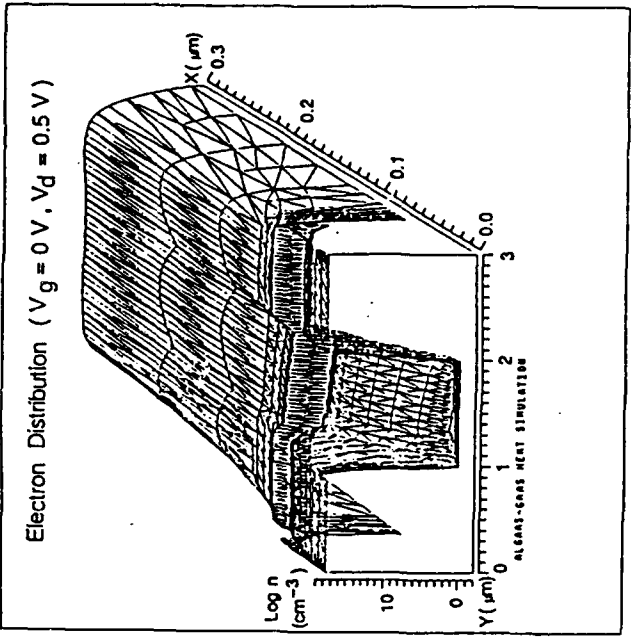
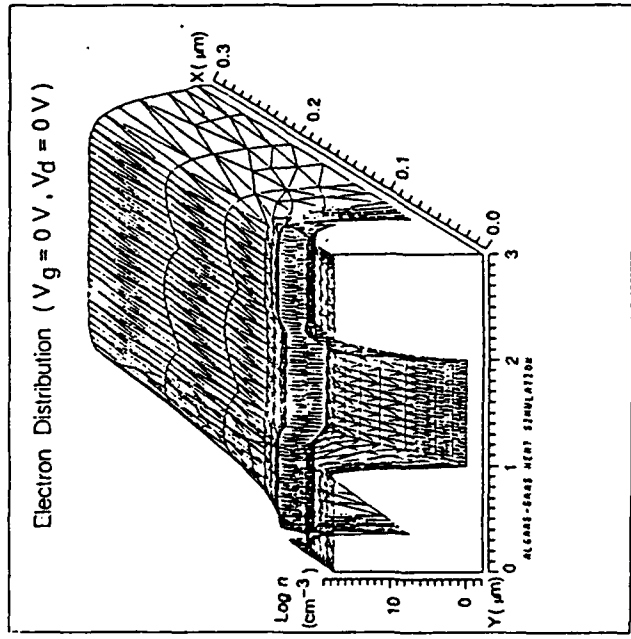


Fig. 4

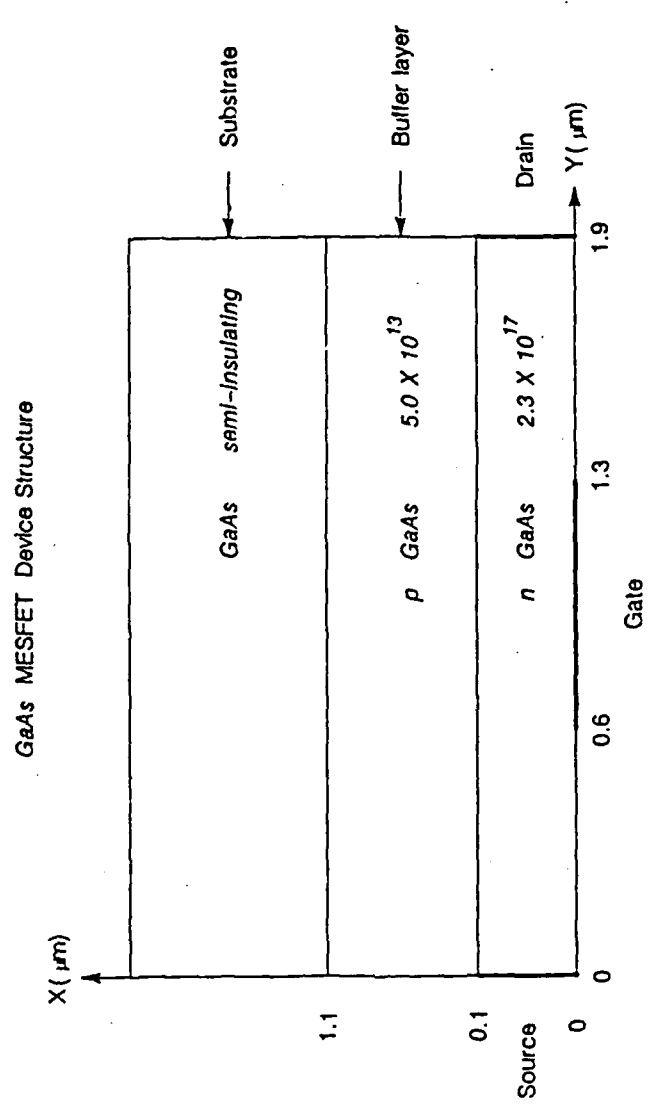
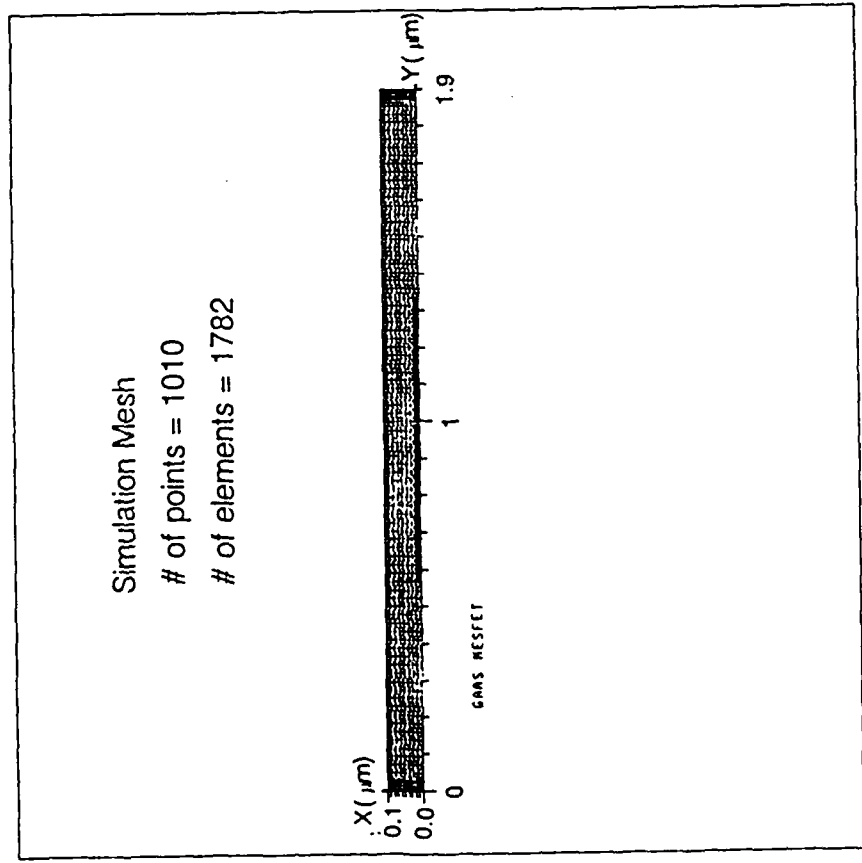


Fig. 5

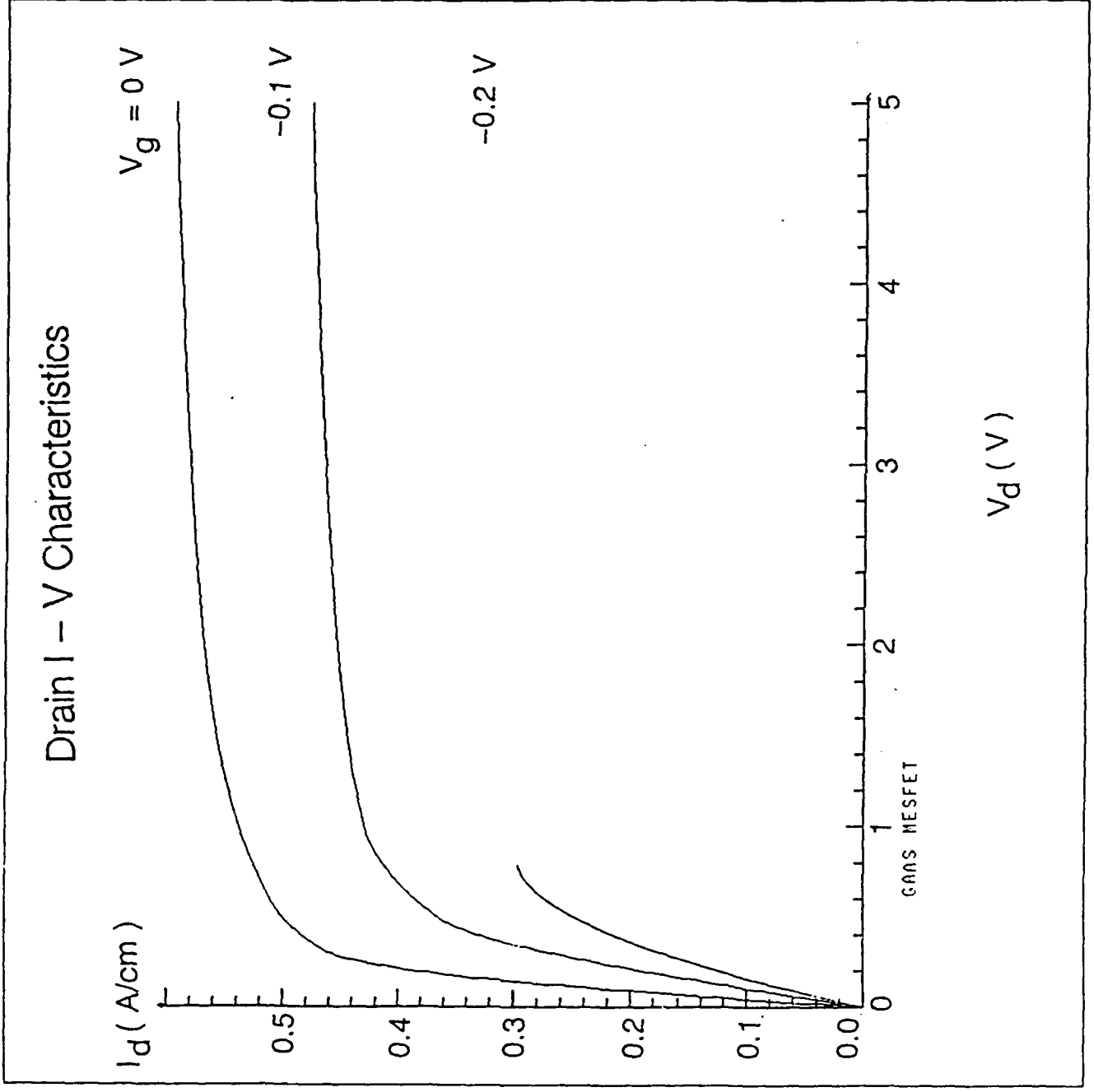


Fig. 6

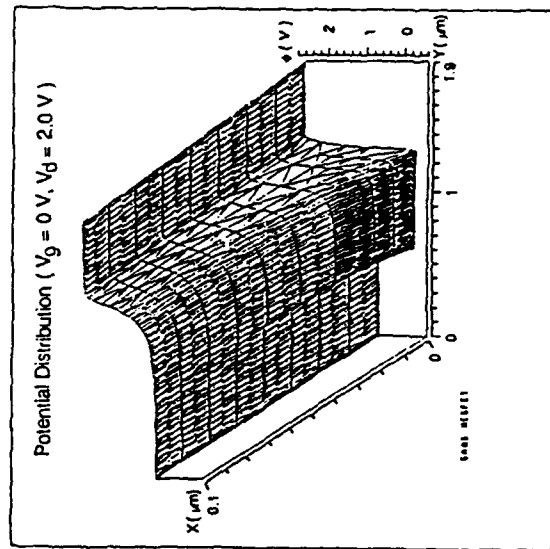
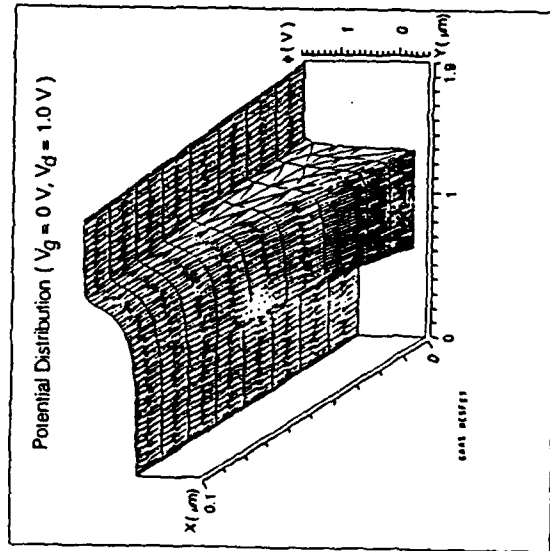
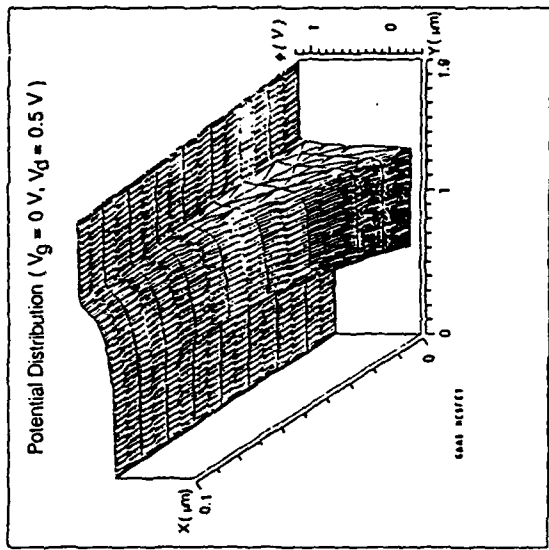
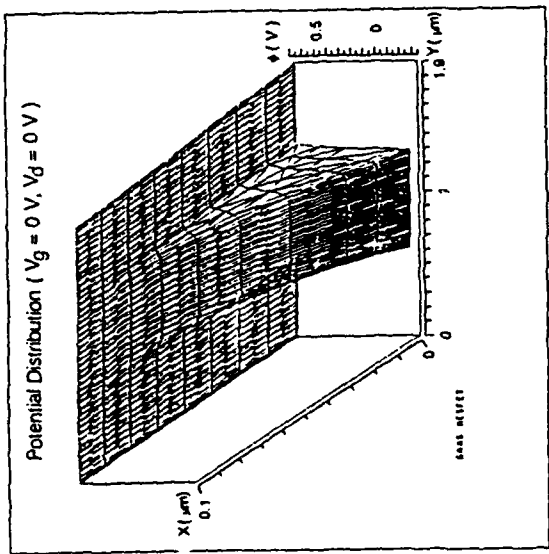
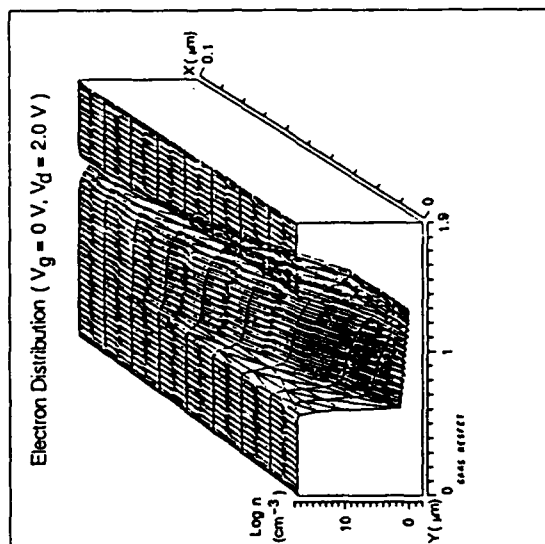
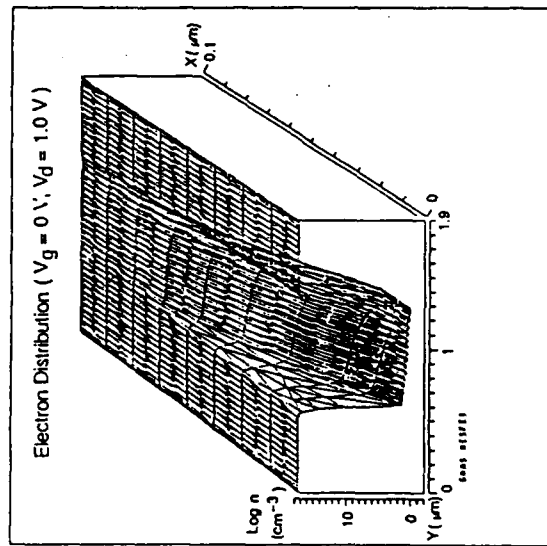
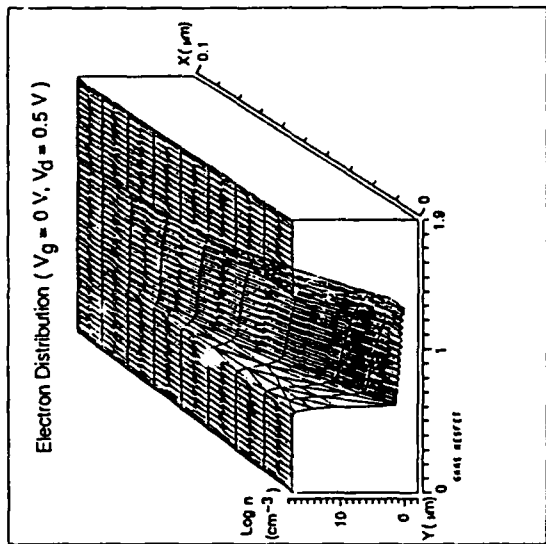
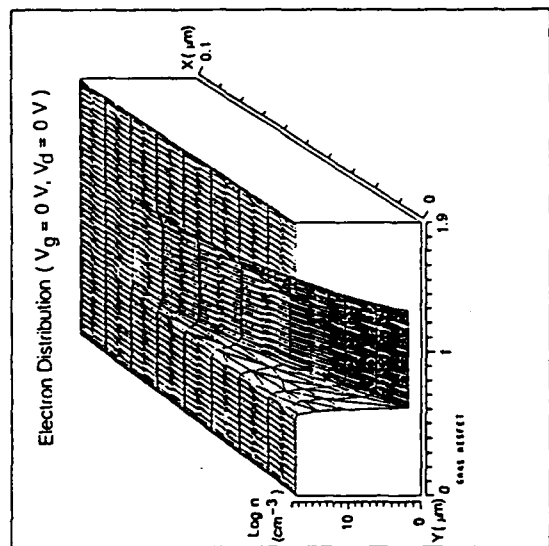
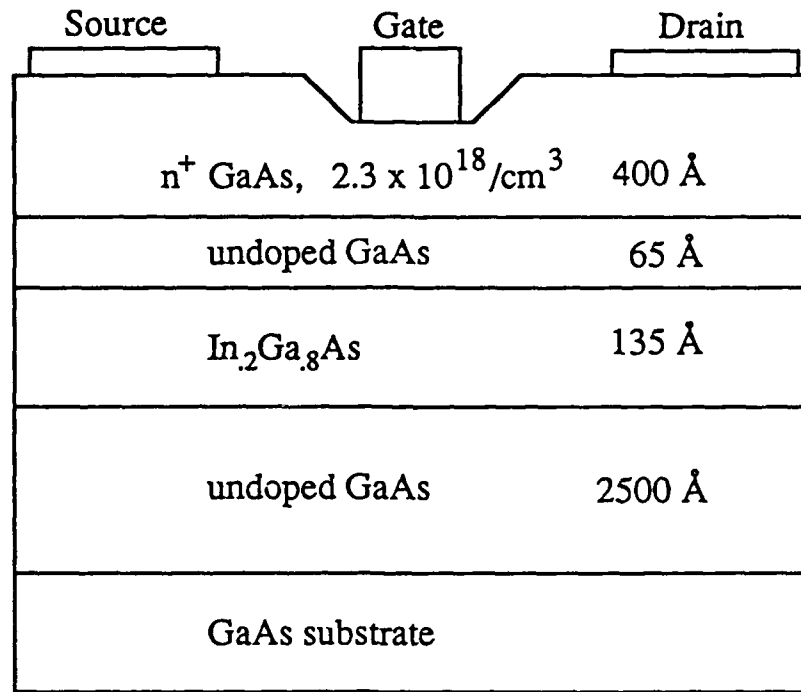
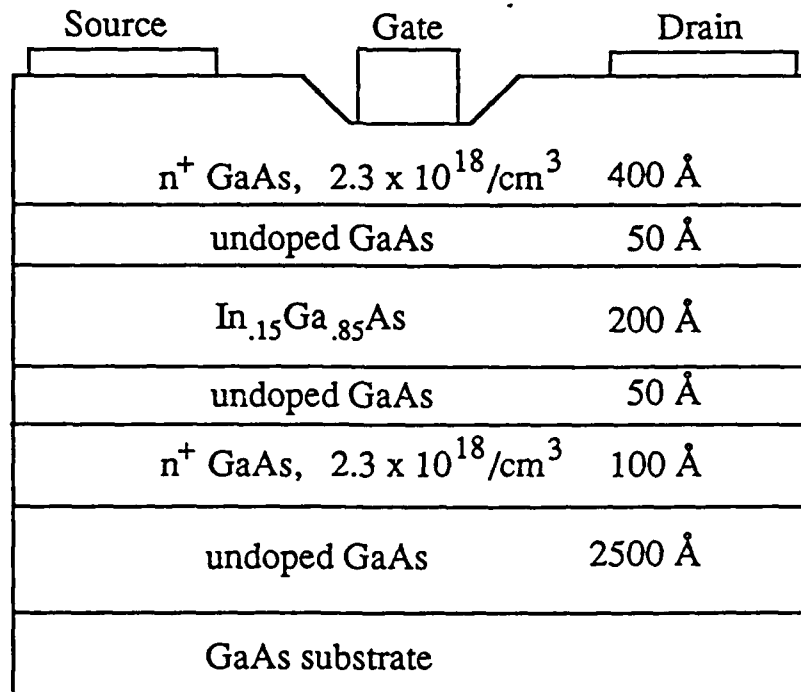


Fig. 7



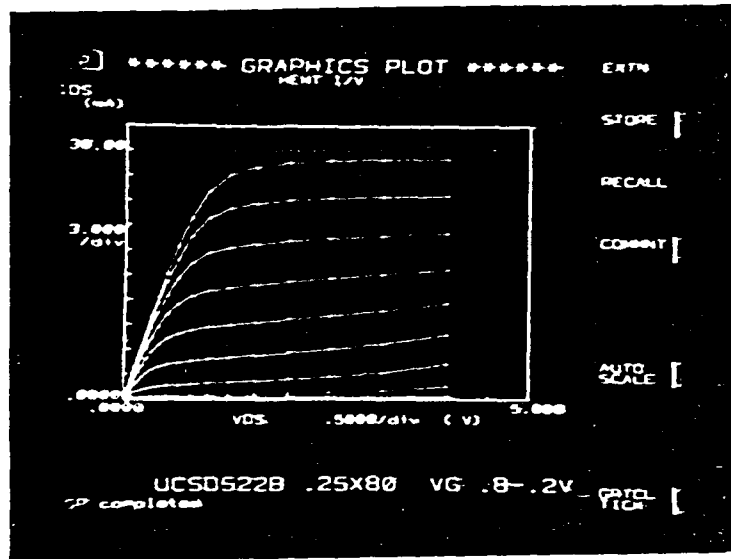


a) Layer structure of single heterojunction In_{0.2}Ga_{0.8}As/GaAs HEMT

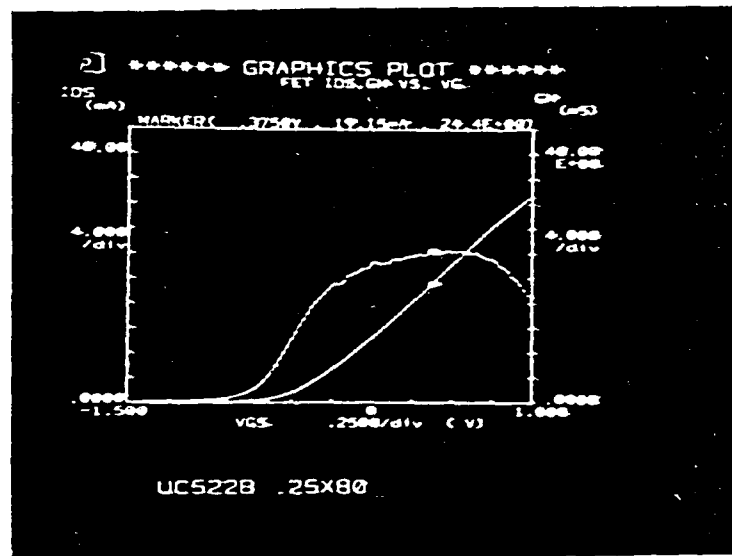


b) Layer structure of double heterojunction In_{0.15}Ga_{0.85}As/GaAs HEMT

Fig. 9



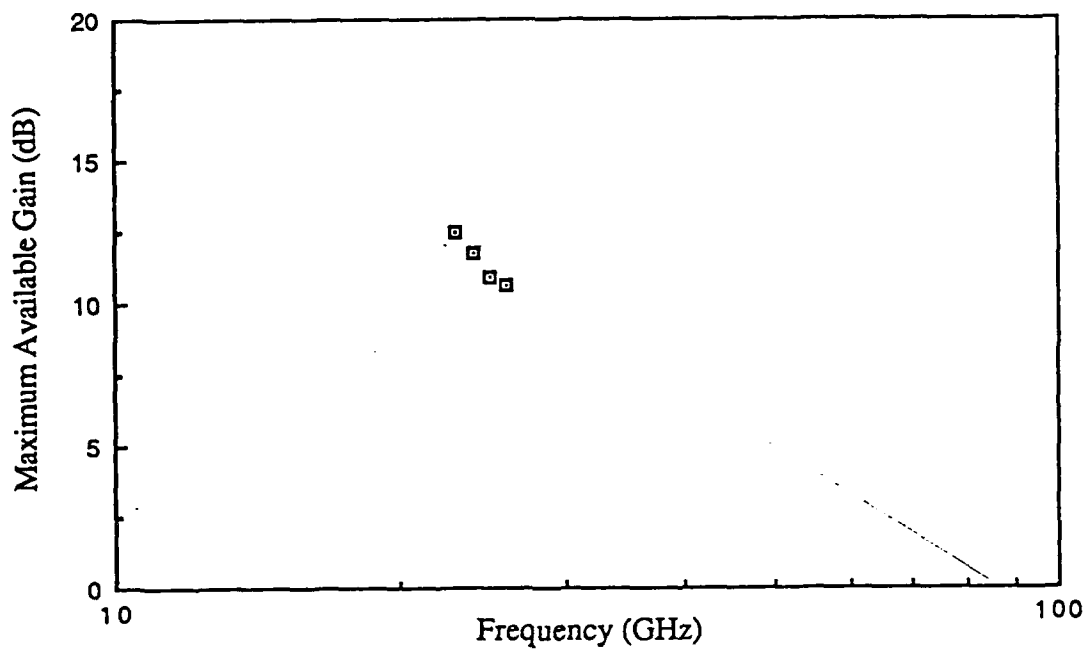
I-V characteristics of the HEMT



Transconductance and drain current versus gate bias

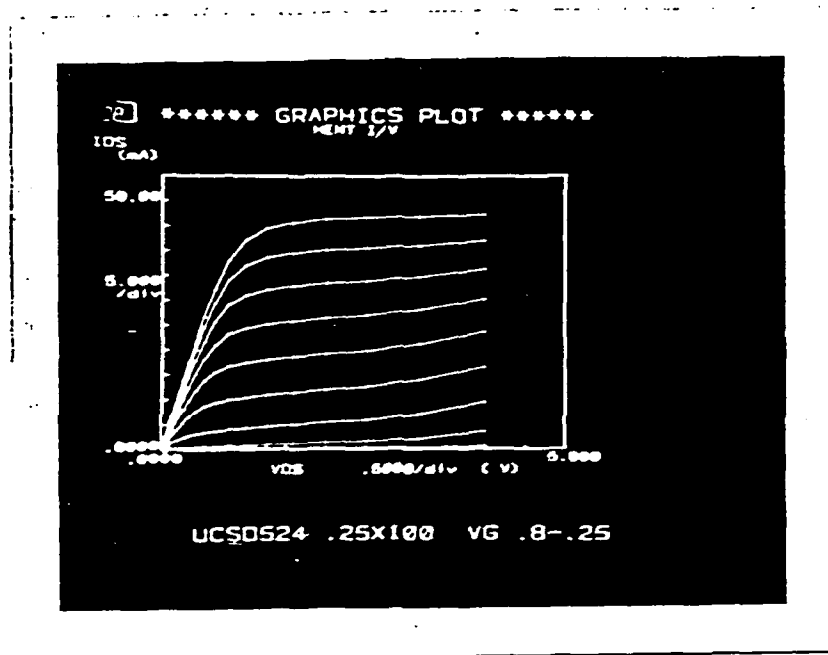
DC characteristics of single heterojunction $\text{In}_{.2}\text{Ga}_{.8}\text{As}/\text{GaAs}$ HEMT

Fig. 10

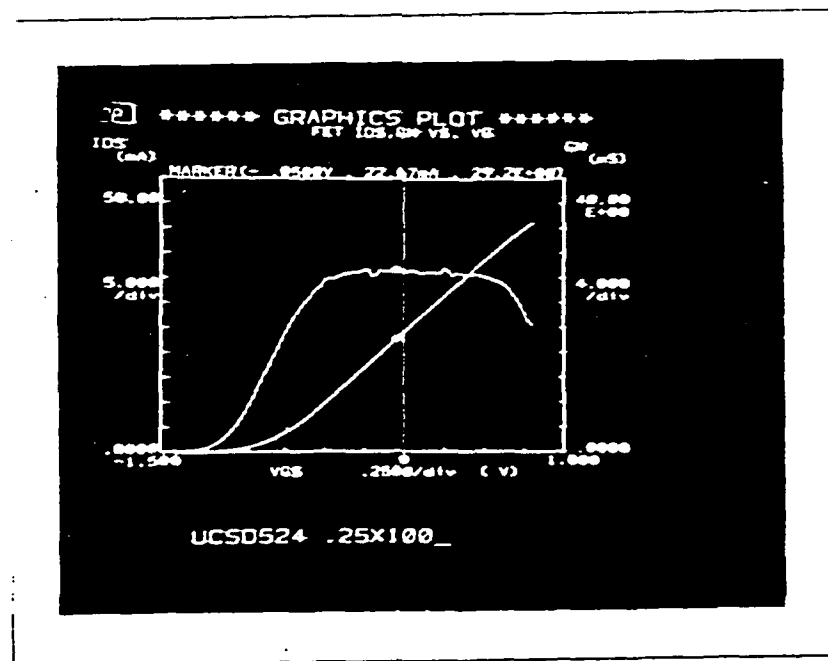


Maximum available gain versus frequency for a 0.25 μ m gate single heterojunction InGaAs/GaAs HEMT

Fig. 11



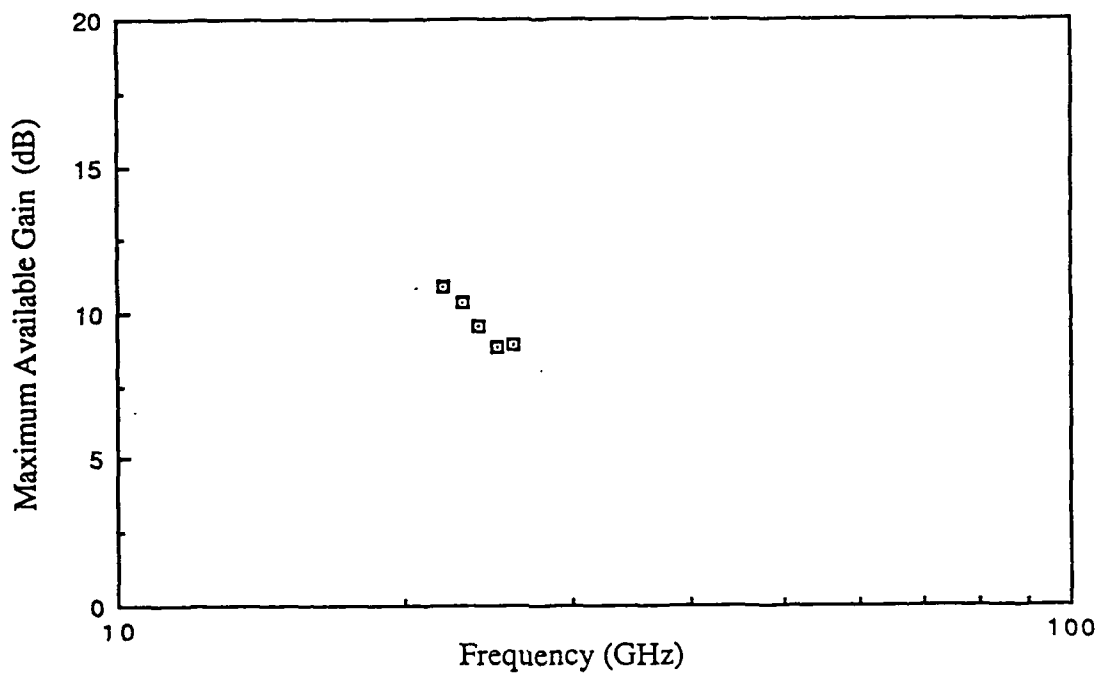
I-V characteristics of the HEMT



Transconductance and drain current versus gate bias

DC characteristics of double heterojunction $\text{In}_{.15}\text{Ga}_{.85}\text{As}/\text{GaAs}$ HEMT

Fig. 12



Maximum available gain versus frequency for 0.25 μ m gate double heterojunction In Ga As/GaAs HEMT

Fig. 13

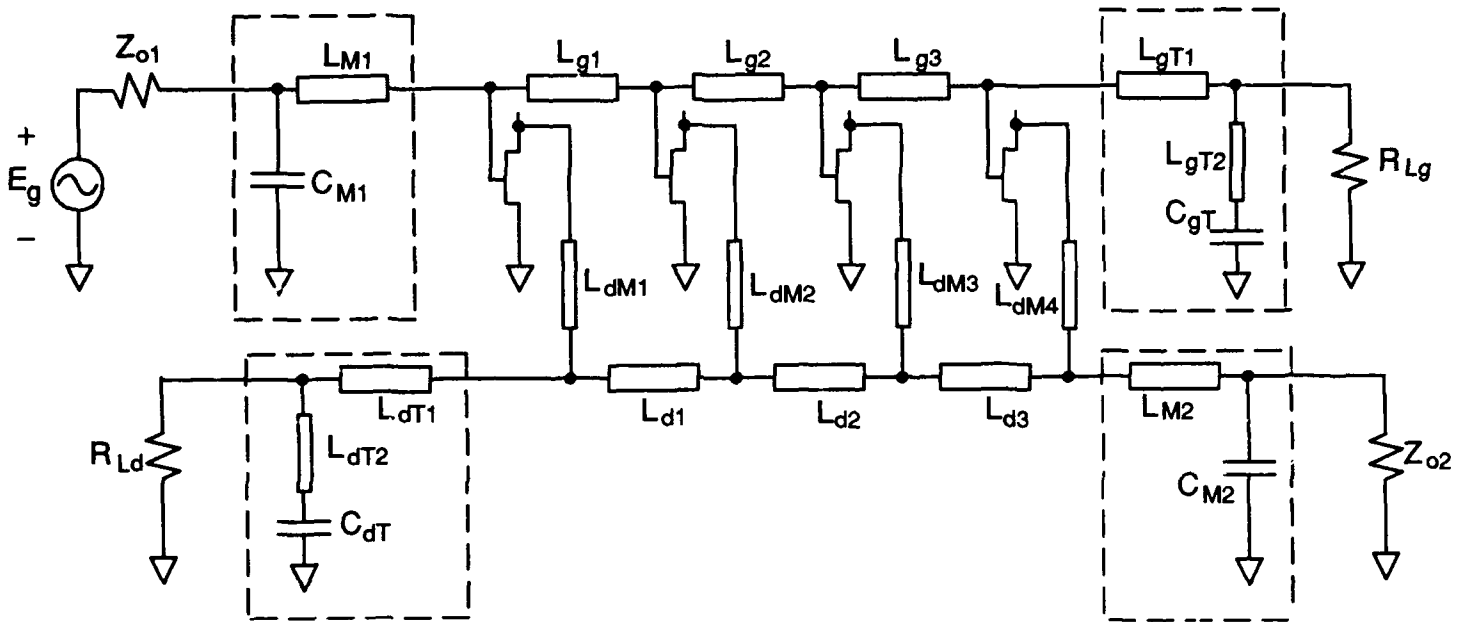


Fig. 14

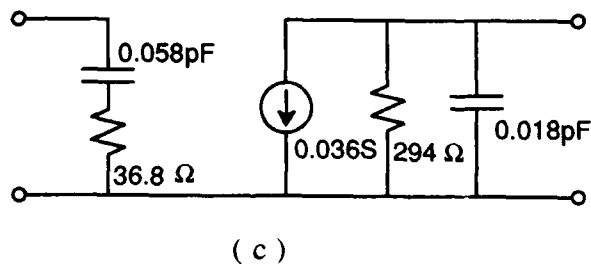
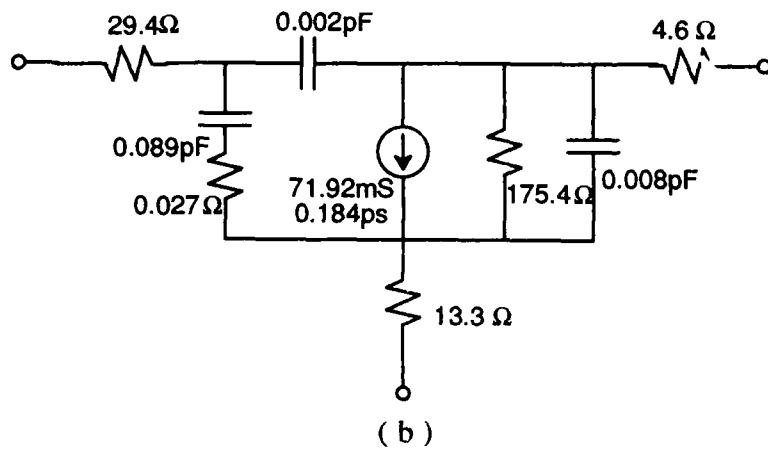
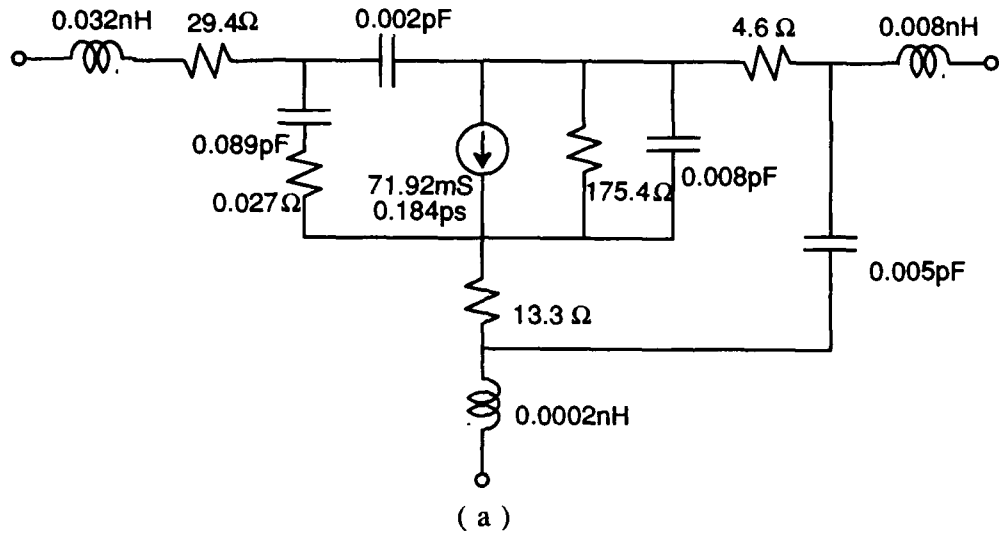
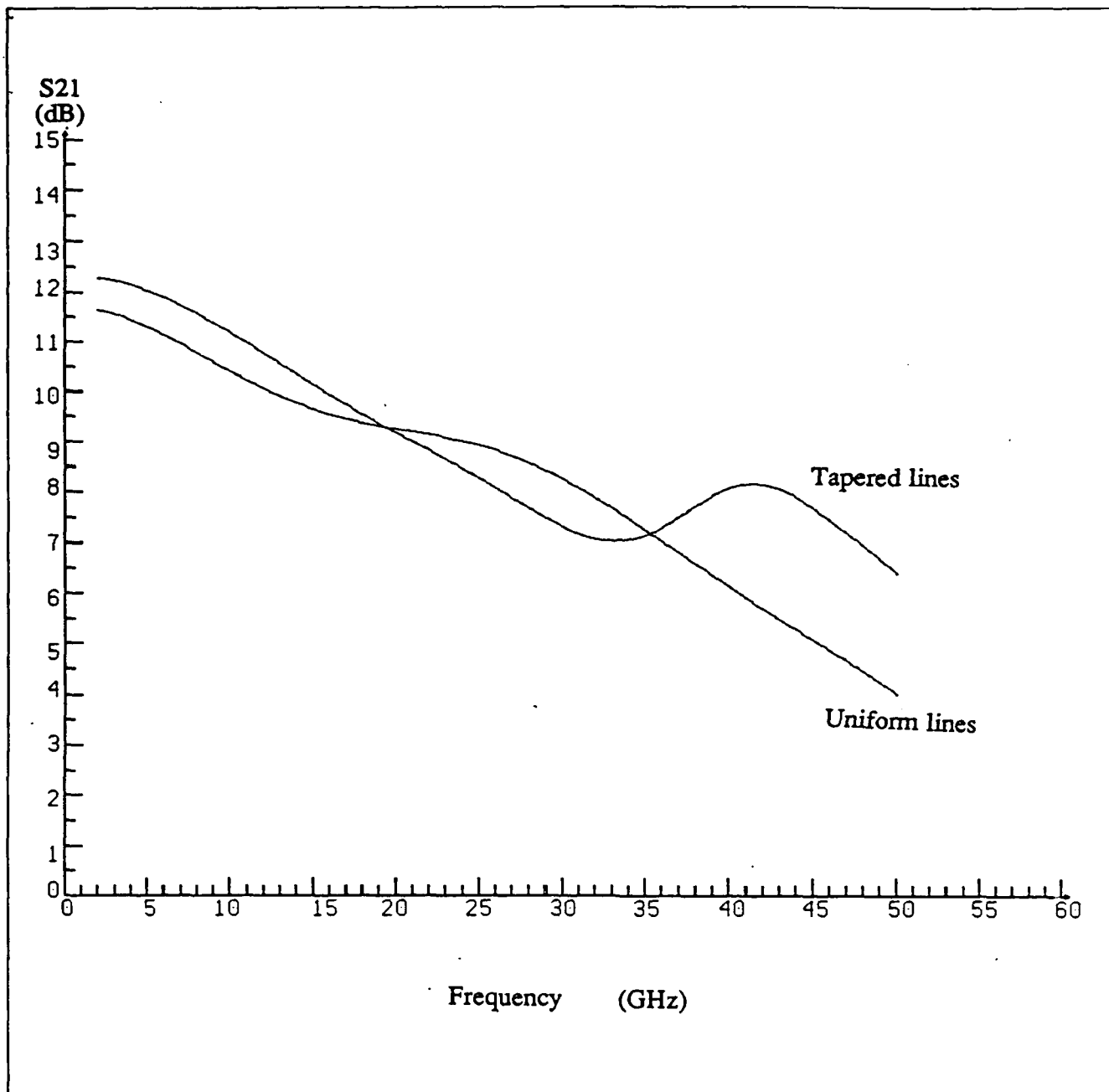
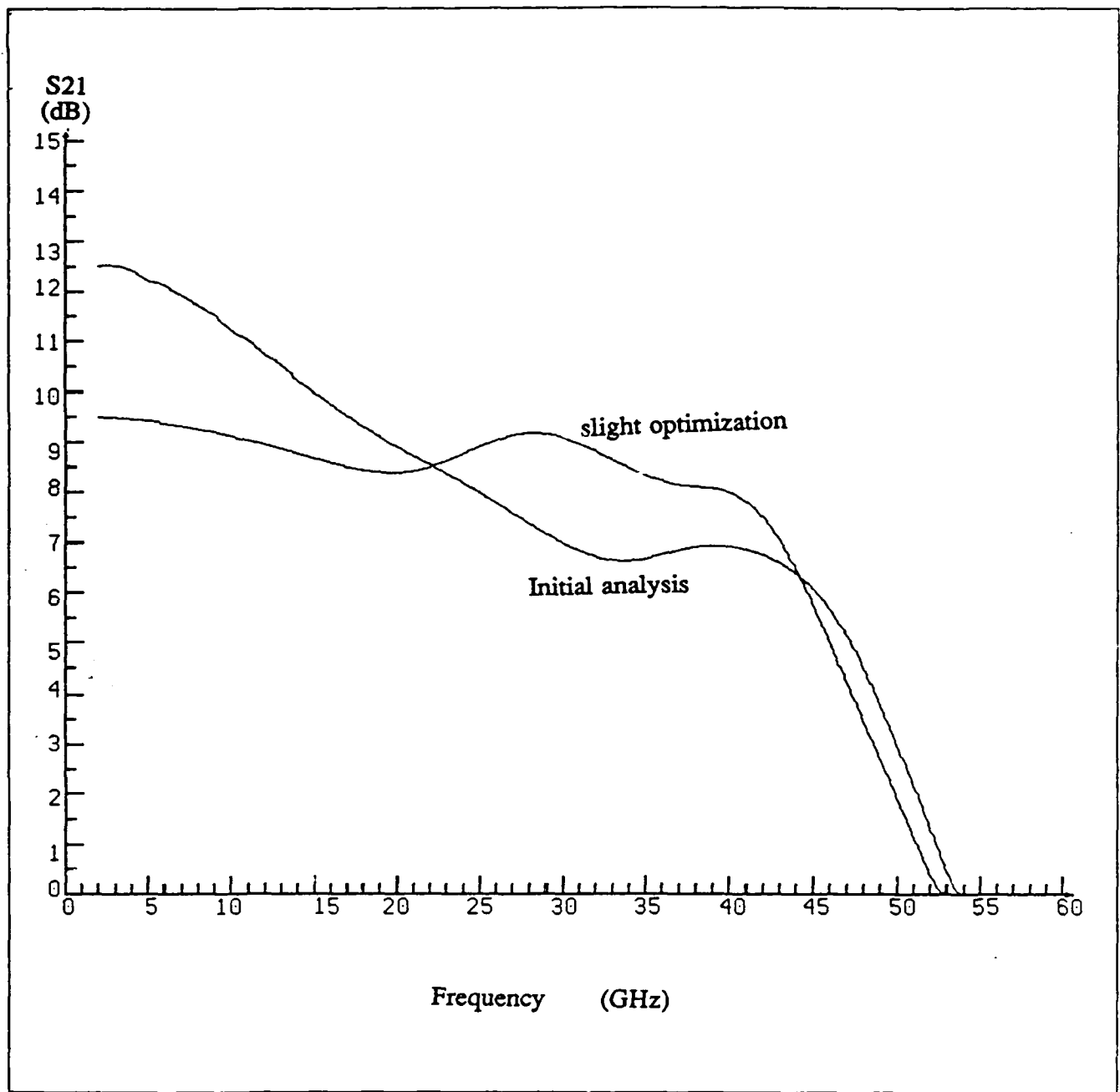


Fig. 15



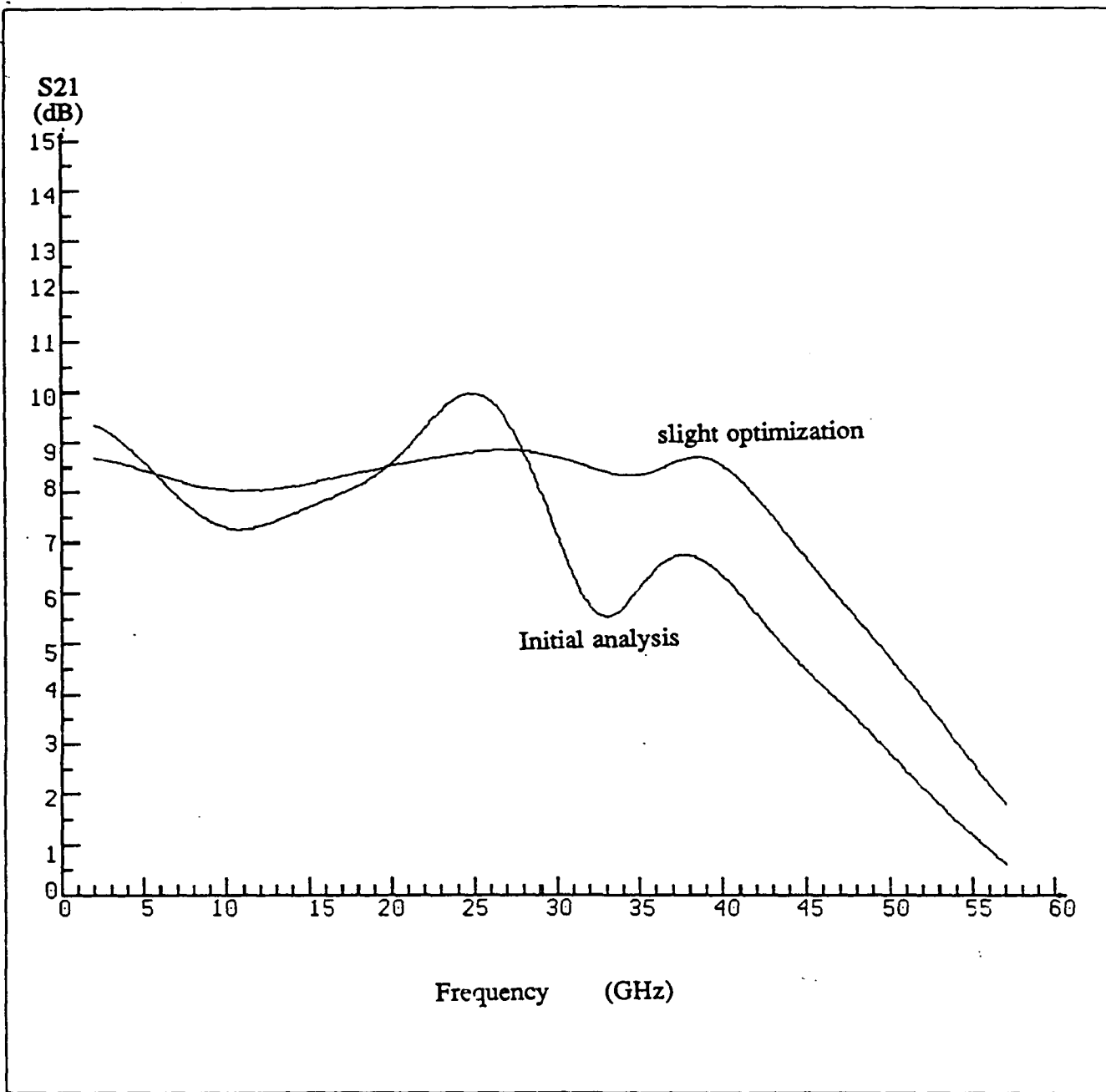
The results designed by DFETA program for the distributed amplifiers with ideal uniform gate and drain transmission lines, and with tapered gate and drain transmission lides.

Fig. 16



The initial analysis and slight optimization results by Touchstone for the distributed amplifier with tapered lines and with the de-embedded model in place of the simplified model.

Fig. 17



The initial analysis and slight optimization results of distributed amplifier with realizable microstrips. The element values are listed in Table 3.

Fig. 18

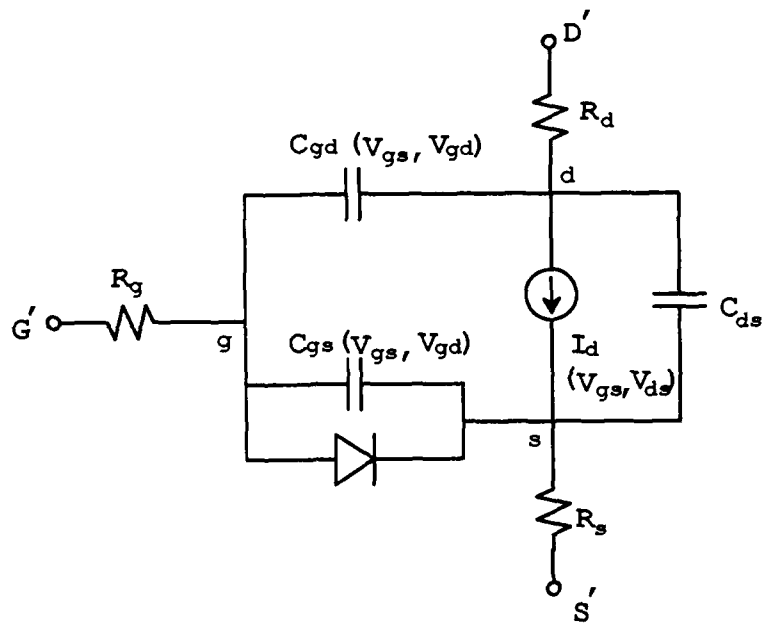
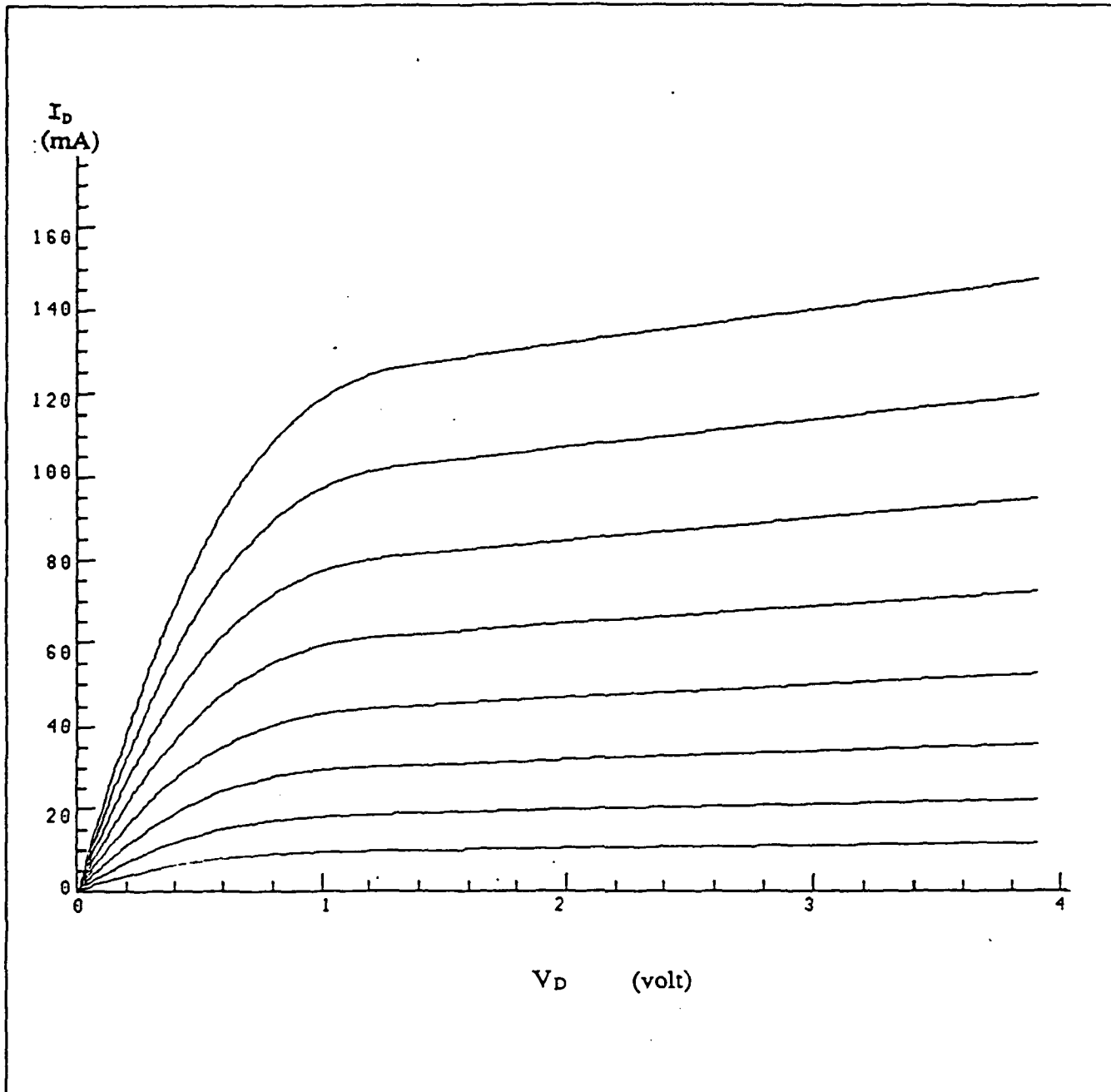


Fig. 19(a)



(b) DC characteristics of the nonlinear MESFET model.
 $V_{to} = -1.308$ $\text{Beta} = 0.035$ $\text{Alpha} = 2.382$
 $\text{Lambda} = 0.0809$ $b = 0.0$

Fig. 19

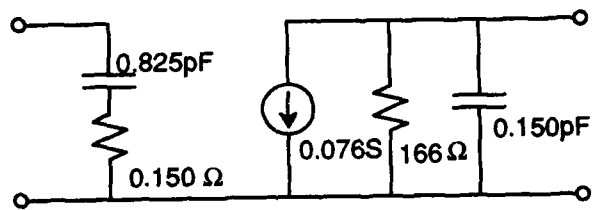
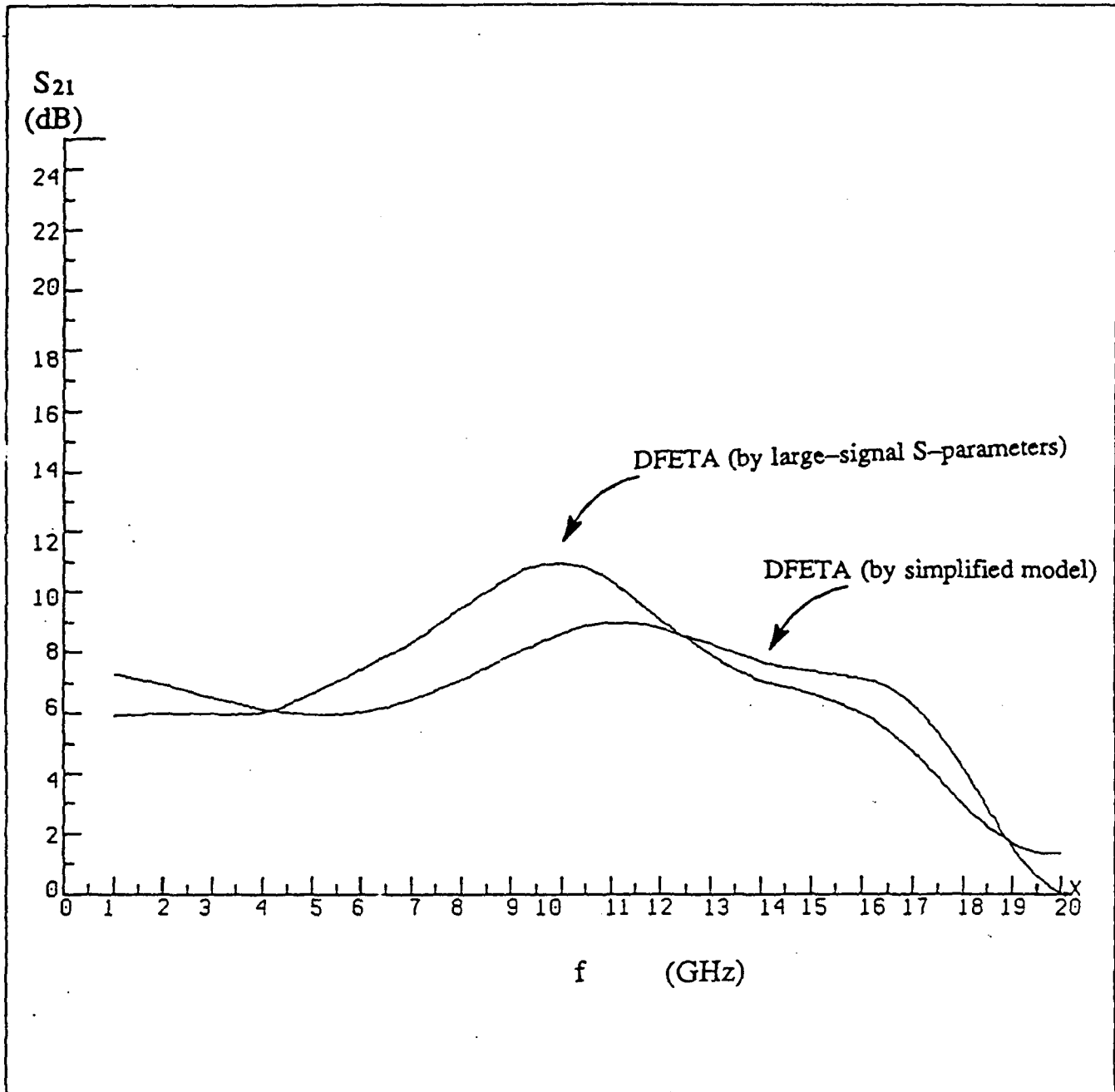


Fig. 20



The result predicted by DFETA with large-signal simplified model and the result analyzed by Touchstone with large-signal S-parameters in place of simplified model in distributed amplifier design.

Fig. 21

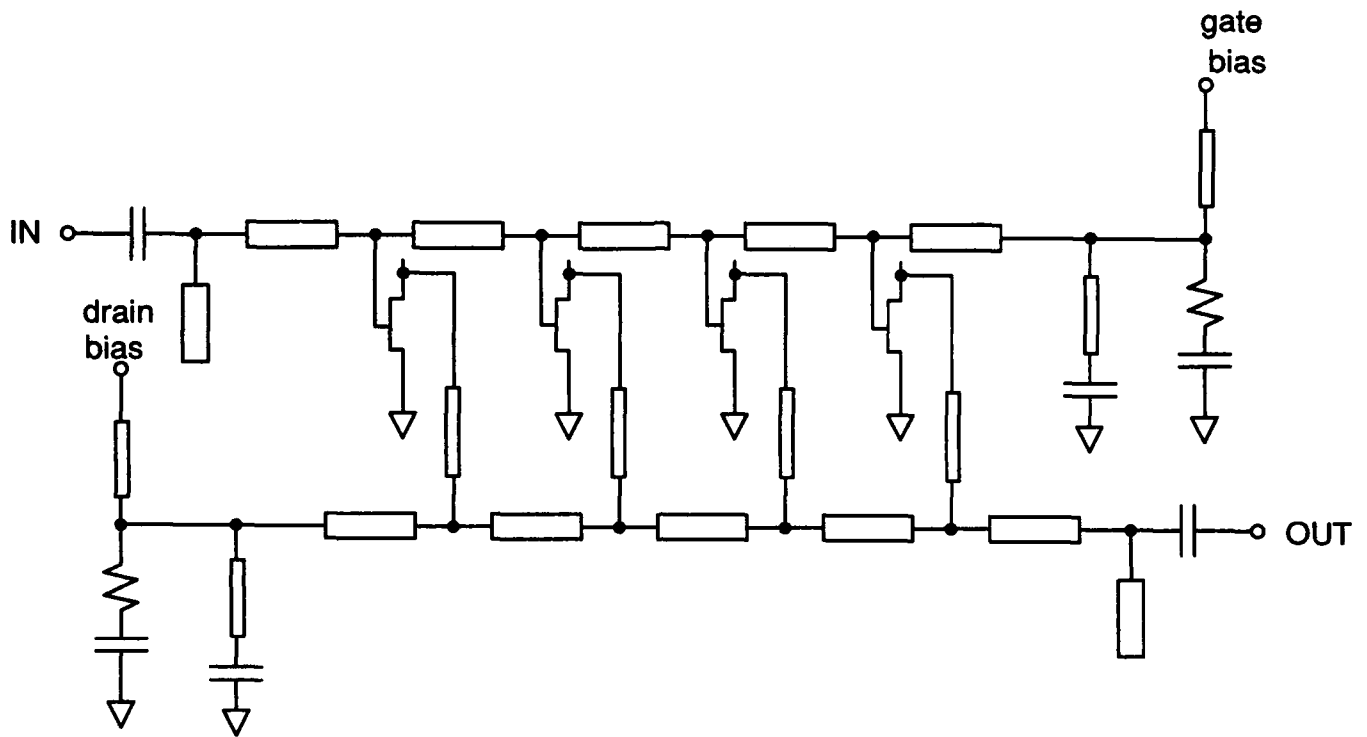
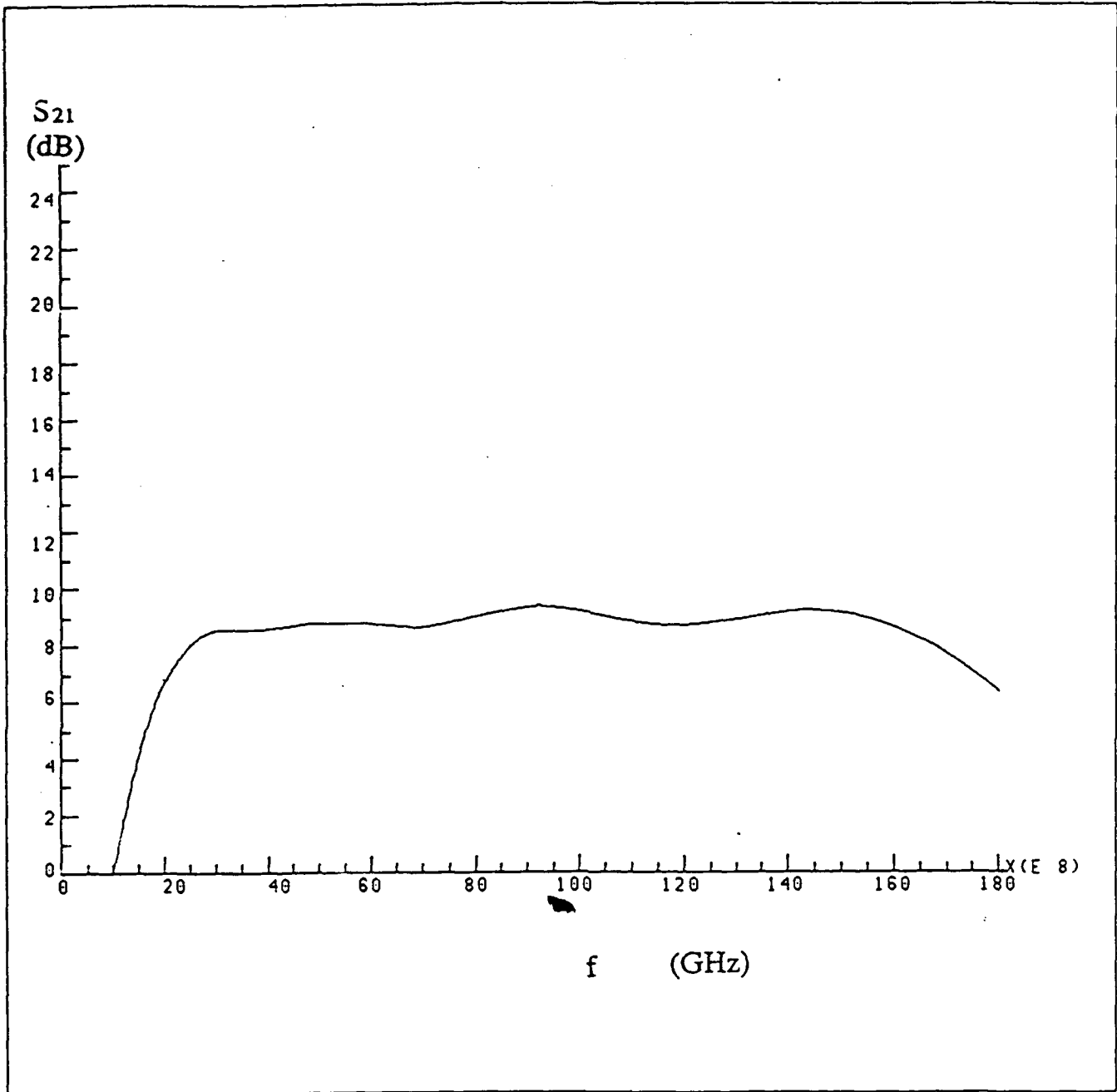
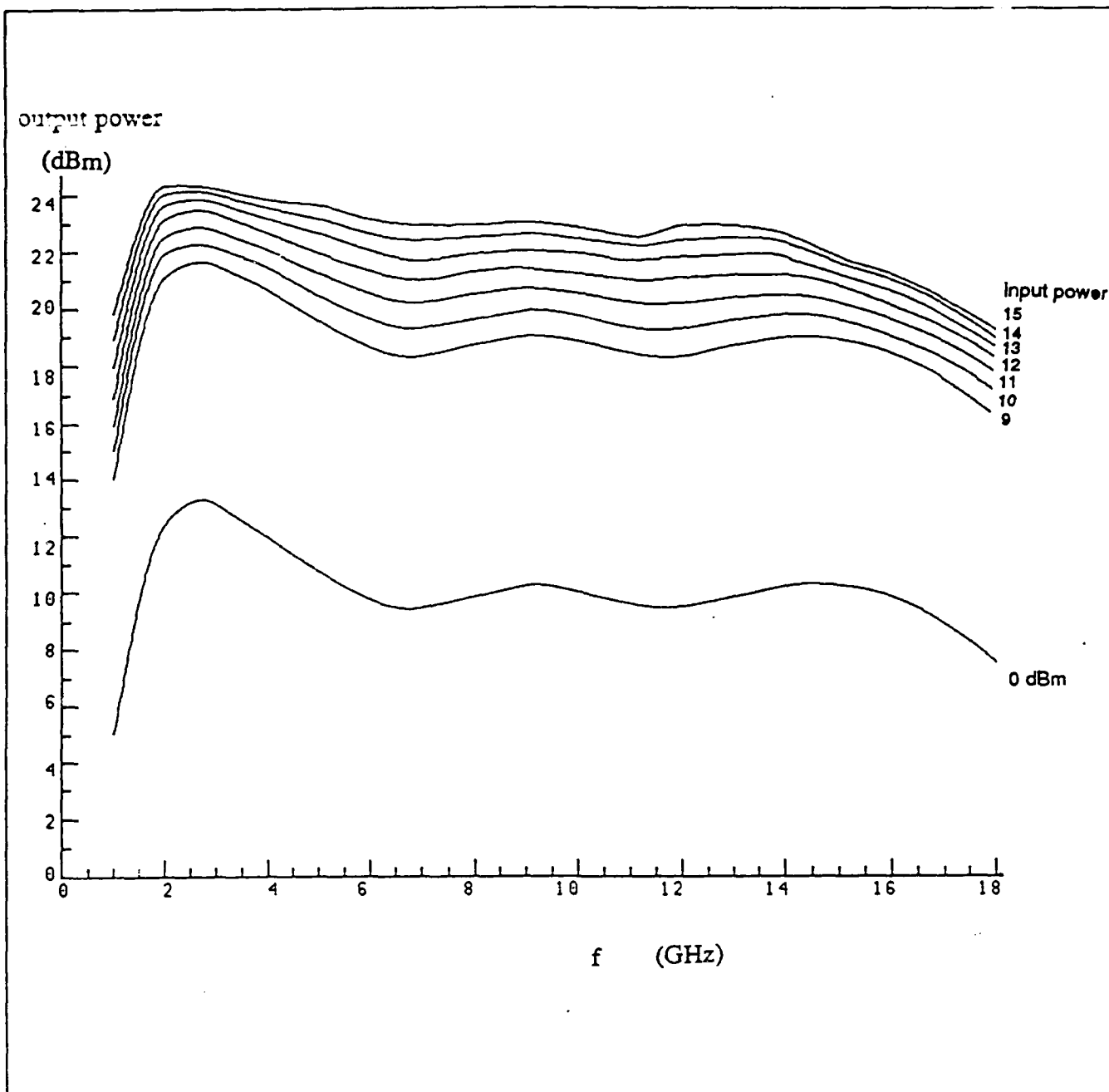


Fig. 22



The result of distributed amplifier with large-signal S-parameters after slight optimization.

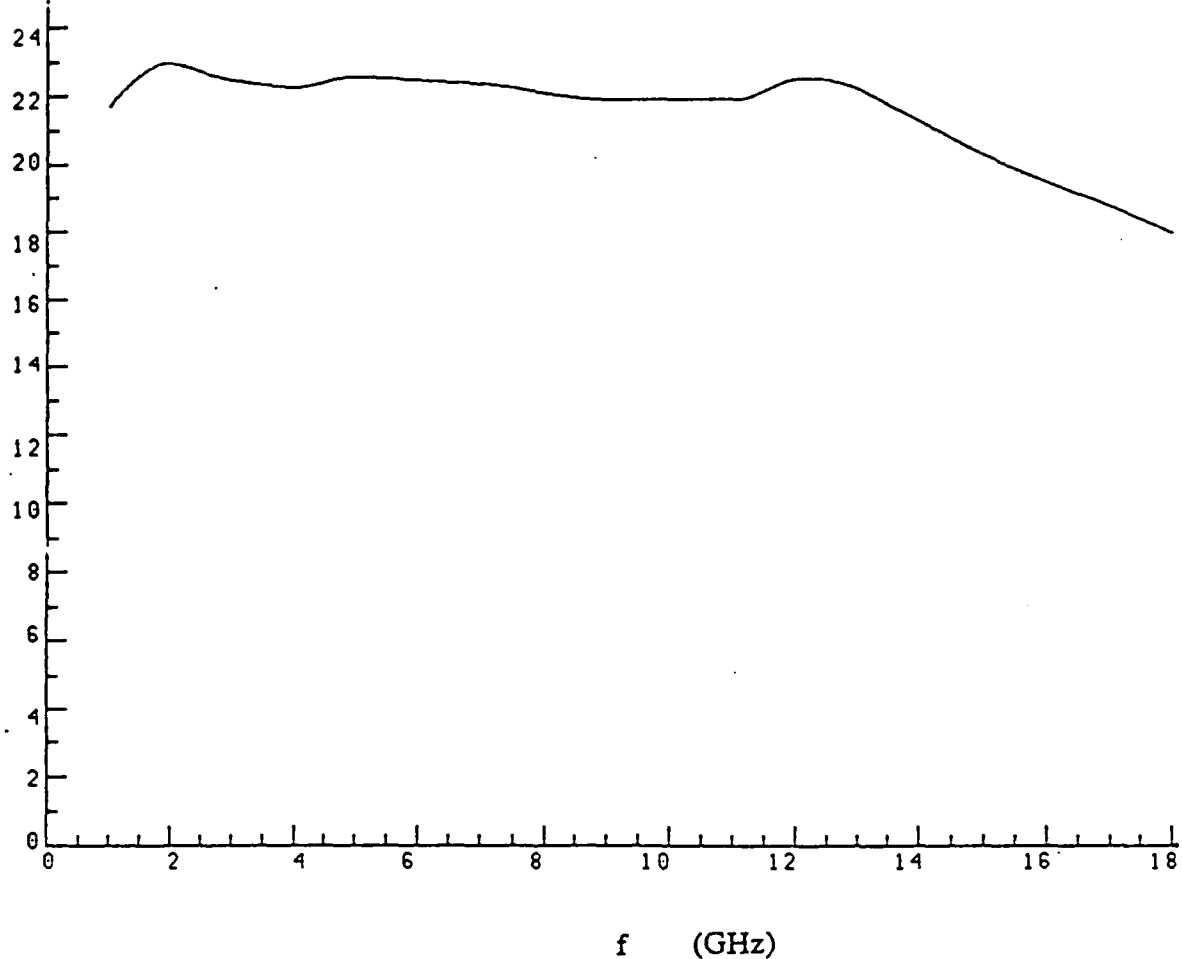
Fig. 23



Output power level corresponding to each RF input power level

Fig. 24

output power
(dBm)



1 dB compression of power distributed amplifier.

Fig. 25

Table I

Z_g (Ω)	L_g (nH)	microstrip length (μm)
56.6	0.13	141.3
67.9	0.149	204.4
79.3	0.203	278.4
90.6	0.265	363.5
101.9	0.335	459.5
113.2	0.414	567.8

Table II

Z_d (Ω)	L_d (nH)	microstrip length (μm)
80	0.115	157.7
90	0.146	200.2
100	0.180	246.9
110	0.218	300.0
120	0.259	355.2
130	0.304	417.0
140	0.353	484.2
150	0.405	555.5
160	0.461	632.3
170	0.520	713.2
180	0.583	800.0
190	0.650	891.5
200	0.720	987.5
210	0.794	1089.0

Table III

	L_{M1}	L_{g1}	L_{g2}	L_{g3}	L_{gT1}	L_{gT2}	L_{dM1}	L_{dM2}
microstrip width (μm)	18	18	18	18	18	10	10	10
microstrip length (μm)	131	225	280	263	386	232	186	240

	L_{M2}	L_{d1}	L_{d2}	L_{d3}	L_{dT1}	L_{dT2}	L_{dM3}	L_{dM4}
microstrip width (μm)	18	18	18	18	18	10	10	10
microstrip length (μm)	140	401	394	250	415	218	199	232

Z_{o1}	Z_{o2}	R_{Lg}	R_{Ld}	C_{M1}	C_{M2}	C_{gT}	C_{dT}
$50\ \Omega$	$50\ \Omega$	$47\ \Omega$	$53.8\ \Omega$	0 pF	0 pF	0.052pF	0.053pF

Appendix A

On the Charge Control of the Two-Dimensional Electron Gas for Analytical Modeling of HEMT's

On the Charge Control of the Two-Dimensional Electron Gas for Analytic Modeling of HEMT's

AN-JUI SHEY AND WALTER H. KU

Abstract—A simple charge control model of the two-dimensional electron gas (2-DEG) of HEMT's, which explicitly takes into account the effective distance of the 2-DEG from the heterointerface, has been developed for use in analytic I - V and C - V modeling. In this model, the Fermi energy level versus the 2-DEG sheet carrier concentration is represented by a simplified expression derived from the triangular potential well approximation and is shown to be dominated by terms with different functional forms in two distinct operation regions: a moderate carrier concentration region and a subthreshold region. The validity of the analytic charge control model is supported by the calculated results of self-consistent quantum mechanical model.

I. INTRODUCTION

THE recent development of the HEMT, employing novel layer structures such as strained-layer heterostructures, has shown a promise of higher transconductance and a good power capability resulting from superior electronic transport properties of the active channel, a larger sheet carrier concentration, and better confinement at the heterointerface. These enhanced characteristics lead to improved device performance which demands a more accurate approximation of the charge control model over a wider operation range in order to obtain accurate HEMT I - V and C - V models useful for circuit simulators. The analytic models most widely used for characterizing HEMT performance are based on the linear charge control model [1], [2], which either neglects the variation of the Fermi potential with the gate bias, or for simplicity, assumes a constant correction distance in the direction normal to the heterointerface plane accounting for the quantization of the two-dimensional electron gas (2-DEG) in the quasi-triangular potential well. These assumptions only hold for a very narrow range and result in a low degree of accuracy in the model when device behavior is characterized over the whole operation region.

Recently, Kola *et al.* [3] proposed a data fitting expression for Fermi level versus sheet carrier concentration that would take into consideration the modulation effect of an applied bias on the Fermi energy. However, the expression lacks corresponding physical significance and requires a sophisticated data fitting process. In this study, we developed a simple yet more accurate Fermi energy expression, derived from the triangular

potential well approximation, which yielded a more rigorous analytic charge control model in which the dependence of the effective distance of the 2-DEG from the heterojunction on the 2-DEG carrier concentration was accurately reflected.

II. EXTENDED MODEL

To obtain an exact charge control formulation of the 2-DEG channel in HEMT structures, Poisson's equation and Schrödinger's equation would need to be self-consistently solved. Unfortunately, the physical calculations are too involved for use in analytic device modeling. However, an approximation approach based on the linear charge control concept can be applied [4]. Additionally, the triangular well approximation, in conjunction with Fermi statistics, was found to give a fair description of the 2-DEG carrier concentration dependence on the gate voltage if an appropriate empirical parameter was incorporated to account for the discrepancy in field strength due to the assumption of an infinite barrier height imposed on the junction [5].

Consider a HEMT structure with an n -type substrate, whose energy band diagrams are shown in Fig. 1. The flat-band voltage is the gate voltage applied simply to counterbalance the bending of the quasi-Fermi level across the active channel at thermal equilibrium and can be expressed as

$$V_{FB} = \phi_B - \left(V_b^0 + \frac{\Delta E_c}{q} + V_n \right) \quad (1)$$

where ϕ_B is the Schottky barrier height; ΔE_c is the conduction band discontinuity; V_n is the potential difference between the Fermi level and the conduction band edge in the neutral substrate and $V_b^0 = qN_{D1}(d_1 - d_e)^2/2\epsilon_1$ is the potential across the fully depleted top layer under flat-band condition, where ϵ_1 , d_1 , and N_{D1} are the permittivity, thickness, and doping density of the large-gap semiconductor layer, respectively; and d_e is the spacer layer thickness.

When the gate bias V_G is higher than V_{FB} , the voltage $V_G - V_{FB}$ can be partitioned between two components: $V_1 = (V_b^0 - V_b)$, the voltage drop absorbed by the top depleted layer, and V_2 , the band bending of the 2-DEG channel, i.e.,

$$V_G - V_{FB} = V_1 + V_2. \quad (2)$$

Referring to the energy band diagram, the band bending across the 2-DEG channel may be expressed by

$$V_2 = E_F + V_n + V_c(x) \quad (3)$$

Manuscript received July 7, 1988; revised September 26, 1988. This work was supported by AFOSR, Boiling Air Force Base, DC, under Grant AFOSR-86-0339 monitored by Dr. G. Witt.

The authors are with the Department of Electrical and Computer Engineering, University of California, San Diego, La Jolla, CA 92093.

IEEE Log Number 8824829.

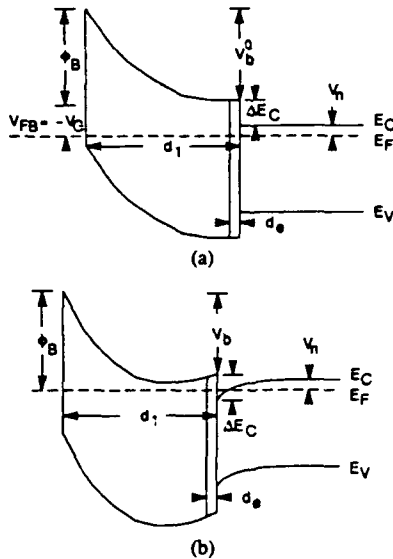


Fig. 1. Energy band diagram of a HEMT on the n^- -type substrate in the 2-DEG charge control regime by a Schottky barrier. (a) Flat-band condition. (b) Thermal equilibrium.

where E_F is the Fermi potential and references the conduction band edge of the 2-DEG channel, and $V_c(x)$ is the channel potential at point x along the channel defined with respect to the source contact.

According to the triangular potential well approximation and Fermi-Dirac distribution the relation between the 2-DEG carrier concentration n_s , and the Fermi-level can be established only if the lower and the first excited subbands are being considered and is given by

$$E_F = \frac{kT}{q} \ln \left\{ -\frac{1}{2} [\exp [(q/kT)\gamma_0 \cdot n_s^{2/3}] + \exp [(q/kT)\gamma_1 \cdot n_s^{2/3}]] + \left(\frac{1}{4} [\exp [(q/kT)\gamma_1 \cdot n_s^{2/3}] - \exp [(q/kT)\gamma_0 \cdot n_s^{2/3}]]^2 + \exp [(qn_s/DkT)] \cdot \exp [(q/kT)(\gamma_0 + \gamma_1) \cdot n_s^{2/3}] \right)^{1/2} \right\} \quad (4)$$

where D is the density of states in the 2-DEG, and γ_0 and γ_1 are material parameters, usually estimated from experimental measurements [1]. For moderate values of n_s , the argument of the exponential terms is small and a series expansion of these terms converges. For qualitative consideration, we end the expansion after the linear term. The result for the Fermi potential takes the simplified form

$$E_F \cong \frac{kT}{q} \ln \left(\frac{qn_s}{2DkT} \right) + \frac{D}{4} (\gamma_1 - \gamma_0)^2 \cdot n_s^{1/3} + (\gamma_0 + \gamma_1) \cdot n_s^{2/3}. \quad (5)$$

The contribution of the second term to the variation of Fermi energy with carrier concentration is apparently small com-

pared to other terms. Furthermore, the first term dominates only in the subthreshold region. In the normal operation region the former two terms can be considered to be a constant which can be evaluated at the equilibrium carrier concentration n_{s0} . Therefore, we can approximate E_F by expression of the form

$$E_F = E_{F0} + \gamma \cdot n_s^{2/3}. \quad (6)$$

By charge conservation and Gauss' law, further manipulations yield the 2-DEG charge control formulation as

$$Q_n = qn_s = -\Delta Q_G = -\frac{\epsilon_1}{d_1 + \Delta d} [V_G - V_T - V_c] \quad (7)$$

where the threshold voltage is defined as $V_T = \phi_B - (\Delta E_C/q) + E_{F0} - V_b^0$, and the corresponding effective distance of the 2-DEG from heterointerface can be expressed as

$$\Delta d = \frac{\epsilon_1 \gamma}{q} \cdot n_s^{-1/3}. \quad (8)$$

This analytic expression is essentially the same as that derived by Stern [6] using a variational method.

III. RESULTS AND DISCUSSIONS

Fig. 2 shows a comparison of the fitted results of the linear approximation [2], the second-order polynomial expression [3], and (6) with an exact calculation of the triangular potential well approximation [1]. As seen in Fig. 2, (6) has a better fit with the exact E_F versus n_s characteristics than other approximate functions in all regions of operation of interest, where $E_{F0} = -0.062$ V and $\gamma = 0.385 \times 10^{-11}$. The corresponding effective distance of the 2-DEG from heterointerface is also compared with the constant effective distance used in [2]. The results indicate that the variation of the effective distance over the operation range significantly affects the characterization of the charge control of the 2-DEG in HEMT structure.

To further confirm the effectiveness and consistency of this model, the numerical calculations of electron energy levels in a GaAs/Ga_{1-x}Al_xAs heterostructure by exact quantum mechanical model [7] are included for comparison with the results of our model and are illustrated in Fig. 3, where $E_{F0} = -57.0$ mV and $\gamma = 0.298 \times 10^{-8}$. The slight difference between these two curves in the low carrier concentration region is caused mainly by the subthreshold effect in which the variation is logarithmic in nature. The plot of corresponding effective distances shows that without introducing an additional fitting parameter in (8) the approximation is very close to the numerical results of the quantum mechanical model and indicates that the extended model is more accurate as far as the nonlinearity of charge control of the 2-DEG is concerned. Moloney *et al.* [8] have also given a similar approximation for the Fermi energy versus carrier concentration of the 2-DEG while modeling the $C-V$ characteristics of HEMT's, in which a functional dependence like the second term in (5) was assumed dominant at room temperature rather than the third one. The fits based on this formula, as shown in Fig. 3, are fairly good at first sight even in the low carrier concentration region. However, the corresponding effective distances of the 2-DEG from the heterojunction deviate considerably from the

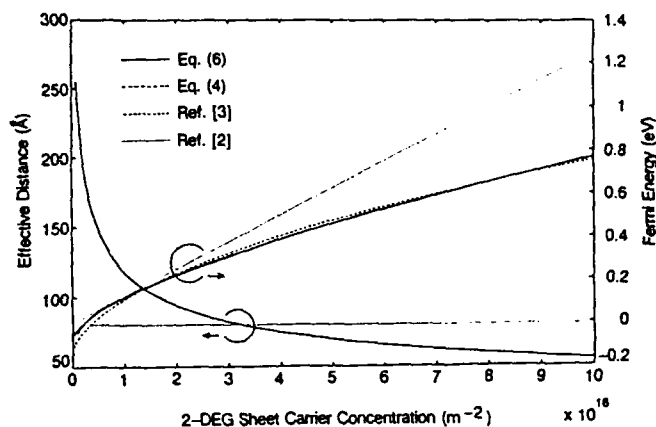


Fig. 2. Comparison of some approximate expressions on Fermi energy versus sheet carrier concentration of 2-DEG channel at 300 K and the corresponding effective distance of 2-DEG from the heterointerface. Note the results of (6) almost overlap those calculated from the triangular potential well approximation.

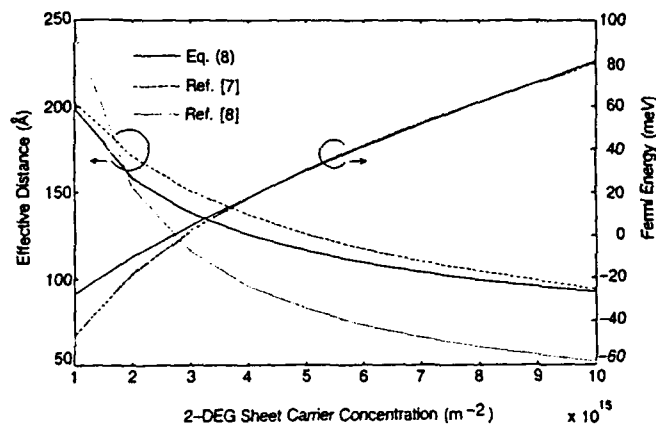


Fig. 3. Comparison of the exact numerical solution and the approximate models on Fermi potential versus 2-DEG density in a GaAs/AlGaAs heterojunction and the corresponding effective distance versus 2-DEG concentration.

results of the exact numerical model. This comparison reveals the importance of the extraction of a proper functional dependence for the analytic fitting expression from a detailed physical analysis to ensure the consistency of the formulation.

In conclusion, a better general agreement with the exact calculation of the quantum mechanical model indicates that the extended model provides a realistic description of the 2-DEG charge control of a HEMT structure. Further, the simplicity of this model makes it well suited for use in analytic modeling of HEMT's. It has been successfully applied to predicting the I - V characteristics of pseudomorphic InGaAs/GaAs HEMT's with satisfactory agreement with the experimental data over a wide operation regime.

ACKNOWLEDGMENT

The authors would like to thank Prof. H. H. Wieder and Dr. G. Witt for their support and very helpful discussions.

REFERENCES

- [1] D. Delagebeaudeuf and N. T. Linh, "Metal-(n)AlGaAs-GaAs two dimensional electron gas FET," *IEEE Trans. Electron Devices*, vol. ED-29, pp. 955-960, 1982.
- [2] T. J. Drummond, H. Morkoç, K. Lee, and M. Shur, "Model for modulation doped field effect transistor," *IEEE Electron Device Lett.*, vol. EDL-3, pp. 338-341, 1982.
- [3] S. Kola, J. M. Goloio, and G. N. Maracas, "An analytical expression for Fermi level versus sheet carrier concentration for HEMT modeling," *IEEE Electron Device Lett.*, vol. 9, pp. 136-138, 1988.
- [4] A. N. Khondker, A. F. M. Anwar, M. A. Islam, L. Limoncelli, and D. Wilson, "Charge control mechanism in MODFET's: A theoretical analysis," *IEEE Trans. Electron Devices*, vol. ED-33, pp. 1825-1826, 1986.
- [5] J. Yoshida, "Classical versus quantum mechanical calculation of the electron distribution at the n-AlGaAs/GaAs heterointerface," *IEEE Trans. Electron Devices*, vol. ED-33, pp. 154-156, 1986.
- [6] F. Stern, "Self-consistent results for n-type Si inversion layers," *Phys. Rev. B*, vol. 5, pp. 4891-4899, 1972.
- [7] F. Stern and S. D. Sarma, "Electron energy levels in GaAs-Ga_{1-x}Al_xAs heterojunctions," *Phys. Rev. B*, vol. 30, pp. 840-848, 1984.
- [8] M. J. Moloney, F. Ponce, and H. Morkoç, "Gate capacitance-voltage characteristic of MODFET's: Its effect on transconductance," *IEEE Trans. Electron Devices*, vol. ED-32, pp. 1675-1684, 1985.

Appendix B

An Analytical Current-Voltage Characteristics Model the High Electron Mobility Transistors Based on Nonlinear Charge Control Formulation *

* Accepted for publication in the upcoming special issue of the *IEEE Trans. Electron Devices*, on Heterostructure Transistors, October 1989.

An Analytical Current-Voltage Characteristics Model for the High Electron Mobility Transistors Based on Nonlinear Charge-Control Formulation *

An-Jui Shey and Walter H. Ku

Department of Electrical and Computer Engineering
University of California, San Diego, R-007
La Jolla, CA 92093
(619)534-2717

Abstract

Consideration of nonlinear variation of the sheet carrier concentration of the Two-Dimensional Electron Gas (2-DEG) with Fermi potential in the quasi-triangular potential quantum well of the HEMT structure has led to a bias-dependent effective offset distance of the 2-DEG from the heterointerface. The inclusion of the variable 2-DEG offset distance allows model characterization of the charge-control mechanism in a more consistent manner, and with greater accuracy, than the conventional linear charge-control model does. Based on the nonlinear charge-control formulation, we developed an accurate analytical drain current-voltage characteristics model for HEMT device. This model is valid over a very wide range of operation, extending from near-subthreshold regime to high parasitic MESFET conduction regime. This model also includes the broadening effect of the 2-DEG quantum well in the pinchoff regime, providing a more accurate description of current saturation mechanism. We demonstrate the effectiveness and accuracy of this model by comparing measured and modeled dc characteristics of normally-on as well as normally-off HEMT devices. Furthermore, the simple analytical expressions make the model very suitable for CAD applications in the analysis and design of high-frequency microwave and high-speed digital HEMT devices and integrated circuits.

* This research is supported by AFOSR, Boiling Air Force Base, DC, under Grant No. AFOSR-86-0339, monitored by Dr. Gerald Witt.

Introduction

Since it was demonstrated in 1980, the High Electron Mobility Transistor (HEMT), a field-effect transistor that takes advantage of the novel properties of the two-dimensional electron gas formed at the heterojunction, has shown very promising performance for both high-frequency microwave and high-speed digital circuit applications. In order to optimize the performance of HEMT devices and circuits, many analytical models for HEMT's based on a simple linear charge-control model have been proposed [1-5]. These models are similar to that for conventional MOSFET's with only the gate insulator layer being replaced by a fully depleted doped semiconductor layer. These models, however, show a limited range of validity, basically because of the inaccurate assumption of linear charge-control for the modulation of the 2-DEG channel charge by the external bias. Thus, more accurate and realistic models are clearly needed.

The inaccuracy of linear charge-control modeling of the HEMT operation could stem from the improper estimation of the effective offset distance of the 2-DEG channel from the heterointerface, especially in the pinchoff regime. Hughes *et al.*[6] pointed out the important effects of nonlinear characteristics of the charge-control model on the evaluation of transconductance. Taking into account the variable 2-DEG offset distance from the heterojunction by numerical calculation, they obtained a fair agreement between the calculated and measured transconductance characteristics over a wide operation range. However, the derivation of this model is not explicit in terms of the physical parameters, and the numerical solution is too complicated for applications in the analysis and design of integrated circuits.

Recently, Kola *et al.* [7] proposed a data fitting expression for the Fermi potential versus 2-DEG sheet carrier concentration that would take into consideration the variation of the Fermi level in the 2-DEG channel with the externally applied bias. In order to avoid a sophisticated data fitting process and to provide a direct physical insight into the operation of the device, we have developed a simple but more accurate nonlinear charge-control model[8], which is derived directly from the triangular potential well approximation. Based on the analytical nonlinear charge-control model, we further developed an analytical HEMT drain current-voltage characteristics model, in which the gain compression phenomena appeared near the pinchoff region and in the high parasitic MESFET conduction region are more accurately described.

Charge-Control Model

The first proposed conventional charge-control model [1] derived from Poisson's equation for HEMT's neglected the Fermi-potential term. The resultant model (see the energy band diagrams in Fig. 1) shows that the channel carrier concentration depends linearly on the gate bias.

$$qn_s = \frac{\epsilon_1}{d_1} [V_G - V_T] \quad (1)$$

$$V_T = \phi_B - \frac{\Delta E_C}{q} - \frac{qN_{D1}}{2\epsilon_1} (d_1 - d_c)^2 \quad (2)$$

where n_s is the 2-DEG sheet carrier concentration; ϵ_1 and d_1 are the permittivity and thickness of the electron supply layer with a wider energy-band gap, respectively; q is the electronic charge; V_G is the gate-source biased voltage; ϕ_B is the barrier height of the Schottky-gate; ΔE_C is the conduction band discontinuity at heterojunction; N_{D1} is the doping concentration in the electron supply layer; d_c is the spacer layer thickness. Note that subscript 1 refers to the parameters associated with the electron supply layer with a wider energy-band gap and subscript 2 for the 2-DEG channel layer.

Drummond *et al.*[2] extended this model to include the variation of the 2-DEG Fermi potential gas with the sheet carrier concentration. A linear approximation,

$$V_F = V_{F0} + a n_s , \quad (3)$$

yields the linear charge-control formulation used by most of the existing analytical models,

$$qn_s = \frac{\epsilon_1}{d_1 + \Delta d} [V_G - V_{F0} - V_T] , \quad (4)$$

where V_{F0} is the equilibrium Fermi potential; and Δd is the corresponding offset distance of the 2-DEG from heterointerface. Δd is assumed to be a constant value, i.e.,

$$\Delta d = \frac{\epsilon_1 a}{q} \approx 80 \text{ \AA} \quad (5)$$

This model was further modified in [6] to take into account the nonlinear dependence of the average position of the 2-DEG channel, Δd , from heterointerface on the gate bias. The 2-DEG offset distance is calculated from the weighted average distance of all energy levels,

$$\Delta d = \frac{\frac{2}{3} \sum_n n_{sn} d_n}{n_s} \quad n = 0, 1, 2, 3, \dots \quad (6)$$

where n_{sn} and d_n are the density and average distance from the heterointerface of carriers in the n -th subband, respectively. The total carrier concentration n_s in the 2-DEG channel is a sum of all occupancy of energy states at various energy levels,

$$n_s = \sum_n n_{sn} \quad n = 0, 1, 2, 3, \dots \quad (7)$$

However, the computation process is too involved to be useful in the CAD environment.

In the triangular potential well approximation, if only the lower and the first excited subbands are considered, the relation between the 2-DEG sheet concentration n_s and the Fermi-level can be expressed as

$$E_F = (kT) \ln \left\{ -\frac{1}{2} \left[e^{\frac{q}{kT} \gamma_0 n_s^{\frac{2}{3}}} + e^{\frac{q}{kT} \gamma_1 n_s^{\frac{2}{3}}} \right] + \left[\frac{1}{4} \left[e^{\frac{q}{kT} \gamma_1 n_s^{\frac{2}{3}}} - e^{\frac{q}{kT} \gamma_0 n_s^{\frac{2}{3}}} \right]^2 + e^{\frac{qn_s}{DkT}} e^{\frac{q}{kT} (\gamma_0 + \gamma_1) n_s^{\frac{2}{3}}} \right]^{\frac{1}{2}} \right\} \quad (8)$$

where D is the density of states of the 2-DEG; γ_0 and γ_1 are material parameters of the 2-DEG channel layer, usually estimated from results of resonance experiments [1]. γ_0 and γ_1 link the 2-DEG carrier density with the longitudinal quantized energy through the equations

$$E_0 = \gamma_0 n_s^{2/3}$$

$$E_1 = \gamma_1 n_s^{2/3}$$

For moderate values of n_s , the argument of the exponential terms is small, and a series expansion of these terms in (8) converges. We can then approximate the Fermi energy E_F by

$$E_F \approx (kT) \ln \left(\frac{qn_s}{2DkT} \right) + \frac{qD}{4} (\gamma_1 - \gamma_0)^2 n_s^{\frac{1}{3}} + q(\gamma_0 + \gamma_1) n_s^{\frac{2}{3}} \quad (9)$$

In the normal operation region the third term dominates and the first two terms can be considered to be constants that can be evaluated at the equilibrium carrier concentration n_{s0} . Therefore, we have a further simplified form

$$E_F = E_{F0} + \gamma n_s^{\frac{2}{3}} \quad (10)$$

This approximation holds as long as the device is not operated in the deep subthreshold region, where the quantization effect is of minor importance because the potential well broadens remarkably and the subbands are closely spaced. An advantage of using (10) is that only two adjustable parameters are involved. They can be determined from estimated values in the corresponding terms in (9). This requires much less effort when compared to other data fitting expressions. Fig. 2 shows plots of the fitted results of the linear approximation[2], the second-order polynomial expression[7], and (10) together with an exact solution of the triangular potential well approximation under the assumption of negligible background impurities [1]. The expression in (10) clearly shows a better description of E_F versus n_s characteristics in all regions of interest, where $E_{F0} = -0.062$ eV and $\gamma = 0.385 \times 10^{-11}$ eV·m^{4/3}.

Substituting (10) into (1) and rearranging terms, we can express the 2-DEG sheet carrier concentration as

$$n_s = \frac{\beta}{[1 + \xi n_s^{-1/3}]} [V_G - V_{T0} - V], \quad (11)$$

where V is the channel potential. The threshold voltage V_{T0} , the linear charge-control coefficient β , and the offset distance coefficient ξ are separately defined as

$$V_{T0} = \phi_B - \frac{\Delta E_C}{q} + E_{F0} - \frac{qN_{D1}}{2\epsilon_1} (d_1 - d_e)^2 \quad (12)$$

$$\beta = \frac{\epsilon_1}{qd_1} \quad (13)$$

$$\xi = \frac{\epsilon_1 \gamma}{qd_1} = \gamma \beta \quad (14)$$

It is interesting to note that, from comparing (11) and (4), the corresponding offset distance of the 2-DEG, Δd , from the heterojunction is proportional to $n_s^{-1/3}$, which is essentially the same as the results derived by Stern [9] using a variational method. In fact, the key feature of our new nonlinear charge-control model is the inclusion of the nonlinear dependence of the offset distance of the 2-DEG channel on the 2-DEG sheet carrier concentration. This offset distance will affect the transconductance performance significantly[6]. Fig. 3 shows plots of the corresponding offset distances of the 2-DEG as calculated by the above expression, the linear charge-control model, and exact quantum mechanical model [10]. Without additional fitting parameters in (11), our approximation of the effective offset distance of 2-DEG is very close to the numerical results of the quantum mechanical model, with a maximum discrepancy of less than 10 Å.

Drain I - V Characteristics Model

1. Empirical Velocity versus Electrical Field Model

Experimental measurement has shown the velocity saturation phenomenon in III - V compound material at high fields. To take velocity saturation into account, the following functional form is commonly employed in numerical models for depicting velocity versus electrical field curve.

$$v(E) = \frac{\mu E + v_{sat} \left(\frac{E}{E_C} \right)^n}{1 + \left(\frac{E}{E_C} \right)^n} \quad (15)$$

where μ is the low-field mobility; v_{sat} is the saturation velocity; E_C is the electrical field corresponding to the peak velocity; $n = 4$ is found to give the best fit to the experimental data. In

order to obtain an analytical solution, we set $n = 1$ for both the parasitic MESFET channel and the two-dimensional electron gas channel, i.e.,

$$v(E) = \frac{(\mu + \frac{v_{sat}}{E_C}) E}{1 + \frac{E}{E_C}} \quad E \leq E_S \quad (16)$$

$$= v_{sat} \quad E \geq E_S \quad (17)$$

where the electrical field E_S at the onset of velocity saturation is determined by the equation

$$E_S = \frac{v_{sat}}{\mu} \quad (18)$$

2. The Threshold of the Parasitic MESFET Conduction

In the normal operation mode of HEMT's, the depletion of the doped layer is from the charge transfer and the Schottky gate depletion. At thermal equilibrium the undepleted channel width of the parasitic MESFET, h , as shown in Fig. 1, is

$$h = (d_1 - d_e) - \frac{n_s}{N_{D1}} - \left[\frac{2\epsilon_1}{qN_{D1}} (\phi_B - V_n - V_G) \right]^{\frac{1}{2}} \quad (19)$$

where V_n is the potential difference between the conduction band edge and the Fermi-energy in the neutral carrier supply layer.

The threshold voltage V_C of the parasitic MESFET's conduction can be easily evaluated by letting $h = 0$. Then

$$V_C = \phi_B - V_n - \frac{qN_{D1}}{2\epsilon_1} (d_1 - d_e - \frac{n_{s0}}{N_{D1}})^2 \quad (20)$$

3. Intrinsic HEMT Operation Mode ($V_G < V_C$)

(a) Linear Region ($V_D < V_{sat}$)

When the applied drain voltage is not high enough to accelerate carriers up to saturation velocity, the drain current can be evaluated by combining (11) and (16) and using a one-step substitution approximation for the 2-DEG sheet carrier concentration. We then obtain

$$I_D = Wqn_s v$$

$$= \frac{Wq\beta\mu_2[V_G - V_{T0} - V]}{[1 + \eta(V_G - V_{T0} - V)^{-1/3}]} \frac{E}{1 + \frac{E}{E_{C2}}} \quad (21)$$

where W is the gate width; L is the nominal gate length; η ($= \gamma\beta^{2/3}$) is the nonlinear charge-control coefficient; V is the channel potential; E_{C2} is the characteristic electric field used in (16) for the 2-DEG case.

Let y define the inverse offset distance variable as a function of channel potential for the 2-DEG channel by

$$y = [V_G - V_{T0} - V]^{1/3} \quad (22)$$

The boundary conditions on the 2-DEG channel require that $V(x)$ equal zero at $x = 0$ and V_D at $x = L$, which correspond to

$$y_0 = [V_G - V_{T0}]^{1/3} \quad (23)$$

$$y_D = [V_G - V_{T0} - V_D]^{1/3} \quad (24)$$

Substituting (22) into (21) and integrating y from y_0 to y_D and x from 0 to L , we obtain the drain 2-DEG current below saturation given by

$$I_D = -\frac{3A_2}{(1 + \frac{V_D}{B_2})} \left\{ \sum_{n=1}^6 \left[\frac{(-1)^n}{n} \eta^{(6-n)} (y_D^6 - y_0^6) \right] + \eta^6 \ln \left[\frac{y_D + \eta}{y_0 + \eta} \right] \right\} \quad (25)$$

where A_2 and B_2 are defined as

$$A_2 = \frac{W\mu_2q\beta}{L} \quad (26)$$

$$B_2 = LE_{C2} \quad (27)$$

(b) Saturation Region ($V_D \geq V_{sat}$)

When the 2-DEG carriers are accelerated to the saturation velocity by the longitudinal electrical field parallel to the current flow, the 2-DEG channel current in the saturation region is expressed in the equation

$$I_D = Wq\beta \frac{(V_G - V_{T0} - V_{sat})}{[1 + \eta(V_G - V_{T0} - V_{sat})^{-1/3}]} v_{sat}^2 \quad (28)$$

The velocity of the electrons in the channel reaches saturation at the point $x = L_s$. Further increase in drain bias will increase the electrical field along the channel and cause the electrons to

reach velocity saturation at a point closer to the source electrode, i.e., reducing the effective length L_s . By requiring the current continuity between the linear regime and saturation regime, we arrive at the expression for the length L_s of the linear channel region

$$L_s = -\frac{V_{sat}}{E_{C2}} - 3\left(\frac{E_{C2} + E_{S2}}{E_{C2}E_{S2}}\right)\left(\frac{y_s + \eta}{y_s^4}\right) \left\{ \sum_{n=1}^6 \left[\frac{(-1)^n}{n} \eta^{(6-n)} (y_s^n - y_0^n) \right] + \eta^6 \ln \left[\frac{y_s + \eta}{y_0 + \eta} \right] \right\} \quad (29)$$

where the voltage drop, V_{sat} , across L_s is

$$V_{sat} = V_G - V_{T0} - y_s^3 \quad (30)$$

4. Current Saturation Mechanism

To determine L_s and V_{sat} , one can solve the two-dimensional Poisson's equation in the pinchoff region by using self-consistent approach and keep the lowest space harmonic of the approximation solution along the boundary [11]. The approximation yields the relation between L_s and V_{sat} as

$$V_D - V_{sat} = \frac{2d_{sat}E_{S2}}{\pi} \sinh \left[\frac{\pi(L - L_s)}{2d_{sat}} \right] \quad (31)$$

Note that due to the nonlinear charge-control mechanism, the effective distance of the saturated 2-DEG channel from the gate electrode is a function of potential at L_s , namely,

$$d_{sat} = d_l \left[1 + \eta (V_G - V_{T0} - V_{sat})^{-1/3} \right] \quad (32)$$

As illustrated in Fig. 4, in the saturation region the high saturation voltage reduces the depth of the quasi-triangular quantum well, and the 2-DEG channel becomes broader at the drain side. This is equivalent to an increase in the offset distance of the 2-DEG channel from the heterojunction. This phenomenon could be observed in the electron density distribution plot in a two-dimensional numerical HEMT model, e.g., [12,13].

The value of y_s as a function V_G and V_D can be easily found by combining (29)-(32) and using a simple Newton's rooting method in a few iterations with the initial value set as y_0 . Once y_s is known, the drain current can be calculated directly from (28).

5. The Consideration of Parasitic Components

Once the gate voltage is larger than V_C , the parasitic MESFET channel starts conduction, i.e. the carrier supplying layer is not fully depleted, leading to current contribution from the 2-

DEG channel as well as the parasitic MESFET channel underneath the Schottky gate. The calculation of parasitic MESFET conduction current is very similar to that derived in [5]. The detailed derivation is shown in the Appendix.

The intrinsic HEMT model does not explicitly include the parasitic resistances R_S and R_D on the source and drain sides. To take these parasitic resistances into account, we can calculate the intrinsic HEMT bias voltages V_G and V_D by solving the equations

$$V_D = V_{ds} - I_D (R_S + R_D) \quad (31)$$

$$V_G = V_{gs} - I_D R_S \quad (32)$$

where V_{ds} and V_{gs} are the terminal voltages at the drain and gate electrodes relative to the source contact.

Results and Discussion

To show the accuracy and effectiveness of our nonlinear charge-control model, we compare our calculated drain current-voltage characteristics with experimental measurements of a normally-off HEMT and a normally-on HEMT reported by Drummond *et al.* [2] and Lee *et al.* [3], respectively, which are two typical samples commonly cited by the linear models reported in the literature. The parameters used for the modeling are summarized in Table 1. Fig. 5 shows the I-V curves of a normally-off HEMT with 1 μm gate length from our model and from a linear charge-control model in conjunction with a two-piece velocity model. As seen in Fig. 5, our modeled results are in good agreement with the experimental data. Here, the device size, R_s , μ , and N_{D1} are measured values. Moreover, we do not need to add a resistance parallel to the channel as in [4], in order to fit drain I-V curves in the saturation region for this 1 μm gate HEMT. As indicated in the electron density distribution plots of a two-dimensional numerical simulation [12,13], the carriers in the saturation region (fewer compared to those in the linear region) are further repelled from the heterojunction toward the substrate by the gate field. When fitting the drain current curves in the saturation region, because of the basic assumption of constant offset distance, the linear model includes only the current contributed by the carriers within the constant effective distance from heterointerface and leaves out others. Therefore, R_s or μ values different from measured data and a parallel conductance are required in the linear model to take into account the conduction current contributed by those 2-DEG carriers with larger offset distance. Note that this current component is often interpreted as the substrate current or leakage current in the linear model. Since the channel broadening of the quantum well in the saturation region has been included in the nonlinear model by using the bias dependent effective offset distance, a more accurate estimation of carrier concentration in the 2-DEG channel is obtained. This results

in a more accurate prediction of the drain saturation current by present model as compared to that calculated by a linear model. As theoretical estimation or experimental measurement of saturation velocity, v_{sat} , of 2-DEG in the quantum well has not been widely reported, we use the simulation values calculated by Monte Carlo method [14].

Fig. 6 shows the experimental data of a normally-on HEMT, our calculation, and the modeled results by a linear charge-control model using a three-piece velocity model. The parameter values used for modeling are also listed in Table 1, where R_s and μ are measured values. It can be seen that the accuracy of the derived I-V characteristics is quite satisfactory when the nonlinear modulation effect is included in the charge-control formulation. Fig. 7 shows the calculated and measured saturation drain current as a function of gate voltage. In the near subthreshold region, our results agree very well with experimental data, due to the more accurate nonlinear charge-control description embedded in the drain I-V characteristics model. The existing linear models usually underestimate the 2-DEG sheet carrier concentration and fail in the near subthreshold region.

Using a logarithm functional form similar to that of the first term in (9), which proved to be dominant in the subthreshold regime, a refinement in modeling the nonlinear charge-control could further extend the validity of the present model into the subthreshold region.

Conclusion

We have developed an analytical HEMT model based on a simple nonlinear charge-control formulation that explicitly takes into account the variation of the 2-DEG offset distance from heterointerface as a function of bias. The validity of the analytical charge-control model is supported by the results of a self-consistent quantum mechanical model. The I-V characteristics can be expressed in a simple analytical form, making it very suitable for the analysis and computer-aided design of microwave and high-speed HEMT integrated circuits. In addition, although the derived model is still in an approximate form, the modeled results are in fair agreement with experimental data. The model can therefore be applied to optimize device performance.

Appendix

Inclusion of Parasitic MESFET Conduction Model ($V_G \geq V_C$)

Consider the case where the MESFET channel is pinched off at $x = L_M$ by the gate bias. The channel potential at this point is

$$V_M = V_p - (\phi_B - V_n) + V_G, \quad (A1)$$

and the pinchoff voltage is given by

$$V_p = \frac{qN_{D1} (d_1 - d_e - \frac{n_{s0}}{N_{D1}})^2}{2\epsilon_1}. \quad (A2)$$

Within the conduction channel, wherever the channel potential is lower than V_M , the 2-DEG will not be perturbed by the gate and drain voltages and will stay at its thermal equilibrium values, n_{s0} , which can be estimated self-consistently by the equation

$$n_{s0} = \frac{\epsilon_1}{qd_1 [1 + \xi n_{s0}^{-1/3}]} \left[\phi_B - V_n - V_p - V_{T0} \right]. \quad (A3)$$

(a) Linear MESFET Channel ($V_D < V_M$)

The current flowing through the MESFET channel can be derived as in the conventional MESFET model.

$$I_1 = \frac{A_1}{(1 + \frac{V_D}{B_1})} \left\{ V_D - \frac{2}{3} \frac{(\phi_B - V_n - V_G + V_D)^{3/2} - (\phi_B - V_n - V_G)^{3/2}}{\sqrt{V_p}} \right\} \quad (A4)$$

where A_1 and B_1 are defined as

$$A_1 = \frac{Wq\mu_1 N_{D1}}{L} (d_1 - d_e - \frac{n_{s0}}{N_{D1}}) \quad (A5)$$

$$B_1 = LE_{C1} \quad (A6)$$

In the case of $V_D < V_M$, since the whole 2-DEG channel behaves like a linear resistor, the current flows through the 2-DEG channel is

$$I_2 = \frac{A_2(\phi_B - V_n - V_p - V_{T0}) V_D}{(1 + \frac{V_D}{B_2}) [1 + \xi n_{s0}^{-1/3}]} \quad (A7)$$

The total drain current I_D is

$$I_D = I_1 + I_2 \quad (\text{A8})$$

(b) Pinchoff MESFET Channel ($V_M < V_D < V_{sat}$)

The current due to the equilibrium two-dimensional electron gas can be calculated as in the linear region.

$$I_2 = \frac{LA_2 (\phi_B - V_n - V_p - V_{T0}) V_M}{(L_M + \frac{V_M}{E_2}) [1 + \xi n_{s0}^{-1/3}]} \quad (\text{A9})$$

The current flowing through the MESFET channel can be evaluated with the boundary condition, $V(L_M) = V_M$, and can be expressed as

$$I_1 = \frac{A_1 \left\{ V_M - \frac{2}{3} \left[V_p - \frac{(\phi_B - V_n - V_G)^{3/2}}{\sqrt{V_p}} \right] \right\}}{\left\{ \frac{A_2 [\phi_B - V_n - V_p - V_i]}{I_2 [1 + \xi n_{s0}^{-1/3}]} - \frac{1}{B_2} + \frac{1}{B_1} \right\} V_M} \quad (\text{A10})$$

Similar to the derivation in the normal operation mode, the 2-DEG current can be explicitly expressed as

$$I_2 = \frac{-3A_2}{(1 + \frac{V_D}{B_2})} \left\{ -\frac{V_M [\phi_B - V_n - V_p - V_{T0}]}{3[1 + \xi n_{s0}^{-1/3}]} + \sum_{n=1}^6 \left[\frac{(-1)^n}{n} \eta^{(6-n)} [y_D^n - y_M^n] \right] + \eta^6 \ln \left[\frac{y_D + \eta}{y_M + \eta} \right] \right\} \quad (\text{A11})$$

(c) Saturated MESFET Channel ($V_{sat} < V_D$)

In this operation region, formulation of the current flowing through the MESFET channel is identical to (A10). And the 2-DEG current is very similar to that in the pinchoff region and can be derived as

$$I_2 = \frac{-3A_2L}{(L_s + \frac{V_{sat}}{E_{C2}})} \left\{ -\frac{V_M [\phi_B - V_n - V_p - V_{T0}]}{3[1 + \xi n_{s0}^{-1/3}]} + \sum_{n=1}^6 \left[\frac{(-1)^n}{n} \eta^{(6-n)} (y_s^n - y_M^n) \right] + \eta^6 \ln \left[\frac{y_s + \eta}{y_M + \eta} \right] \right\} \quad (\text{A12})$$

Similarly, the variables L_s and V_{sat} can be solved from the following two equations, derived from current continuity requirement and from Poisson's equation in the saturation region with fixed boundary d_1 .

$$L_s = - \frac{(V_G - V_{T0} - y_s^3)}{E_{C2}} - 3 \left(\frac{E_{C2} + E_{S2}}{E_{C2} E_{S2}} \right) \left(\frac{y_s + \eta}{y_s^4} \right) \cdot$$

$$\left\{ \frac{V_M [\Phi_B - V_n - V_p - V_{T0}]}{3[1 + \xi n_s^{-1/3}]} + \sum_{n=1}^6 \left[\frac{(-1)^n}{n} \eta^{(6-n)} (y_s^n - y_0^n) \right] + \eta^6 \ln \left[\frac{y_s + \eta}{y_0 + \eta} \right] \right\} \quad (A13)$$

$$V_D - V_{sat} = \frac{2d_1 E_{S1}}{\pi} \sinh \left[\frac{\pi (L - L_s)}{2d_{sat}} \right] \quad (A14)$$

Acknowledgement

The authors would like to thank Prof. H. H. Wieder, Prof. Charles W. Tu, Norman Tien, and Dr. Gerald Witt for their support and very helpful discussions.

References

- [1] Daniel Delagebeaudeuf and Nuyen T. Linh, "Metal-(n) AlGaAs-GaAs Two-Dimensional Electron Gas FET," *IEEE Trans. on Electron Devices*, vol. ED-29, pp. 955-960, 1982.
- [2] T. J. Drummond, H. Morkoc, K. Lee, and M. Shur, "Model for Modulation Doped Field Effect Transistor," *IEEE Electron Device Letters*, vol. EDL-3, pp. 338-341, 1982.
- [3] K. Lee, M. Shur, T. J. Drummond, and H. Morkoc, "Current-Voltage and Capacitance-Voltage Characteristics of Modulation-Doped Field-Effect Transistors," *IEEE Trans. on Electron Devices*, vol. ED-30, pp. 207-212, 1983.
- [4] Margaret H. Weiler and Yalcin Ayasli, "DC and Microwave Models for $Al_xGa_{1-x}As/GaAs$ High Electron Mobility Transistors," *IEEE Trans. on Electron Devices*, vol. ED-31, pp. 1854-1861, 1984.
- [5] Guan-Wu Wang and Walter H. Ku, "An Analytical and Computer-Aided Model of the AlGaAs/GaAs High Electron Mobility Transistor," *IEEE Trans. on Electron Devices*, vol. ED-33, pp. 657-663, 1986.
- [6] William A. Hughes and Christopher M. Snowden, "Nonlinear Charge Control in AlGaAs/GaAs Modulation-Doped FET's," *IEEE Trans. on Electron Devices*, vol. ED-34, pp. 1617-1625, 1987.
- [7] S. Kola, J. M. Goloio, and G. N. Maracas, "An Analytical Expression for Fermi Level Versus Sheet Carrier Concentration for HEMT Modeling," *IEEE Electron Device Letters*, vol. EDL-9, pp. 136-138, 1988.
- [8] An-Jui Shey and Walter H. Ku, "On the Charge Control of the Two-Dimensional Electron Gas for Analytical Modeling of HEMT's," *IEEE Electron Device Letters*, vol. EDL-9, pp. 624-626, 1988.
- [9] F. Stern, "Self-Consistent Results for n-Type Si Inversion Layers," *Phys. Rev. B*, vol. 5, pp. 4891-4899, 1972.
- [10] F. Stern and S. D. Sarma, "Electron energy levels in GaAs-Ga $_{1-x}$ Al $_x$ As heterojunction," *Phys. Rev. B*, vol. 30, pp. 840-848, 1984.
- [11] A. B. Grebene and S. K. Ghandhi, "Signal and Noise Properties of Gallium Arsenic Microwave Field-Effect Transistors," *Solid-State Electronics*, vol. 12, pp. 573-589, 1969.
- [12] Dany Loret, "Two-Dimensional Numerical Model for the High Electron Mobility Transistor," *Solid-State Electronics*, vol. 30, pp. 1197-1203, 1987.
- [13] F. A. Buot, "Two-Dimensional Numerical Modelling of HEMT Using An Energy Transport Model," *COMPEL*, vol. 6, pp. 45-52, 1987.

- [14] G. Salmer, J. Zimmermann, and R. Fauquembergue, "Modeling of MODFET's," *IEEE Trans. on Microwave Theory Tech.*, vol. 36, pp. 1124-1140, 1988.

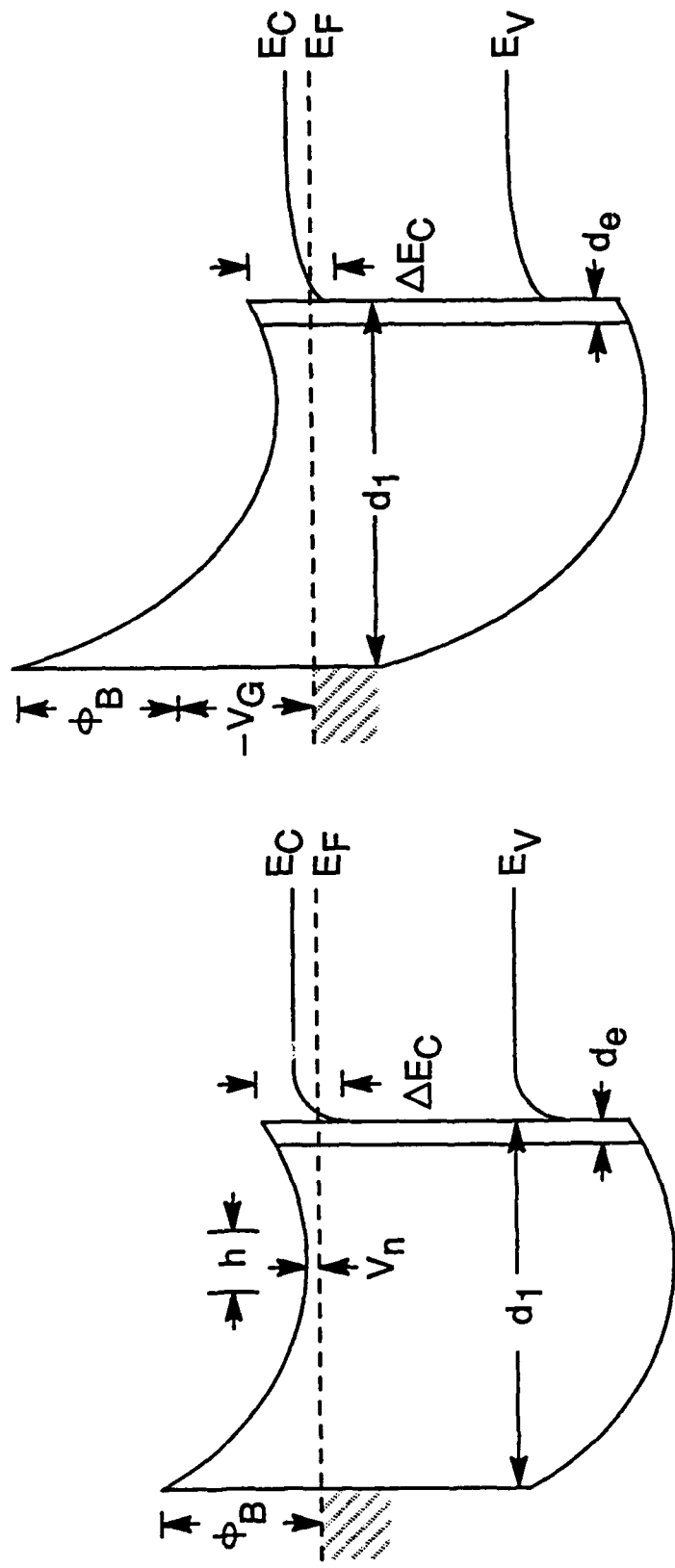
Figure Captions

- Fig. 1 Energy band diagrams of a normally-on HEMT on an n^- -type substrate (a) at thermal equilibrium and (b) in the 2-DEG charge-control regime.
- Fig. 2 Comparison of the exact numerical solution and the approximate models on the Fermi potential versus 2-DEG sheet carrier concentration in a GaAs/AlGaAs heterostructure at 300° K. Note that the fitted results of equation (10) are almost indistinguishable from the exact calculations.
- Fig. 3 The effective offset distance of the 2-DEG from the heterointerface as derived from the results shown in Fig. 2 by both the linear and nonlinear charge-control models.
- Fig. 4 Schematic diagram shows the 2-DEG channel spreads out toward the substrate in the saturation regime and the conduction of parasitic MESFET. The decrease of the 2-DEG sheet carrier concentration and the broadening of the quantum well result in an increase in the effective offset distance.
- Fig. 5 Measured and calculated drain current-voltage characteristics for a normally-off HEMT [2]. Solid line: present model. Dots: measured points. Dashed line: linear charge-control model with a two-piece velocity approximation.
- Fig. 6 Measured and modeled drain I-V characteristics of a normally-on HEMT [3]. Solid line: present model. Dots: measured points. Dashed line: linear charge-control model with a three-piece velocity approximation.
- Fig. 7 The calculated and experimental saturation drain current of a normally-on HEMT [3]. as a function of gate bias ($V_D = 1.5$ V). Solid line: present model. Dots: measured points.

Table 1

**The device parameters used by present model for modeling
the HEMT's**

Mode	Normally-OFF	Normally-ON	unit
L	1	1	μm
W	145	145	μm
d₁	400	410	Å
d_e	100	60	Å
V_{T0}	0.03	-0.99	V
ΔE_C	0.32	0.32	eV
ϕ_B	1.106	1.106	V
ϵ_1	12.2	12.2	ϵ_0
N_{D1}	1.0×10^{18}	1.0×10^{18}	cm^{-3}
μ	4300	6800	$\text{cm}^2/\text{V} \cdot \text{s}$
v_{sat}	2×10^7	5.7×10^7	cm/s
R_S	12	7	Ω
R_D	12	7	Ω



Thermal equilibrium

2-DEG charge control regime

Fig. 1

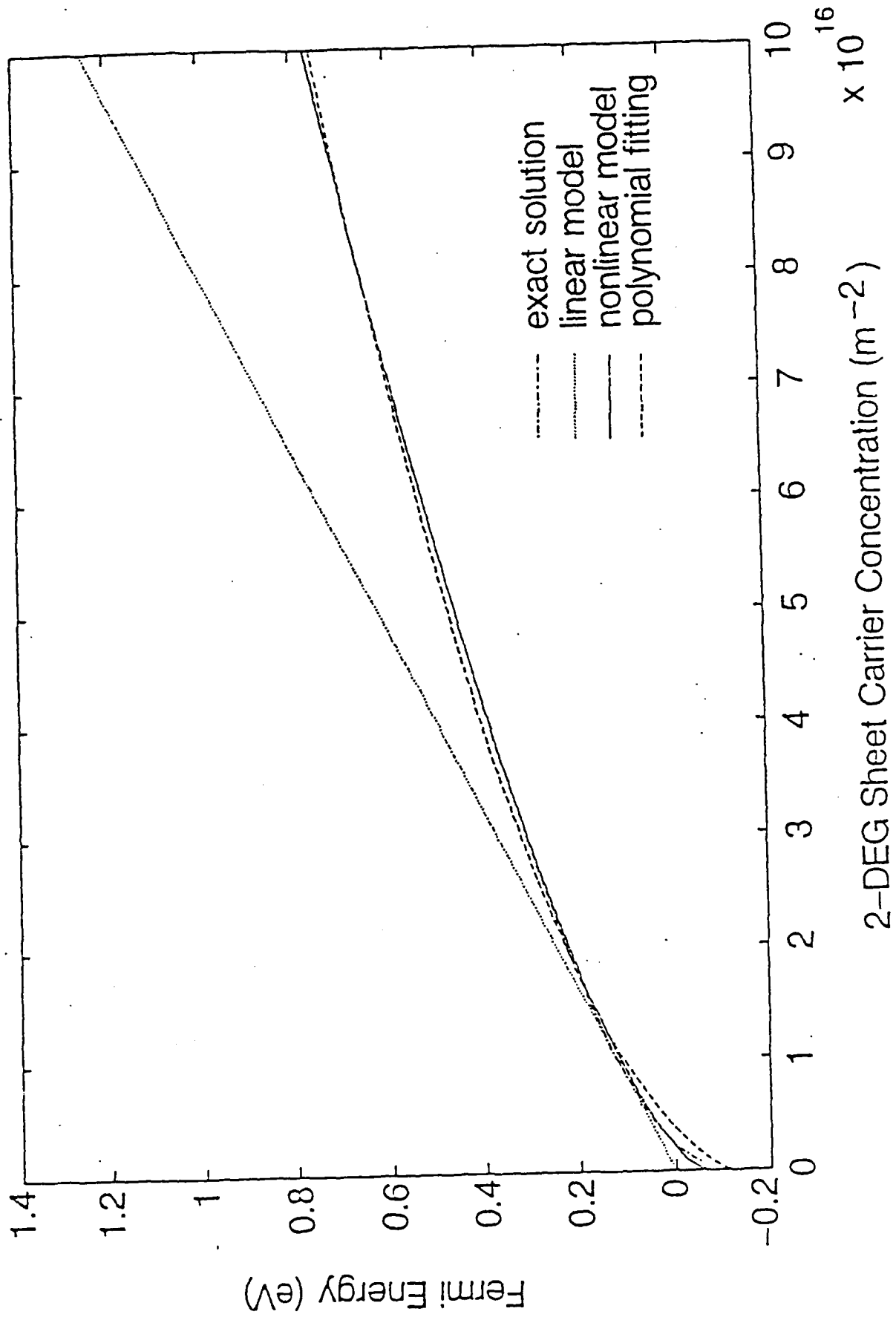


FIG. 2

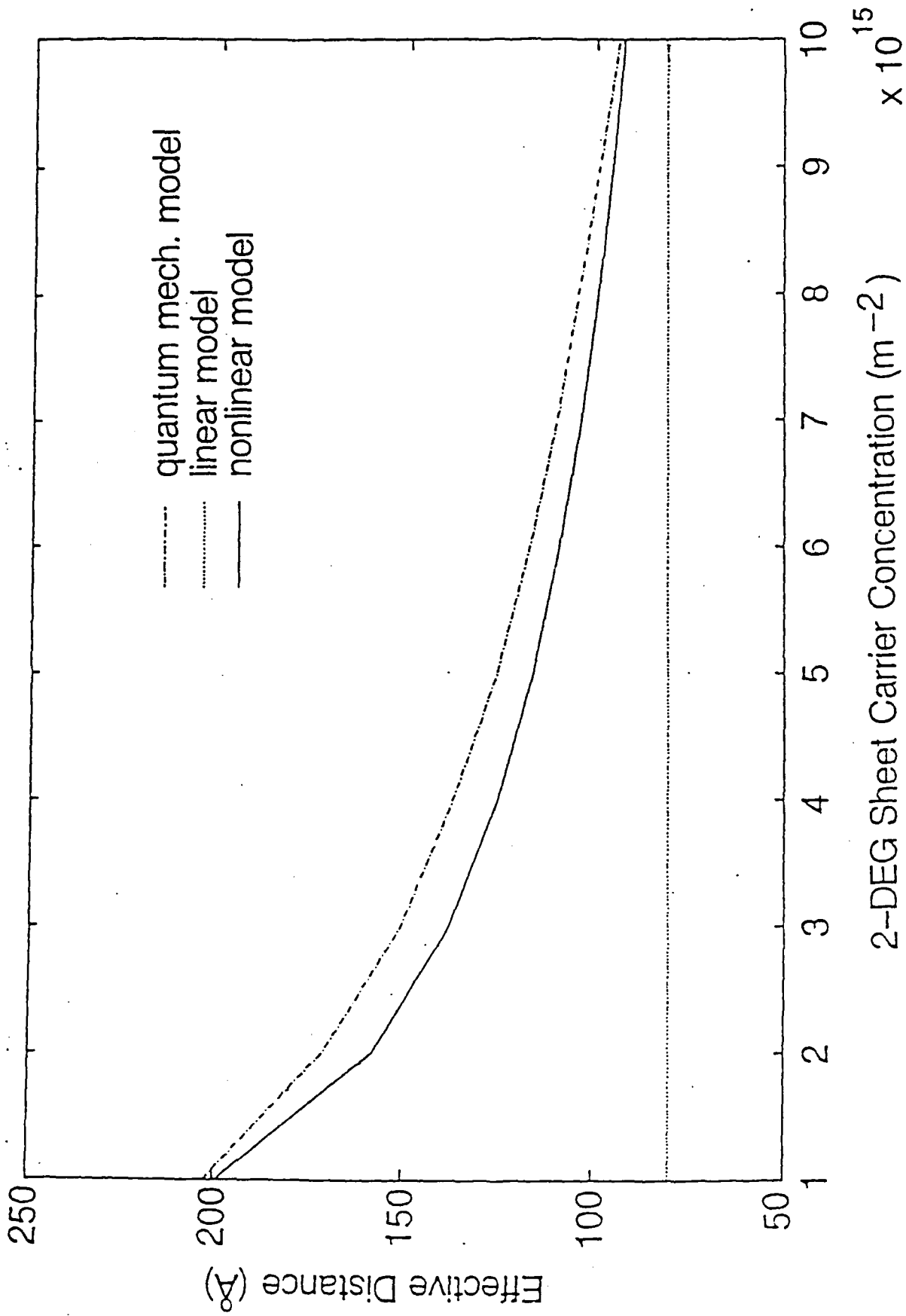


Fig. 3

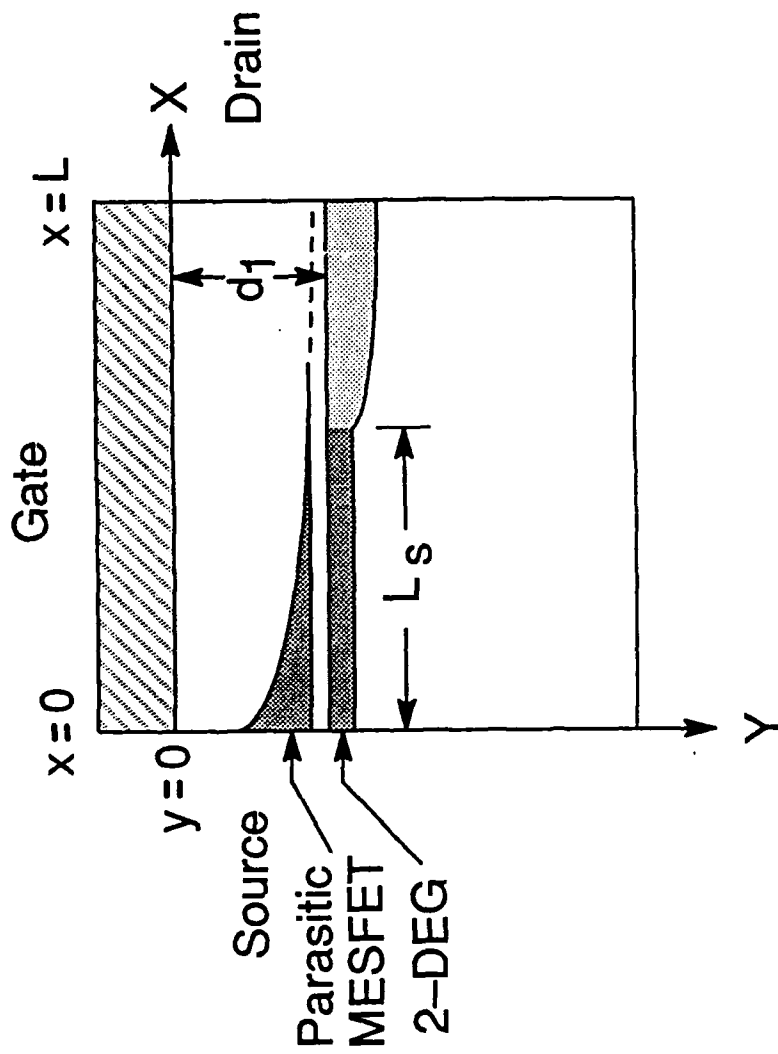


FIG. 4

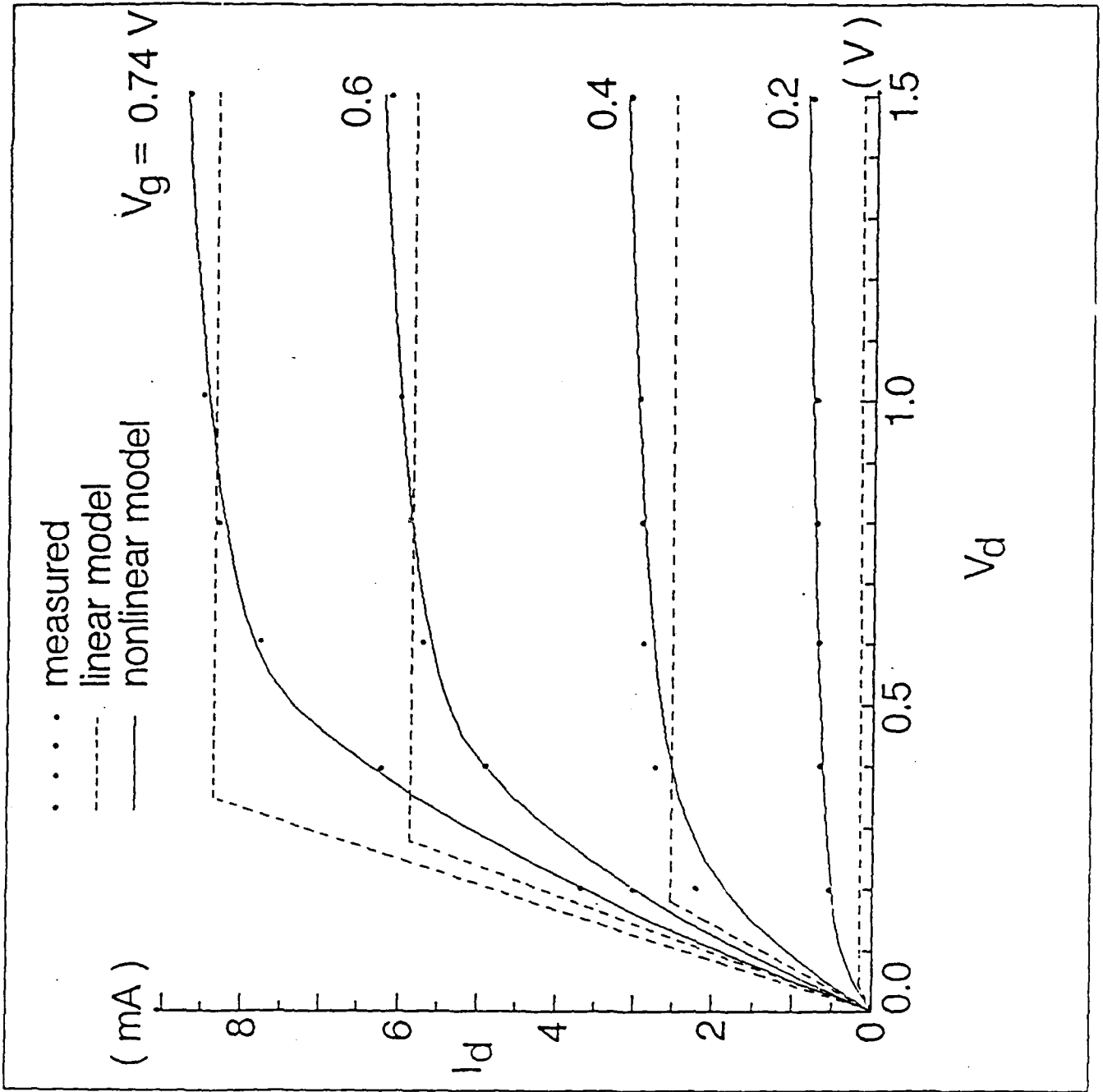


FIG. 5

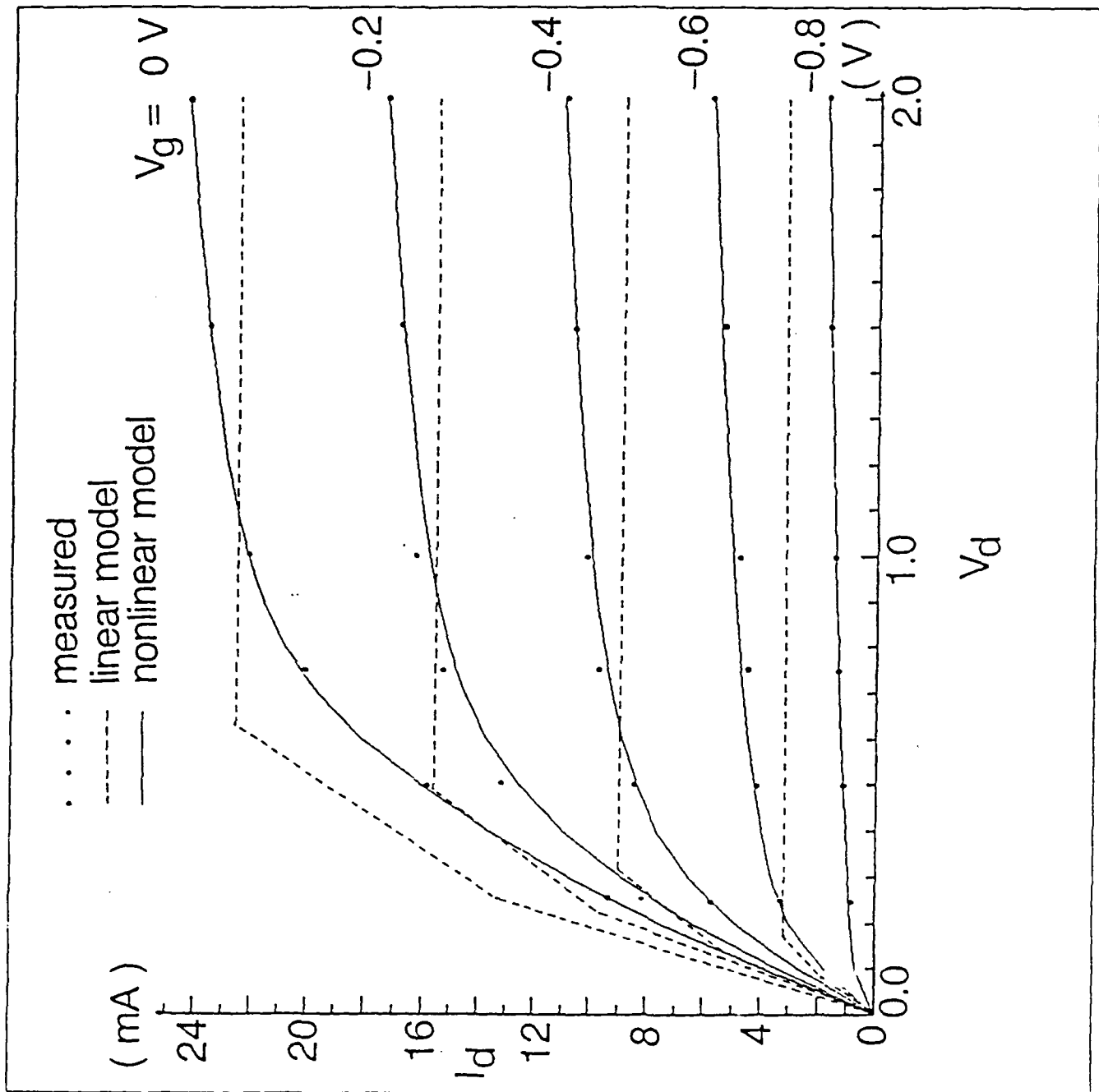


Fig. 6

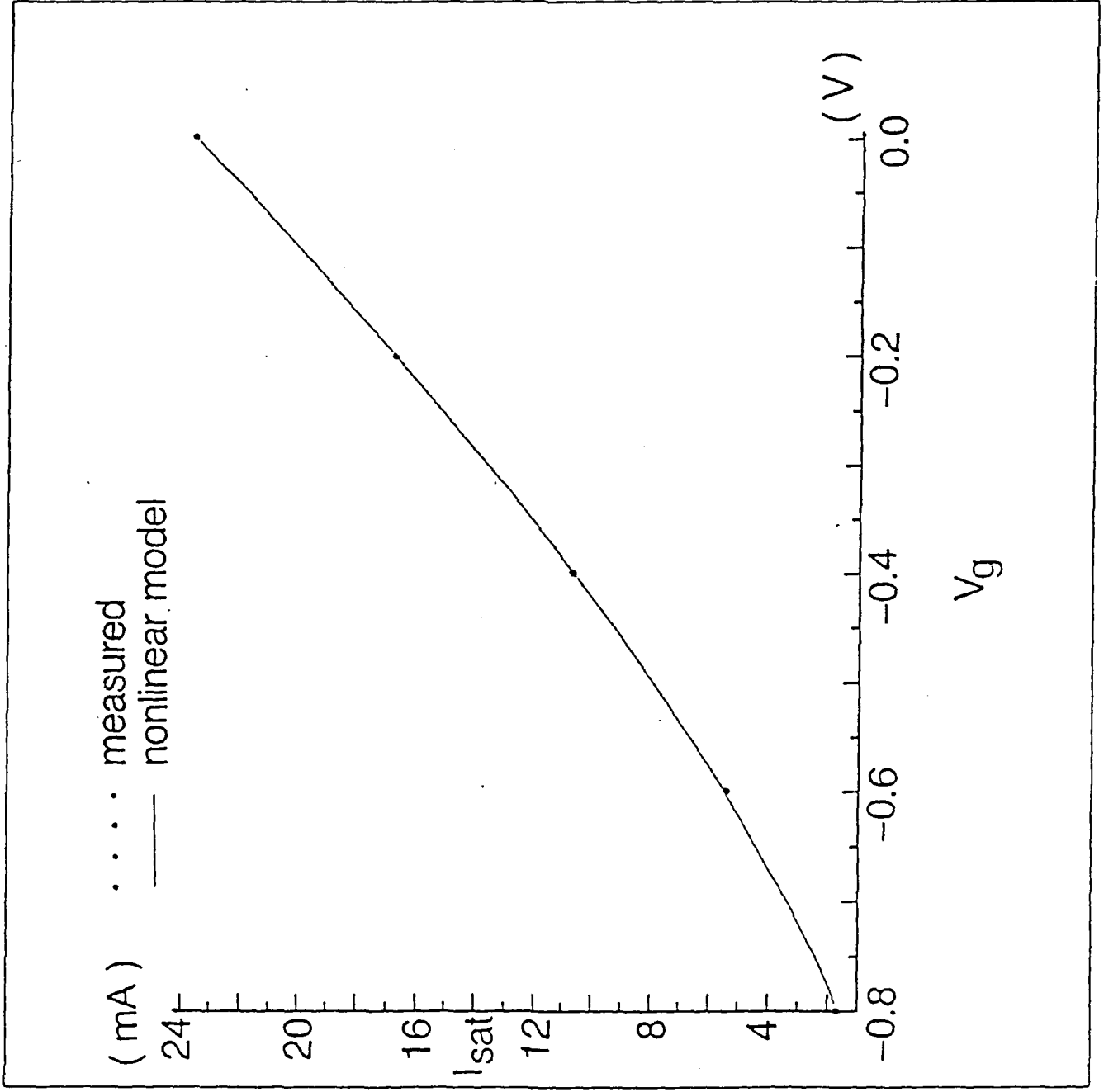


Fig. 7

Appendix C

Analytical and Computer-Aided Models of InP-Based MISFETs and Heterojunction Devices *

* Presented at *Joint NOSC/NRL InP Microwave/Millimeter Wave Technology Workshop*, San Diego, CA, January 25-26, 1989.

Analytical and Computer-Aided Models of InP-Based MISFETs and Heterojunction Devices

The superior properties of InP material, e.g., higher peak electron drift velocity, thermal conductivity, and breakdown field, to GaAs have made it an alternative for high performance applications in microwave and millimeter-wave regimes as well as high-speed digital circuits. Recently, a high-efficiency InP MISFET has demonstrated 4.5 watts output power with 4dB gain and 46% power-added efficiency at 9.7 GHz by Messick *et al* [15]. These impressive results clearly confirmed the promising superior performance of InP MISFETs.

The main concern in the applications of III-V MISFETs has been the reliability of output characteristics of the devices, which is mainly attributed to the variations of interfacial properties of the gate dielectric layer and the underlying semiconductor active layer. The task of modeling output characteristics of III-V compound-based MISFET devices has become complex with the possible dominance of the interfacial properties in the devices' performance. Much more attention should be paid to the nonlinear modulation of the surface potential by the external gate voltage due to the presence of an excessive amount of interfacial states, since the accompanying carrier trapping, scattering, and recombination could have altered completely the charge control and transport mechanisms, and consequently the device output characteristics.

Because of these factors, we have developed analytical and computer-aided models for depletion-mode and accumulation-mode MISFETs based on a nonlinear charge control model derived from semi-empirical surface potential formulation, which can provide us not only an accurate description of the drain I-V characteristics, but also a comprehensive study of the influence of interfacial properties on the output performance of InP MISFETs. Key aspects of the physics of this device, which relate to charge control, carrier trapping, and field-dependent mobility, are modeled in this study.

In order to further verify the calculated results and predict device performance in the submicron gate-length regime, we have developed a general-purpose finite element two-dimensional semiconductor device simulation program, which is able to analyze and simulate various device structures including homo- and hetero-junctions III-V compound semiconductor-based devices with arbitrary geometries. Preliminary simulation results of a 1 μm AlGaAs/GaAs HEMT device are reported. It is planned to extend the two-dimensional model to submicron InP MISFETs.

Appendix D

Two-Dimensional Semiconductor Device Analysis Based on New Finite-Element Discretization Employing the S-G Scheme

Two-Dimensional Semiconductor Device Analysis Based on New Finite-Element Discretization Employing the S-G Scheme

GEN-LIN TAN, XIAO-LI YUAN, QI-MING ZHANG, WALTER H. KU, AND AN-JUI SHEY

Abstract—The finite element method has been playing an important role in the solution of many engineering problems. To make the application of the finite element method practical in semiconductor device simulation, we have applied the Scharfetter-Gummel (S-G) scheme in conjunction with an accurate seven-point Gaussian Quadrature rule to the assembly of the finite-element stiffness matrices and right-hand side vector of the semiconductor equations, which has resulted in solutions with high accuracy even on coarse mesh as well as a significant speed-up of convergence rate.

I. INTRODUCTION

THE Scharfetter-Gummel scheme [1] has been widely used in the discretization of the continuity equations and has shown great suitability due to an inherent advantage of uniform convergence. However, to date the applications have been almost restricted to the finite difference method or its variants. The classical finite element method, by which the carrier densities are usually approximated in low order polynomial expansions [2], requires an excessively fine finite element mesh in order to achieve a reasonable approximation error. Additionally, it suffers a prohibitive convergence rate because of the large integration errors incurred due to the inaccurate low order polynomial approximations. Therefore, the classical finite element method is inferior to its finite difference counterpart employing the Scharfetter-Gummel (S-G) scheme in which the functional variation of carrier densities is exponential in nature, the so-called Box Integration Method (BIM-SG) [3], in the treatment of current continuity equations.

Manuscript received July 1, 1988; revised October 3, 1988 and January 3, 1989. This work was supported by AFOSR, Boiling Air Force Base, Washington, DC, under Grant AFOSR-86-0339. The review of this paper was arranged by Guest Editor M. Pinto.

G.-L. Tan was with the Department of Electrical and Computer Engineering, University of California at San Diego, La Jolla, CA 92093, on leave from the Department of Electrical Engineering, Beijing Polytechnic University, Beijing, China. He is now with the Department of Electrical Engineering, University of Toronto, Toronto, Ont., Canada M5S 1A4.

X.-L. Yuan is with the Department of Electrical and Computer Engineering, University of Massachusetts, Amherst, MA 01003.

Q.-M. Zhang is with the Department of Electrical Engineering, Beijing Polytechnic University, Beijing, China.

W. H. Ku and A. J. Shey are with the Department of Electrical and Computer Engineering, University of California at San Diego, La Jolla, CA 92093.

IEEE Log Number 8926894

Recently, various upwind schemes [4] have been proposed for finite difference and finite element to achieve the upwind effect in order to avoid the spurious oscillation in solving the convection dominated flow equations. In essence, the optimal upwind formulation in one-dimensional case (without source terms) can reduce to a form equivalent to the S-G scheme. Nevertheless the flow direction not always being along the grid line, it is difficult to extend these formulations to two or three dimensions in a straightforward manner [5].

A simple and feasible finite element method consistent with the exponentially fitted scheme has not been developed for two-dimensional problems. In order to further exploit the promising usefulness of the S-G scheme in the finite-element method, we have developed in our general-purpose two-dimensional Semiconductor Device Analysis program (SDA-1) a simple and accurate finite element discretization method (FEM-QSG), where the S-G scheme is embedded in the quadrature of finite element assembly of Poisson equation and continuity equations. The new method not only avoids the problem of flux direction in the discretization of flow term, but also extends the application of the S-G scheme to the discretization of source term in a consistent way.

In Section II, the basic governing equations in SDA-1 and the classical finite element discretization method are reviewed. Next, a new finite element discretization method employing the S-G scheme is presented in Section III. In Section IV, some typical simulation results are discussed and are compared with the results obtained by the classical finite element method.

II. FORMULATION OF BASIC EQUATIONS

In order to devise a general-purpose device simulator, which is capable of simulating various device structures including homojunctions and heterojunctions with arbitrary geometries under any operation condition, we based our analysis on a macroscopic description of semiconductors. In accordance with the quasi-Fermi level concept and in terms of normalized variables, the basic semiconductor equations governing device's operation with (ψ, ν, ω) ($\nu = e^{-\phi_n}$, $\omega = e^{\phi_p}$) as dependent variables are the following [6], [7]:

$$\nabla \cdot (\epsilon \nabla \psi) = (n - p - N_D^+ + N_A^-) \quad (1)$$

$$\nabla \cdot (\mu_n e^{(\psi+V_n)} \nabla \nu) = \frac{\partial n}{\partial t} + R \quad (2)$$

$$\nabla \cdot (\mu_p e^{(-\psi+V_p)} \nabla \omega) = \frac{\partial p}{\partial t} + R \quad (3)$$

where ϕ_n and ϕ_p are the quasi-Fermi potentials for electrons and holes; ν and ω are the Slotboom variables; ϵ is the permittivity of semiconductor; N_D^+ and N_A^- are the concentrations of ionized donor and acceptor; μ_n and μ_p are the mobilities of electrons and holes; R is the net recombination-generation rate including Shockley-Read-Hall recombination, Auger recombination, impact ionization. . . ; n and p are the electron and hole densities and are given by

$$n = n_{ir} e^{(\psi+V_n-\phi_n)} \quad (4)$$

$$p = n_{ir} e^{(\phi_p-\psi+V_p)} \quad (5)$$

where V_n and V_p are the band parameters, which take into account the variation of band edge with doping and composition, the shape of energy band, and the distribution statistics.

Equations (1)-(3) can be generalized and expressed in the form

$$\nabla \cdot (a \nabla u) = f \quad (6)$$

$$u = (\psi, \nu, \omega) \quad (7)$$

$$a = (\epsilon, \mu_n e^{(\psi+V_n)}, \mu_p e^{(-\psi+V_p)}) \quad (8)$$

$$f = \left(n - p - N_D^+ + N_A^-, \frac{\partial n}{\partial t} + R, \frac{\partial p}{\partial t} + R \right). \quad (9)$$

Note that (6)-(9) denote three individual equations in the same mathematical form.

If the Gummel iteration method is assumed and using the Galerkin's analysis of (6), the finite element discretization results in the formulation [8]

$$\sum_{j=1}^N (K_{ij} + G_{ij}) \Delta u_j = - \left(\sum_{j=1}^N K_{ij} u_j + f_i \right) \quad (10)$$

where the stiffness matrices and load vector are defined as

$$K_{ij} = \iint a \nabla \phi_i \cdot \nabla \phi_j ds \quad (11)$$

$$G_{ij} = \iint \frac{\partial f}{\partial u} \phi_i \phi_j ds \quad (12)$$

$$f_i = \iint f \phi_i ds \quad (13)$$

and ϕ_i is the shape function, usually chosen as a low order polynomial. Note that there is no derivative term of a involved in the K_{ij} term, however, which may appear in certain cases as stated in Appendix C. Here, the derivative of a is implicitly included in the decoupled iteration scheme, where the Poisson equation is solved first by assuming known quasi-Fermi potentials, then continuity

equations are solved with the potential given from the preceding step. And the Gummel iteration is repeated until self-consistent values of all unknowns are obtained.

For finite element analysis, the main concern is the accuracy of the quadrature in the assembly of stiffness matrices and right-hand side vector of (10), i.e., assembling (11)-(13), in which the complex calculations are involved in determining the values of the function to be integrated.

Conventionally a set of low order polynomials [2] are also used to approximate the carrier densities, n and p , ($e^{(\psi+V_n)}$), and ($e^{(-\psi+V_p)}$), which can be written as

$$n = \sum_{iee} n_i \phi_i \quad (14)$$

$$p = \sum_{iee} p_i \phi_i \quad (15)$$

$$e^{(\psi+V_n)} = \sum_{iee} (e^{(\psi+V_n)})_i \phi_i \quad (16)$$

$$e^{(-\psi+V_p)} = \sum_{iee} (e^{(-\psi+V_p)})_i \phi_i \quad (17)$$

where index i is the alternation of the vertices of the triangular element e . Let's take an example of assembling the matrix element $G_{ij}^{\psi, e}$ of Poisson equation due to element e .

$$G_{ij}^{\psi, e} = \iint_e (n + p) \phi_i \phi_j ds \quad (18)$$

where two methods can be applied for the approximation of such integral functions. On the one hand, the direct integration is an intuitional choice; on the other hand, the Gaussian quadrature rules with various orders are applicable. If the direct integration method is applied, the resultant approximation will be simply in the form

$$\begin{aligned} G_{ij}^{\psi, e} &= \iint_e \sum_{kee} (n + p)_k \phi_k \phi_i \phi_j ds \\ &= \sum_{kee} (n + p)_k \iint_e \phi_i \phi_j \phi_k ds. \end{aligned} \quad (19)$$

It is clearly seen from the above that using low order polynomials to approximate the carrier densities, n and p , ($e^{(\psi+V_n)}$), and ($e^{(-\psi+V_p)}$) will no doubt result in large integration errors because these variables inherently exhibit a highly nonlinear variation in a small region, leading to an inaccurate solution as well as a poor convergence rate, except that the mesh is intensively refined.

The Gaussian quadrature requiring a least number of evaluations to achieve a maximum accuracy is ideally suited for our use [8]. If the Gaussian quadrature rules are applied, we might need values of n , p , ($e^{(\psi+V_n)}$), and ($e^{(-\psi+V_p)}$) at certain points in addition to those at vertices of the element in order to have an accurate high order approximation, which could be interpolated from the known values at vertices. However, it is obvious that using the same low order interpolation polynomials like (14)-(17) in Gaussian quadrature will suffer from the same

low accuracy problem as that which occurs in the direct integration method. Thus an approximation of the integrand in the Gaussian quadrature based on a nonlinear functional fitting would be more desirable.

III. NEW FINITE-ELEMENT DISCRETIZATION EMPLOYING THE S-G SCHEME

In order to take advantage of the simplicity and accuracy of the S-G scheme associated with the finite difference discretization and to avoid the shortcomings of the classical finite element integration method, we employ a seven-point Gaussian quadrature rule in conjunction with the S-G scheme, while assembling the finite-element stiffness matrices and right-hand side vector. This new scheme can be outlined as follows.

For an arbitrary triangular element, e , as shown in Fig. 1, the seven-point Gaussian quadrature rule with error estimate of $O(h^4)$ [8] reads

$$I = \int_e f ds = 2\Delta \sum_{k=1}^7 w_k f(L_1, L_2)|_k \quad (20)$$

where Δ is the area of element e ; L_1 and L_2 are natural coordinates of the triangular element; the seven sampling points on an element are taken at the vertices of triangle, the middle points of the edges and the center of triangle, respectively, as illustrated in Fig. 1; and the corresponding weighting coefficient for Gaussian quadrature at the k th point, w_k , is listed in Table I.

If the quadrature rule (20) is applied to the finite element integration of (11)–(13), a general form can be described as

$$\begin{aligned} \iint_e G(n, p, e^{(\psi+V_n)}, e^{(-\psi+V_p)}) ds \\ = 2\Delta \sum_k G(n_k, p_k, (e^{(\psi+V_n)})_k, (e^{(-\psi+V_p)})_k) w_k \end{aligned} \quad (21)$$

where $n_k, p_k, (e^{(\psi+V_n)})_k, (e^{(-\psi+V_p)})_k, (k = l, m, n, p)$ can be evaluated using a S-G formula-like function. For the approximations of n_k and p_k , we follow the S-G scheme and assume the electric field and the current density between two neighboring grid point i and j are constants, which yields the interpolation formula based on current density equations (see Appendix A for details).

$$\begin{aligned} n(x)|_k = [1 - g(x_k, \Delta\psi_{ij})]n_i + g(x_k, \Delta\psi_{ij})n_j, \\ x_k \in [x_i, x_j] \end{aligned} \quad (22)$$

$$\begin{aligned} p(x)|_k = [1 - g(x_k, -\Delta\psi_{ij})]p_i + g(x_k, -\Delta\psi_{ij})p_j, \\ x_k \in [x_i, x_j] \end{aligned} \quad (23)$$

$$g(x, y) = \frac{1 - e^{-\frac{y(x-x_i)}{h_{ij}}}}{1 - e^{-y}} \quad (24)$$

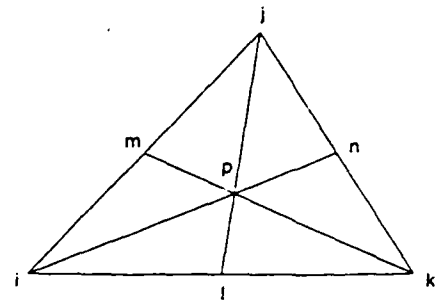


Fig. 1. A triangular element and its sampling points of Gaussian quadrature.

TABLE I
THE WEIGHTING COEFFICIENTS FOR THE SEVEN-POINT GAUSSIAN QUADRATURE

	i	j	k	l	m	n	p
$2w_k$	3/60	3/60	3/60	8/60	8/60	8/60	27/60

$$\Delta\psi_{ij} = \psi_j + V_{nj} - (\psi_i + V_{ni}) \quad (25)$$

$$h_{ij} = x_j - x_i \quad (26)$$

For the approximations of $(e^{(\psi+V_n)})$ and $(e^{(-\psi+V_p)})$, Bank [9] pointed out that the following three schemes can be applied:

- (1) linear interpolation from the nodal values $(e^{(\psi+V_n)})_i$ and $(e^{(\psi+V_n)})_j$;
- (2) linear interpolation from the nodal values $(\psi + V_n)_i$ and $(\psi + V_n)_j$;
- (3) interpolation by using Bernoulli function

and suggested that scheme (3) is more accurate than the others in the sense of nonlinear functional fitting. Based on device physics considerations, we derive an interpolation rule similar to the scheme (3), which can be expressed as

$$(e^{(\psi+V_n)})_k = B(\Delta\psi_{ij}) e^{(\psi_j+V_{nj})} \quad (27)$$

$$(e^{(-\psi+V_p)})_k = B(-\Delta\psi_{ij}) e^{(-\psi_i+V_{pi})} \quad (28)$$

with Bernoulli function defined as

$$B(x) = \frac{x}{e^x - 1} \quad (29)$$

Concerning the determination of the function value at the central point, we take an average of the three interpolated values which are obtained by applying the interpolation rule described above along the respective line connecting a vertex and the middle point of the corresponding edge opposite to it, i.e., $i-n, j-l$, and $k-m$ in Fig. 1. In an appropriately refined mesh which when used in the new scheme is always more coarse than that for the classic finite element method, the differences among these three interpolated values are negligible since we have a more accurate functional fitting expression chosen for interpolation.

For clarity, let's formulate the quadratures for Poisson equation and electron continuity equation in the following (decoupled iteration method assumed):

(1) *Poisson equation*: The calculation of $K_{ij}^{\psi, \epsilon}$ is simple, since $a = \epsilon$ is constant. Here only formulations for $G_{ij}^{\psi, \epsilon}$ and $f_i^{\psi, \epsilon}$ are given, which read

$$\begin{aligned} G_{ij}^{\psi, \epsilon} &= \iint_{\epsilon} (n + p) \phi_i \phi_j ds \\ &= 2\Delta \sum_{k=1}^7 (n_k + p_k) (\phi_i)_k (\phi_j)_k w_k \quad (30) \end{aligned}$$

$$\begin{aligned} f_i^{\psi, \epsilon} &= \iint_{\epsilon} (n - p - N_s) \phi_i ds \\ &= 2\Delta \sum_{k=1}^7 (n_k - p_k - N_{sk}) (\phi_i)_k w_k \quad (31) \end{aligned}$$

where n_k, p_k ($k = l, m, n, p$) can be evaluated from (22) and (23), respectively, and $(\phi_i)_k = \phi_i(x_k, y_k)$, $(\phi_j)_k = \phi_j(x_k, y_k)$.

(2) *Continuity equation*:

$$\begin{aligned} K_{ij}^{n, \epsilon} &= \iint_{\epsilon} \mu_n e^{(\psi + V_n)} \nabla \phi_i \nabla \phi_j ds \\ &= 2\Delta \sum_{k=1}^7 \mu_k (e^{\psi + V_n})_k (\nabla \phi_i)_k (\nabla \phi_j)_k w_k \quad (32) \end{aligned}$$

where $\nabla \phi_i$ and $\nabla \phi_j$ are constant vectors, if linear shape functions are chosen for triangular element.

For simplicity, let us assume the S-R-H recombination dominates the recombination mechanism

$$f = R = \frac{np - n_i^2}{\tau_n(p + n_i) + \tau_p(n + n_i)} \quad (33)$$

$$\begin{aligned} \frac{\partial f}{\partial v} &= \frac{(p + n_i)(\tau_n p + \tau_p n_i)}{[\tau_n(p + n_i) + \tau_p(n + n_i)]^2} n_{ir} e^{(\psi + V_n)} \\ &= \bar{R}(n, p) n_{ir} e^{(\psi + V_n)} \quad (34) \end{aligned}$$

then the matrix elements are given by

$$\begin{aligned} G_{ij}^{n, \epsilon} &= \iint_{\epsilon} \bar{R}(n, p) n_{ir} (e^{\psi + V_n}) \phi_i \phi_j ds \\ &= 2\Delta \sum_{k=1}^7 \bar{R}(n_k, p_k) n_{ir} (e^{\psi + V_n})_k (\phi_i)_k (\phi_j)_k w_k \quad (35) \end{aligned}$$

$$f_i^{n, \epsilon} = \iint_{\epsilon} R \phi_i ds = 2\Delta \sum_{k=1}^7 R(n_k, p_k) (\phi_i)_k w_k \quad (36)$$

where for $k = (l, m, n, p)$, n_k, p_k , and $(e^{\psi + V_n})_k$ are calculated by (22)-(29).

In the sense of finite element analysis, the FEM-QSG formulation conforms to the Galerkin method, where the

shape functions serve as the weighting functions. In situations where the dominant drift term is strong enough to cause spurious oscillations, we can easily modify the weighting functions in the FEM-QSG formulation to achieve upwind effect without any inconsistency [4]. (See Appendix C for a detailed discussion.)

In order to take advantage of the simplicity in derivation and its consistency with the finite element theory, the definition of current proposed by Barnes *et al.* [2] is adopted in our current calculation, by which the local as well as global current conservations are preserved. It must be stressed that in the FEM-QSG formulation the modification on the interpolation of $n, p, e^{\psi + V_n}, e^{-\psi + V_p}$ for the quadratures would not perturb the current conservation property and the consistency with the finite element theory.

This new discretization scheme not only uses an accurate seven-point Gaussian quadrature rule instead of the classical integration method but also applies the S-G scheme to calculating the values of quadrature points which are not on the vertices of an element so that the approximation of carrier densities, $(e^{\psi + V_n})$ and $(e^{-\psi + V_p})$ yields an accurate exponential functional fitting form. As a result, the convergence rate would be significantly enhanced and the accuracy of solution would be obviously improved due to the low finite element discretization error generated by the new method.

IV. SIMULATION RESULTS AND DISCUSSIONS

In the BIM discretization, an equivalent central finite difference discretization scheme is usually applied to the equation assembly of Poisson equation in a two-dimensional domain, which results in a solution with comparable accuracy to that generated by the classical finite element method using piecewise linear finite elements [10]. Additionally, the linear interpolation on the source terms (the right-hand side terms) of Poisson equation by the BIM will inevitably introduce a larger discretization error than that by the S-G interpolation in our method, especially for the strong coupling cases. On the solution of current continuity equations, a hybrid finite-difference finite-element technique in conjunction with the S-G scheme is applied in the BIM scheme. From the viewpoint of the generalized finite-element method [11], it is found that there is a natural correspondence between the BIM scheme and our new method on the discretization of continuity equations. A more detailed comparison is presented in Appendix B.

To demonstrate the effectiveness and accuracy of this new discretization method (method II) compared to the classical one (method I), we give three examples. From the theoretical analysis, we gather that the convergence rate is strongly dependent on the accuracy of discretization. We thus consider that a detailed comparison with the classical finite element can show us to what extent that the discretization errors have influence on the convergence rate.

First of all, a simple abrupt p-n junction is simulated. Two meshes used for simulations are illustrated in Fig. 2.

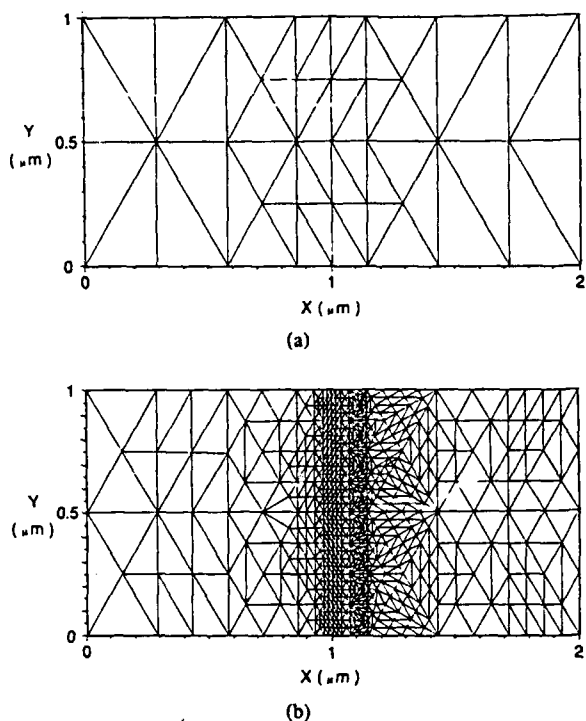


Fig. 2. Meshes used for simulations of an abrupt p-n junction with grid-points of (a) $NP = 37$, (b) $NP = 640$.

The coarse mesh is used as a reference for the following evaluations. The mesh with fine grid is a typical mesh example for obtaining the optimal solution.¹

Fig. 3 shows the number of iterations required by method II to reach convergence and that required by method I, as a function of impurity concentration. Fig. 4 compares the minimum number of mesh points required for convergence by method II with that by method I, also as a function of impurity concentration. As seen in Figs. 3 and 4 the results indicate that the integrations by method II are so accurate that the convergence speed is almost independent of the impurity density and the grid size of the mesh. On the contrary, the convergence rate of the simulation discretized by method I is very sensitive to the impurity density and the fineness and the layout of the mesh due to large integration errors involved in the approximation of nonlinear functions during assembling the element matrices, especially for highly doped regions.

Fig. 5 shows the decreasing rate of the error function of Poisson equation (at zero bias). It is obvious that the convergence rate is quadratic for method II. Besides, it does not need damping scheme in Newton iteration except the first few iterations, whereas the convergence rate is almost a linear one for method I.

In Fig. 6, we compare the discretization error, ERR ,² of Poisson equation by method II with that by method I,

¹Here the optimal solution is obtained by keeping reducing the grid size by half each time (i.e., refining the mesh) until the relative deviation between solutions of two successive discretizations is less than 1 percent.

²The discretization error ERR is defined as the relative error between the exact solution and numerical solution.

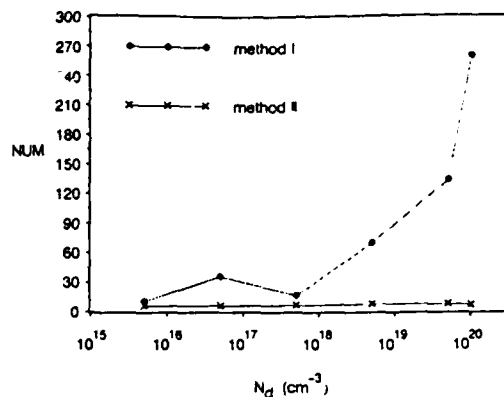


Fig. 3. The number of iteration NUM required for convergence versus impurity concentration N_D ($N_A = 1 \times 10^{15} \text{ cm}^{-3}$, zero bias).

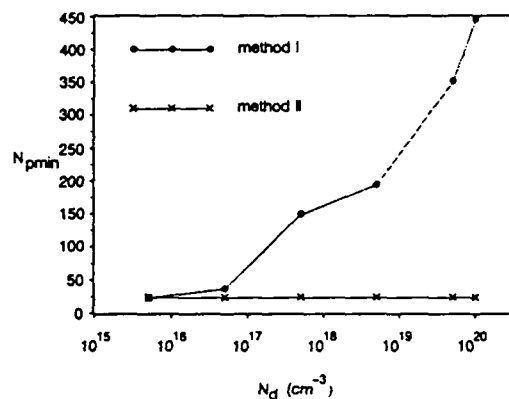


Fig. 4. The minimum number of mesh points N_{pmin} required for convergence versus impurity concentration N_D ($N_A = 1 \times 10^{15} \text{ cm}^{-3}$, zero bias).

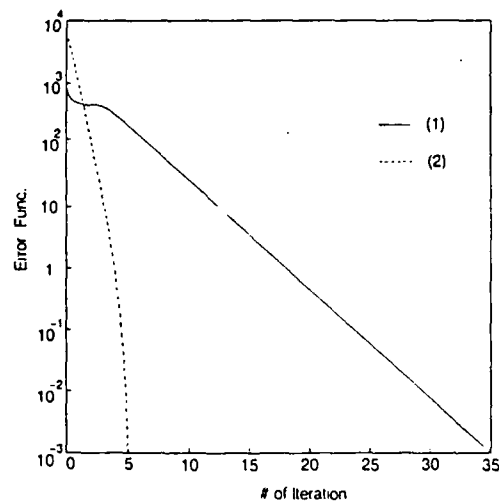


Fig. 5. The decrease of the error function of Poisson's equation versus the number of iterations ($NP = 37$, zero bias) by (1) method I and (2) method II.

as a function of minimum mesh size. And we show in Fig. 7 the discretization errors of continuity equations of electrons and holes by method II with that by method I, again as a function of minimum mesh size.

Figs. 6 and 7 confirm that by method II we can obtain a more accurate solution than that by method I on the same

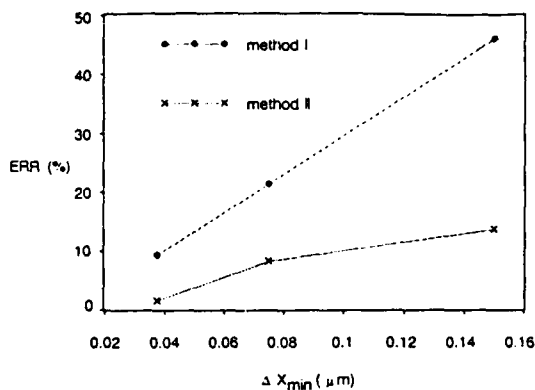


Fig. 6. The discretization errors ERR between exact solution and numerical solution of Poisson's equation as a function of minimum mesh size Δx_{\min} ($N_A = 1 \times 10^{15} \text{ cm}^{-3}$, $N_D = 1 \times 10^{15} \text{ cm}^{-3}$, zero bias).

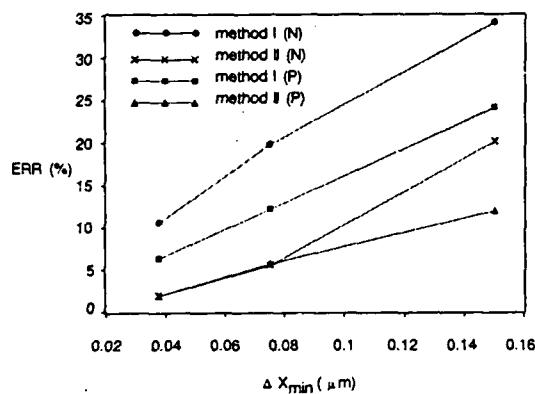


Fig. 7. The discretization errors of continuity equations of electron and hole between exact solution and numerical solution as a function of Δx_{\min} ($N_A = 1 \times 10^{15} \text{ cm}^{-3}$, $N_D = 5 \times 10^{15} \text{ cm}^{-3}$, $V_{app} = 0.6 \text{ V}$).

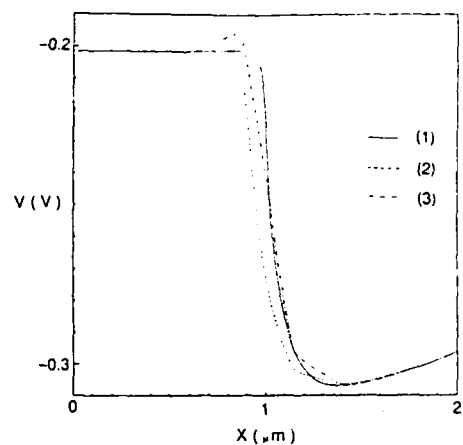
grid, in particular for the Poisson equation case. In addition, the results illustrate that applying method II to continuity equations will allow us to take the same advantages of the S-G scheme as those well known in the finite difference counterpart. Therefore, this new finite element scheme is competitive with the finite difference method with exponential functional fitting in the sense of discretization accuracy.

Fig. 8 shows the simulation potential distribution and electron and hole concentration plots of the abrupt p-n junction of the optimal solution¹ compared with those obtained by methods I and II using the mesh shown in Fig. 2(a). We can see that the solution calculated by method II is closer to the optimal solution than that by method I on the basis of same simulation mesh.

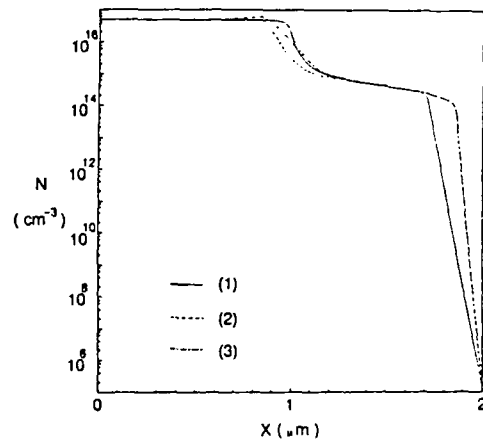
In order to test the effectiveness and efficiency of the new method for complex device cases, we further simulated a typical bipolar transistor and a MOS transistor.

The simulated bipolar transistor, whose geometric structure is shown in Fig. 9(a), is doped with an impurity concentration profile as plotted in Fig. 9(b). Tables II and III list the relative deviation, RD³ of the calculated results

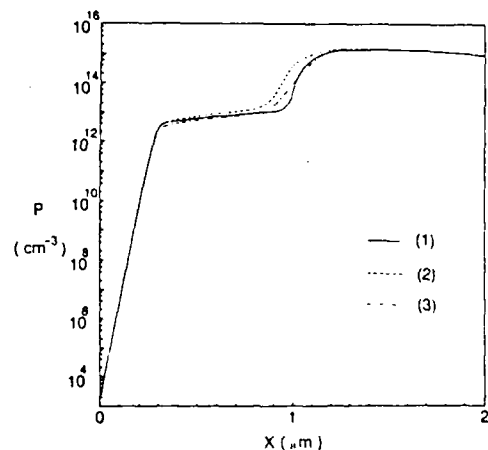
³The relative deviation, RD, is defined as the maximum relative deviation of the calculated results from the optimal solution.



(a)



(b)



(c)

Fig. 8. Plots of (a) the potential distribution, (b) the electron concentration, and (c) the hole concentration of along the central line of the abrupt p-n junction of (1) the optimal solution, solutions obtained. (2) by method I, and (3) by method II.

vith respect to the optimal solution for the bipolar transistor biased at $V_c = 1.6 \text{ V}$ and $V_g = 0.9 \text{ V}$ with various meshes by methods I and II. The results manifest that by using method II the solution has higher accuracy than that by method I. In other words, under the same accuracy requirement, method II can use a coarser mesh than that used by method I to reach the same goal.

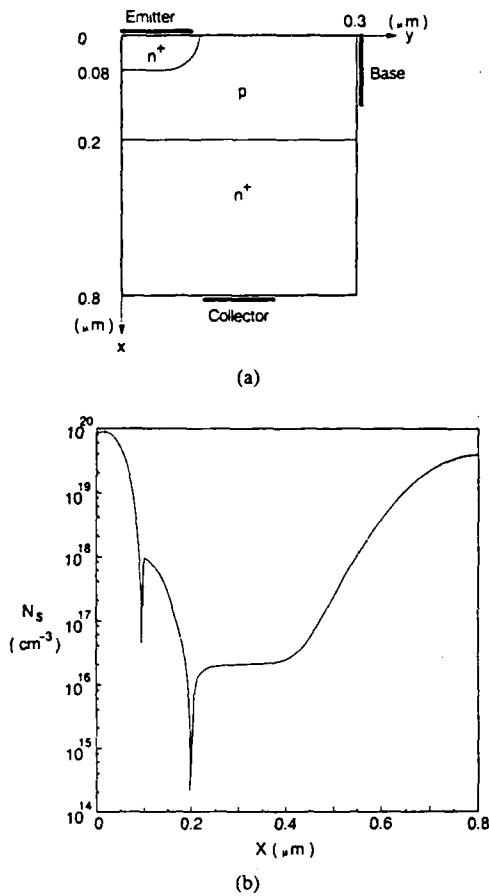


Fig. 9. (a) The device structure and (b) the doping profile along the line of $y = 0$ of the simulated bipolar transistor.

TABLE II
THE RELATIVE DEVIATION OF THE CALCULATED RESULTS FROM THE OPTIMAL SOLUTION FOR THE BIPOLAR TRANSISTOR (AT $V_c = 1.6$ V, $V_b = 0.9$ V) USING VARIOUS MESHES (METHOD I)

NP	554	904
RD(%)v	2.775	2.774
RD(%)n	8.722	8.720
RD(%)p	5.512	5.731

TABLE III
THE RELATIVE DEVIATION OF THE CALCULATED RESULTS FROM THE OPTIMAL SOLUTION FOR THE BIPOLAR TRANSISTOR (AT $V_c = 1.6$ V, $V_b = 0.9$ V) USING VARIOUS MESHES (METHOD II)

NP	162	593	611	851
RD(%)v	3.570	2.753	2.753	2.142
RD(%)n	21.07	8.252	8.252	6.471
RD(%)p	12.99	5.738	3.771	3.771

Secondly, a MOS transistor, whose structure is shown in Fig. 10, is simulated as well. Fig. 11 shows the convergence rate of Poisson equation for MOS. We found out that method II also held a quadratic convergence rate. We

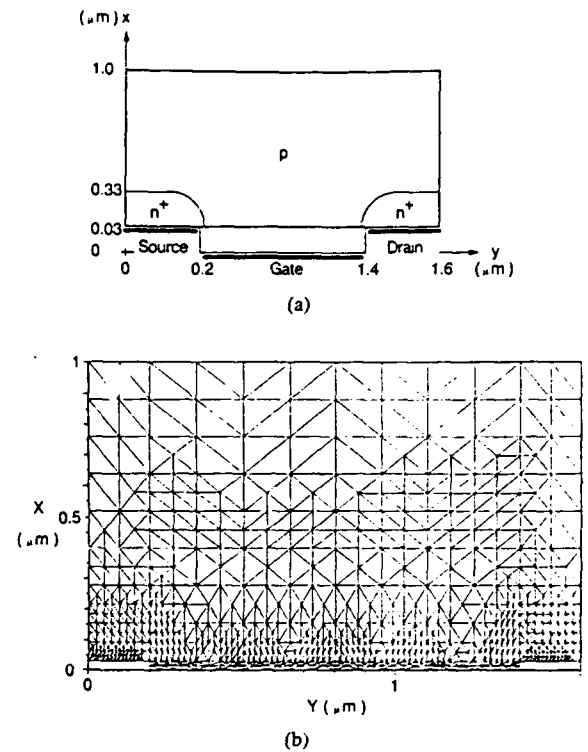


Fig. 10. (a) The device structure of the simulated MOS transistor and (b) the mesh used for simulation.

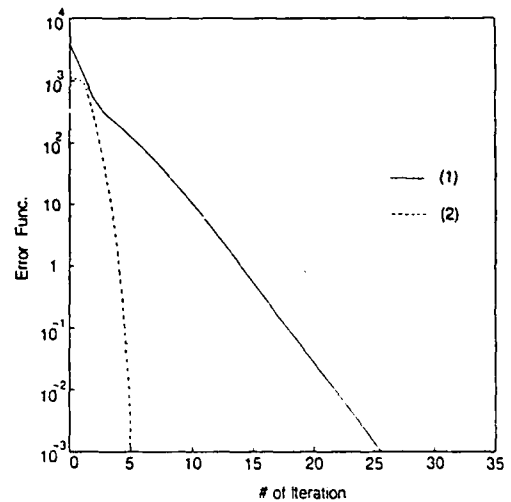


Fig. 11. The decrease of the error function of Poisson's equation versus the number of iterations of Poisson's equation for the MOS (zero bias) by (1) method I and (2) method II.

tabulate the RD of the MOS example by methods I and II in Tables IV and V, respectively, and the results also reveal that the accuracy of solution by method II is higher than that by method I. Fig. 12 shows perspective plots of electron and hole distribution for the BJT (at $V_c = 1.6$ V, $V_b = 0.9$ V).

We can easily find out from the examples demonstrated above that the advantages of the new discretization method applied equally well to a simple abrupt p-n junction and the complicated device structures.

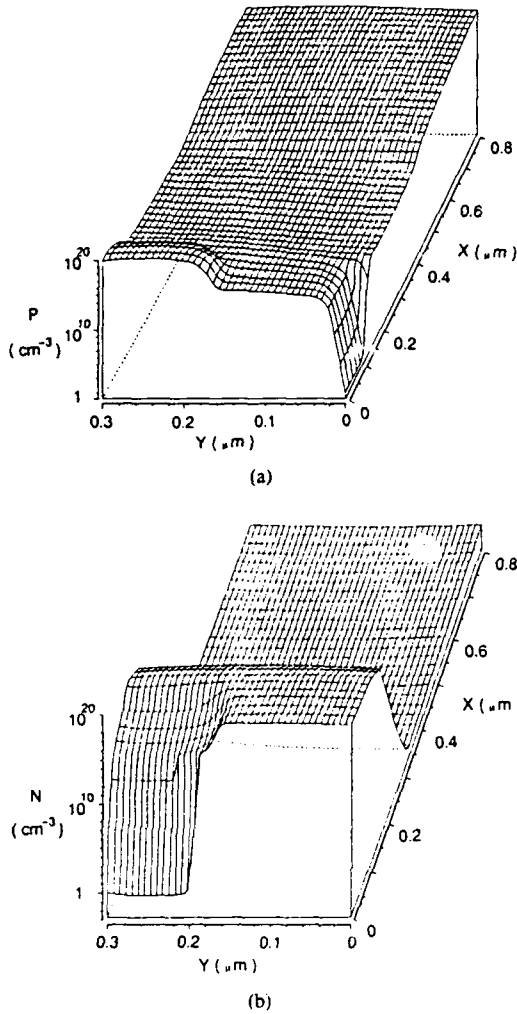


Fig. 12. The perspective plots of electron and hole distributions of the simulated BJT ($V_c = 1.6$ V, $V_o = 0.9$ V).

TABLE IV

THE RELATIVE DEVIATIONS OF THE SOLUTIONS FOR n-MOS (AT $V_g = 1.0$ V, $V_d = 0.5$ V) ESTIMATED ALONG THE LINES OF $x = 0.04$ AND $0.06 \mu\text{m}$ (METHOD II)

NP		220	375
RD (%)	$x=0.04$	1.28	1.08
v	$x=0.06$	2.46	1.60
RD (%)	$x=0.04$	3.84	4.73
n	$x=0.06$	3.86	4.70

TABLE V

THE RELATIVE DEVIATIONS OF THE SOLUTIONS FOR n-MOS (AT $V_g = 1.0$ V, $V_d = 0.5$ V) ESTIMATED ALONG THE LINES OF $x = 0.04$ AND $0.06 \mu\text{m}$ (METHOD I)

NP		240	295	492
RD (%)	$x=0.04$	4.03	5.04	3.71
v	$x=0.06$	4.68	4.22	4.02
RD (%)	$x=0.04$	8.61	8.33	5.96
n	$x=0.06$	7.80	7.66	5.19

The weakness of the new method stems from the constant derivative assumption of ψ, ϕ_n, \dots imposed on the S-G scheme. The approximation is poor by the S-G scheme at the transition layer where a large variation of electrical field or current density occurs. The remedy to this is refining the mesh properly by self-adaptive algorithm.

V. CONCLUSIONS

A simple and accurate finite element discretization method has been developed in the two-dimensional semiconductor device analysis program SDA-1. The key of this method lies in (1) accurate interpolation rules, which are derived based on simple device physics considerations, are applied to the functional approximations of $n, p, e^{(\psi+V_n)}, \dots$, necessary in the finite element assembly of stiffness matrices as well as source terms of Poisson equation and continuity equations in a consistent way rather than just concentrating on the discretization of flow term, $\nabla \cdot (a\nabla u)$, of continuity equation like the BIM-SG scheme does. (2) The inherent simplicity and flexibility in the finite element formulation make the new method applicable to multidimensional problems. (3) The simplicity of embedding the S-G scheme in the quadrature of finite element assembly lends itself to all kinds of finite element methods employing various elements, shape functions and weightings. The resultant exponential functional fitting by the new method avoids high discretization errors usually incurred by the classical finite element discretization method. Using this new method, we not only obtain solution with high accuracy but also speed up the convergence rate significantly. Moreover, as the theoretical prediction, the numerical experiments confirm that the convergence rate strongly relies on a proper functional fitting and an accurate numerical integration in the application of the finite element method to the semiconductor equations.

APPENDIX A

THE APPLICATION OF THE S-G SCHEME TO FINITE ELEMENT METHOD BASED ON DEVICE PHYSICS CONSIDERATIONS

Considering the current density equation for electrons, in terms of different dependent variables, they can be expressed, respectively, as

$$J_n = -\mu_n(n\nabla\psi - \nabla n) \tag{A1}$$

or

$$J_n = \mu_n e^{\psi} \nabla v. \tag{A2}$$

According to the Schafetter-Gummel (S-G) scheme, if the derivatives of ψ, v, \dots , between point i and j are assumed constant, the S-G approximation of the current density equation projected on $i - j$ line by central differences reads

$$J_n = \bar{v} e^{\psi} B(\Delta\psi_{ji}) \frac{v_{nj} - v_{ni}}{h} \tag{A3}$$

where $B(x) = x/(e^x - 1)$ is the Bernoulli function; $\bar{\mu}$ is the average value of μ between point i and j [9]. It seems difficult to derive a similar expression like (A3) by the finite element discretization. However, the similarity between (A3) and (A2) suggests that $e^{\psi_i} B(\Delta\psi_{ji})$ is a proper interpolation formula for evaluating e^{ψ} at certain point between points i and j ; or in a more exact term, the e^{ψ} value at midpoint M between points i and j can be approximated by

$$(e^{\psi})_M = e^{\psi_i} B(\Delta\psi_{ji}). \quad (\text{A4})$$

The carrier densities, n and p , are well known for having an exponential functional dependence on ψ . The linear interpolation will obviously result in an inaccurate estimation. However, we can further extend the idea behind the S-G scheme to the evaluation of carrier concentration, at point k located in between two neighboring gridpoints i and j , in terms of the given carrier concentrations n_i and n_j at these two terminal point as follows.

Based on the constant derivative assumption, the current density equation (A1) in a one-dimensional case reduces to a two-point boundary value problem:

$$\frac{dn}{dx} + E_{\text{eff}} n = \frac{J_n}{\mu_n} \quad (\text{A5})$$

with the boundary conditions

$$n(x_i) = n_i \quad (\text{A6})$$

$$n(x_j) = n_j \quad (\text{A7})$$

where $E_{\text{eff}} = -\nabla\psi$.

The general solution n can be expressed as

$$n = n_i(1 - g) + n_j g \quad (\text{A8})$$

$$g = \frac{1 - e^{-\frac{y(x-x_i)}{h_{ij}}}}{1 - e^{-y}} \quad (\text{A9})$$

where $h_{ij} = x_j - x_i$, $y = [\psi_j - \psi_i]$. Then the equivalent S-G formula, (22), can be obtained and (23) can be derived in the same way.

APPENDIX B

THE COMPARISON OF THE NEW METHOD WITH THE BIM-SG SCHEME

A triangular (or rectangular) domain partition process is usually employed in the BIM scheme first. Then boxes are constructed around every gridpoint by taking the mid-perpendiculars of line segments directed to its neighboring points. If the Green's theorem is applied to (6) on a box, we have

$$\int a \nabla u \cdot dl = \int f ds \quad (\text{B1})$$

or

$$\sum_i a \nabla u \cdot \hat{n}_i l_i = fS \quad (\text{B2})$$

where \hat{n}_i is the unit normal vector of box edge l_i ; l_i is the length of the edge; S is area of the box.

If the BIM scheme is applied to Poisson equation on the example mesh shown in Fig. 13, a standard central difference expression would be obtained:

$$a(u_1 + u_2 + u_3 + u_4 - 4u_0) = f_0 h^2. \quad (\text{B3})$$

This shows an equivalence of the BIM scheme on Poisson equation to the standard central difference with accuracy of second order. From other point of view, the application of classical FEM to Poisson equation on the same mesh will yield a same central difference expression. Thus the BIM scheme is equivalent to the classical FEM on the discretization of Poisson equation. Although we use a rectangular mesh here, the derivation holds generally true on other mesh geometries [10].

In Section III, we have shown the superiority of the new method to the classical FEM due to the accurate assembly of the stiffness matrices. Besides, we introduce the S-G scheme to the Jacobian and right-hand side vector via $\iint (n+p)\phi_i\phi_j ds$ and $\iint (n-p-N_s)\phi_i ds$. Compared to the BIM scheme where the source term is approximated simply by f_0 times the box area, the more accurate treatment of the right-hand side vector in the new method will definitely further reduce the discretization error. Thus the new method does not need mesh as fine as that usually used by the BIM scheme to achieve a same convergence rate in solving Poisson equation.

As for continuity equation, the BIM scheme incorporates the S-G current formula to improve the discretization accuracy. For convenience, in the following comparison we consider the contribution to the Jacobian only from the triangle $\Delta 015$ as indicated in Fig. 13 by the BIM-SG scheme, which gives

$$\begin{aligned} J_1 \cdot l_1 + J_2 \cdot l_2 &= \mu_{01} e^{\psi_0} B(\Delta\psi_{01}) \frac{v_1 - v_0}{h} l_1 \\ &+ \mu_{05} e^{\psi_0} B(\Delta\psi_{05}) \frac{v_5 - v_0}{\sqrt{2}h} l_2 \\ &= \mu_{01} e^{\psi_0} B(\Delta\psi_{01}) \frac{v_1 - v_0}{2} \end{aligned} \quad (\text{B4})$$

where for the mesh in Fig. 13, $l_1 = h/2$ and $l_2 = 0$. (For other cases, l_1, l_2 may not be zero; however, the comparison still holds valid.)

If the new method is applied, according to (32), the discretization of continuity equation on element $\Delta 015$ reads

$$\sum_{j=0,1,5} K_{ij}^n e^{\psi_j} v_j = 2\Delta\bar{\mu} \sum_k w_k (e^{\psi})_k \cdot \sum_j (\nabla\phi_i)_k (\nabla\phi_j)_k v_j \quad (\text{B5})$$

Assume the shape function is linear, then

$$\nabla\phi_i \cdot \nabla\phi_j = \frac{b_i b_j + c_i c_j}{4\Delta^2} \quad (\text{B6})$$

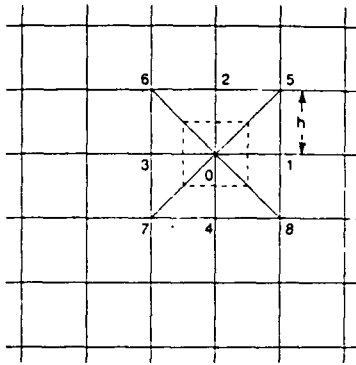


Fig. 13. An example rectangular mesh.

where Δ is area of element $\Delta 015$, and (B5) becomes

$$\sum_{j=0,1,5} K_{ij}^n e^{\psi_j} = \bar{\mu} \left(\sum_k 2w_k (e^{\psi})_k \right) \sum_j \left(\frac{b_i b_j + c_i c_j}{4\Delta} \right) \quad (\text{B7})$$

where $\bar{\mu}$ is average value of μ . Moreover, from the linear shape function, we can easily prove that

$$\sum_j \frac{b_i b_j + c_i c_j}{4\Delta} = \frac{v_0 - v_1}{2} \quad (\text{B8})$$

Therefore, (B7) can be further expressed in the form

$$\sum_{j=0,1,5} K_{ij}^n e^{\psi_j} = \bar{\mu} \left(\sum_k 2w_k (e^{\psi})_k \right) \frac{v_0 - v_1}{2} \quad (\text{B9})$$

where

$$\begin{aligned} \sum_k 2w_k (e^{\psi})_k &= \sum_{k=0,1,5} \frac{3}{60} (e^{\psi})_k + \frac{8}{60} (e^{\psi})_0 B(\Delta\psi_{01}) \\ &+ \frac{8}{60} (e^{\psi})_3 B(\Delta\psi_{05}) + \frac{8}{60} (e^{\psi})_1 \\ &\cdot B(\Delta\psi_{15}) + \frac{27}{60} (e^{\psi})_p \end{aligned} \quad (\text{B10})$$

Equation (B10) is equivalent to a weighting scheme over (e^{ψ}) with weights on

- (1) three vertex values (e^{ψ}) by $3/60$;
- (2) midpoint values of three edges (corresponding to $(e^{\psi})_0 B(\Delta\psi_{01})$ in the S-G scheme) by $8/60$;
- (3) the value at the central point $(e^{\psi})_p$, which is also an average of the midpoint values and the vertex values, by $27/60$.

Comparing (B9) with (B4), we will find that the idea behind the S-G scheme is embedded in the new method in a different form where the weighting average of (e^{ψ}) is taken on the element rather than on the edges by the BIM-SG scheme. Thus, the new method is at least as good as the BIM-SG scheme in the sense of applying the S-G scheme to continuity equation. It might have a lower discretization error than the BIM-SG scheme does, if we count the factors of using the accurate seven-point Gauss-

ian quadrature rule and weighting the average of a on element instead of on edges.

Again, the new method has a more accurate treatment on the source term f than the BIM-SG scheme does by further introducing the S-G formula to the terms, $\iint (\partial f / \partial u) \phi_i \phi_j ds$ and $\iint f \phi_i ds$, where the BIM-SG scheme simply approximate these terms by linear interpolations. In this respect, if decoupled solution method is used and the generation-recombination terms are neglected where the continuity equation is linear, the new method is identical to the BIM-SG scheme. However, if the generation-recombination terms are taken into account, then the equation being a nonlinear one, the new method certainly would have a better performance than the BIM scheme due to a lower discretization error from source term.

APPENDIX C

RELEVANT CHARACTERISTICS TO THE UPWIND EFFECT

If a in (6) is a function of u , (10) will involve a first-order derivative term (the drift term), via

$$\nabla \cdot [a(u) \nabla u] = a(u) \nabla^2 u + \nabla a(u) \cdot \nabla u = f \quad (\text{C1})$$

The drift term has to be taken into consideration at the following situations.

- (1) A coupled solution method is used.
- (2) A decoupled iteration method is used, while the mobility, μ , is a function of the Fermi-potential or carrier density.

As is well known, the solutions to the convective transport equation like (C1) by the standard finite difference method or the classical finite element method are often spoiled by spurious oscillations. To preclude such oscillation various schemes have been proposed over the years for finite difference discretization method and finite element discretization method. In the finite element regime, artificial diffusion, quadrature, and the Petrov-Galerkin method are common techniques utilized to achieve the upwind effect.

The application of the S-G scheme has been shown to be equivalent to adding certain "upwind term" to the standard discretization [5]. In the new method, the S-G scheme is incorporated in the quadrature and an accurate quadrature rule is employed. These techniques will come up to enhance the upwind effects in the solution.

Recently, a streamline upwind/Petrov-Galerkin method [4] has been shown effective for two-dimensional convection dominated flow problems by choosing weighting function to be the sum of the standard shape function and a streamline upwind perturbation. Since the new finite element formulation FEM-QSG conforms to the standard Galerkin method, it can be easily converted to the Petrov-Galerkin formulation by simply modifying the weighting function w_i based on the shape function ϕ_i , without causing any inconsistency. Therefore, the new finite element discretization scheme is able to enhance the upwind effects by all kinds of techniques.

REFERENCES

- [1] D. L. Scharfetter and H. K. Gummel, "Large-signal analysis of a silicon Read diode oscillator," *IEEE Trans. Electron Devices*, vol. ED-16, pp. 64-77, 1969.
- [2] John J. Barnes and Ronald J. Lomax, "Finite-element methods in semiconductor device simulation," *IEEE Trans. Electron Devices*, vol. ED-24, pp. 1082-1089, 1977.
- [3] Walter L. Ergl, Heinz K. Dirks, and Bernd Meinerzhagen, "Device modeling," *Proc. IEEE*, vol. 71, pp. 10-33, 1983.
- [4] Alexander N. Brooks and Thomas J. R. Hughes, "Streamline upwind/Petrov-Galerkin formulations for convection dominated flows with particular emphasis on the incompressible Navier-Stokes equation," *Comp. Meth. Appl. Mech. Eng.*, vol. 32, pp. 199-259, 1982.
- [5] S. J. Polak, C. Den Heijer, and W. H. A. Schilders, "Semiconductor device modeling from the numerical point of view," *Int. J. Numer. Methods Eng.*, vol. 24, pp. 763-838, 1987.
- [6] Kiyoyuki Yokoyama, Masaaki Tamizawa, and Akira Yoshii, "Accurate modeling of AlGaAs/GaAs heterojunction bipolar transistor by two-dimensional computer simulation," *IEEE Trans. Electron Devices*, vol. ED-31, pp. 1222-1229, 1984.
- [7] Mark S. Lundstrom and Robert J. Schuelke, "Numerical analysis of heterostructure semiconductor devices," *IEEE Trans. Electron Devices*, vol. ED-30, pp. 1151-1158, 1983.
- [8] O. C. Zienkiewicz, *The Finite Element Method*. New York: McGraw-Hill, 1977.
- [9] R. E. Bank, D. J. Rose, and W. Fichtner, "Numerical methods for semiconductor device simulation," *IEEE Trans. Electron Devices*, vol. ED-30, pp. 1031-1041, 1983.
- [10] Randolph E. Bank and Donald J. Rose, "Some error estimates for the box method," *SIAM J. Numer. Anal.*, vol. 24, no. 4, 1987.
- [11] I. Babuska and J. E. Osborn, "Generalized finite element methods: Their performance and their relation to mixed methods," *SIAM J. Numer. Anal.*, vol. 20, no. 3, pp. 510-536, 1983.

*



Gen-Lin Tan graduated from the Department of Engineering Physics, Qinghua University, China, in 1961.

Since then he has been engaged in teaching and research in the Department of Electrical Engineering, Beijing Polytechnic University, Beijing, China, where he is now a Professor. His research concerns microcomputer application, circuit analysis and optimization, and semiconductor device simulation. He is the author or co-author of several technical papers and three books. He has been

on leave from the University of California, San Diego, as a visiting scholar since 1987. His current research interests include simulation of III-V compound semiconductor device and integrated circuit and layout optimization of IC design.

*

Xiao-Li Yuan received the B.S. degree from Tianjin University, China, in 1984 and the M.S. degree in electrical engineering from Beijing Polytechnic University, China, in 1987. She is currently working toward the Ph.D. degree in the Department of Electrical and Computer Engineering, University of Massachusetts, Amherst.

Her research interest is in two-dimensional numerical simulation of semiconductor devices.



Qi-Ming Zhang received the B.S. degree from Xian Jiaotong University, China, in 1982 and the M.S. degree in electrical engineering from Beijing Polytechnic University, Beijing, China, in 1987.

Currently, he is an Assistant Professor in the Department of Electrical Engineering, Beijing Polytechnic University. His interests lie in the area of numerical simulations of semiconductor devices and processes.

*



Walter H. Ku received the B.S. degree (hon.) from the University of Pennsylvania, Philadelphia, in 1957, and the M.S. and Ph.D. degrees from the Polytechnic Institute of Brooklyn, NY, in 1958 and 1962, respectively, all in electrical engineering. From 1957 to 1960, he held a Research Fellowship at the Polytechnic Institute of Brooklyn.

From 1962 to 1969, he was with the Applied Research Laboratory (ARL) of the GT&E, Waltham, MA.

He joined Cornell University, Ithaca, NY, in 1969, as Professor of Electrical Engineering. During 1973-1974, he was on leave as a Visiting Associate Professor to the Department of Electrical Engineering and Computer Sciences of the University of California, Berkeley. In 1977 he was on sabbatical leave and was the first occupant of the Naval Electronic Systems Command (NAVELEX) Research Chair Professorship at the Naval Postgraduate School, Monterey, California. He has served over the years as a Consultant to DOD on the VHSIC and various monolithic programs and industrial laboratories.

During 1983-1984 he was a Distinguished Visiting Professor in the Department of Electrical Engineering and Computer Sciences of the University of California at San Diego, La Jolla, CA. Since September 1985, he has been Professor of Electrical and Computer Engineering at UCSD, and is currently directing a research group in Electronic Systems and VLSI. His current research interests are in the areas of design and fabrication of submicron gate-length MOS and GaAs FET's, HEMT's and heterojunction bipolar transistors, integrated circuit design and digital signal processing (DSP) algorithms, chip architectures and gigabit logic. He was an Associate Editor of the IEEE TRANSACTIONS ON CIRCUITS AND SYSTEMS, the Co-Chairman of the Technical Committee on Optical, Microwave and Acoustical Circuits of the IEEE Circuits and Systems Society, and a Co-Chairman of the Technical Committee on Computer-Aided Design of the IEEE Microwave Theory and Techniques Society. He is presently an Associate Editor of the *Journal of the Franklin Institute* and member of the Editorial Board of the IEEE TRANSACTIONS ON MICROWAVE THEORY AND TECHNIQUES. He is a member of the IEEE Defense R&D Committee.

Dr. Ku is a member of Eta Kappa Nu, Tau Beta Pi, Sigma Tau, Phi Tau Phi, and Sigma Xi.

*



An-Jui Shey received the B.S. and M.S. degrees in electronics engineering from National Chiao Tung University, Hsinchu, Taiwan, in 1979 and 1981, respectively. At present he is working toward the Ph.D. degree at the University of California, San Diego.

In the summer of 1984, he held a position at TRW, working in the area of VLSI digital design. Currently, he is engaged in the development of CAD tools for GaAs device and integrated circuit design.

Appendix E

**ADIC-2.C: A General-Purpose Optimization Program
Suitable for Integrated Circuit Design Applications
Using the Pseudo Objective Function Substitution Method**

ADIC-2.C: A General-Purpose Optimization Program Suitable for Integrated Circuit Design Applications Using the Pseudo Objective Function Substitution Method (POSM)

GEN-LIN TAN, SHAO-WEI PAN, WALTER H. KU, AND AN-JUI SHEY

Abstract—In this paper, a new unconstrained optimization algorithm—POSM—is presented. This algorithm, requiring neither derivative calculation nor linear search step, substitutes the objective function by a second-order approximated formulation, which enhances the convergence rate substantially and has been implemented in the general-purpose Analysis and Design program for Integrated Circuit, ADIC-2.C. Its high efficiency has been demonstrated by numerical examples as well as integrated circuit designs.

I. INTRODUCTION

THE COMMON features found in the optimization problems of circuit and system designs are a limited number of parameters to be optimized and a huge computation load that is incurred due to an excessively complicated objective function evaluation need (especially for the optimization of transient characteristics). For the existing optimization algorithm, calculation of the derivatives of the objective function or its equivalences is usually a necessity. Because of an increasing complexity of the circuit and the high nonlinearity of active elements involved, this is a complicated process concerning modern integrated circuit designs. Thus the reduction in the number of function evaluations is crucial to its efficiency. Furthermore, the linear search is an essential step to ensure the convergence of Newton's iteration. The techniques employed during the linear search step in existing optimization schemes are very time consuming. Therefore, it is our intention to develop a new algorithm with

the following characteristics:

- (1) no need for derivative calculation,
- (2) reducing the need of linear search to a minimum,
- (3) converging in fewest iterations.

Chen [1] has developed an effective optimization algorithm suitable for integrated circuit design with the following characteristics: (1) making full use of the evaluated objective function values (OFV) in much the same way that the simplex methods [2] do and (2) estimating a falling direction from current $n + 1$ OFV's and finding a new point with an improved objective function along the falling direction in a manner similar to the Newton's method, rather than blindly taking the reflection point with respect to the center in the simplex methods (SM). Thanks to these features, Chen's method proved to be more effective than other known optimization methods [1]. However, the resort to linear search is still frequent in Chen's method and the amount of iterations is huge. Thus we proposed a new algorithm—POSM. The principal idea lies in finding the minimum point of the pseudo objective functions which are formulated to approximate the exact objective function in a much simpler form without involving complicated calculation instead of looking for the minimum point of the exact objective function by a linear search along a falling direction. Note that the error function can be approximated by a first-, second-, or even higher order polynomial of which the minimum point is easy to find, and a series of optimization methods with various degrees of complexity can be developed accordingly following this idea. Moreover, the modified simplex method in conjunction with a quadratic interpolation scheme is incorporated to further alleviate the necessity of linear search step. The total combination leads to the pseudo objective function substitution method (POSM).

In Section II, the basic concept and a detailed algorithmic procedure of the pseudo objective function substitution method are described. The evaluation results of the proposed algorithm by a few typical optimization problems selected from literature are discussed and com-

Manuscript received August 19, 1986; revised June 15, 1987, March 21, 1988, and June 8, 1988. This work was supported by the Air Force Office of Scientific Research, Boiling Air Force Base, Washington, DC, under Grant AFSOR-86-0339. The review of this paper was arranged by Editor A. J. Strojwas.

G.-L. Tan is with the Department of Electrical and Computer Engineering, University of California at San Diego, La Jolla, CA 92093, on leave from the Department of Electrical Engineering, Beijing Polytechnic University, Beijing, China.

S.-W. Pan is with the Department of Electrical Engineering, Beijing Polytechnic University, Beijing, China.

W. H. Ku and A.-J. Shey are with the Department of Electrical and Computer Engineering, University of California at San Diego, La Jolla, CA 92093.

IEEE Log Number 8822901.

pared with other well-known algorithms in Section III. Section IV presents some circuit design examples illustrating the great suitability of the application of POSM in ADIC for integrated circuit and system design. The final section presents summary and conclusions about this algorithm and comments on its further applicability.

II. ALGORITHM

Generally speaking, the circuit optimization can be performed by successively modifying the parameter vector $x = (x_1, x_2, \dots, x_n)$ until the calculated response $u(x, t)$ comes close to the desired response $r(t)$ within a certain tolerance in the sense of a least p th approximation [3], in short, finding an x such that the objective function $S(x)$ being a minimum

$$S(x) = \sum_{j=1}^m [e_j(x)]^p \quad (1)$$

where p is an even positive integer, m is the number of sampling points, and $e_j(x)$ is the corresponding error function at the j th sampling point, and is defined as

$$e_j(x) = u(x, t_j) - r(t_j), \quad j = 1, 2, \dots, m$$

where t , for example, can be input voltage in dc characterization, frequency in ac analysis, or time in TRANSient evaluation; $u(x, t_j)$ and $r(t_j)$ are the calculated response with parameter vector x and the desired response at the j th sampling point, respectively. The basic assumption of POSM is that e_j can be approximated¹ by

$$e_j = e_j^M + \sum_{i=1}^n b_{ij}(x_i - x_i^M) + \sum_{i=1}^n c_{ij}(x_i - x_i^M)^2, \quad j = 1, 2, \dots, m \quad (2)$$

where the notation e_j is for $e_j(x)$, e_j^M for $e_j(x^M)$, and b_{ij} and c_{ij} are approximation coefficients to be determined. In order to determine these approximation coefficients a super-polygon with $2n + 1$ vertices in n -dimensional parameter space is constructed, and the error function $e_j^k = e_j(x^k)$, and the objective function S^k are evaluated at these vertices ($k = 1, 2, \dots, 2n + 1, j = 1, 2, \dots, m$), from which x^M and x^{\max} , the parameter vectors of the best and worst point, i.e., S^M (S^{\max}) with the smallest (biggest) value, among the $2n + 1$ points can be selected as a reference for updating the super-polygon. Putting these values (e_j^k and e_j^M) into (2), we can formulate a set of $2n$ equations in terms of coefficients b_{ij} and c_{ij} (for each j):

$$\begin{aligned} & w^k(e_j^k - e_j^M) \\ &= w^k \sum_{i=1}^n b_{ij}(x_i^k - x_i^M) + w^k \sum_{i=1}^n c_{ij}(x_i^k - x_i^M)^2, \\ & k = 1, 2, \dots, 2n \end{aligned} \quad (3)$$

¹Here the mixed terms in the Taylor series expansion are neglected for reducing the computation load when calculating those coefficients. Nevertheless, the experimental results do not show high sensitivity to those mixed terms.

where $w^k = (S^k)^{-1/p}$ is the weight of the k th equation [1]. Equation (3) can be expressed in a matrix form

$$w(X|Y) \begin{bmatrix} B_j \\ C_j \end{bmatrix} = E_j \quad (4)$$

where $E = [w^k(e_j^k - e_j^M)]_{2n \times m}$, $X = [x_i^k - x_i^M]_{2n \times n}$, $Y = [(x_i^k - x_i^M)^2]_{2n \times n}$, $B = [b_{ij}]_{n \times m}$, and $C = [c_{ij}]_{n \times m}$. E_j , B_j , and C_j denote column vectors of E , B , and C , respectively. From (4), B_j and C_j can be solved by

$$\begin{bmatrix} B_j \\ C_j \end{bmatrix} = [w(X|Y)]^+ E_j, \quad j = 1, 2, \dots, m \quad (5)$$

where the notation $[]^+$ represents a generalized-inverse operation [4]. Note that we only need to calculate B and C from (5) with generalized-inverse operation once, since $w(X|Y)$ in (5) is independent of j .

Based on the second-order error function approximation, a pseudo objective function \bar{S} corresponding to (1) can be formulated in terms of the Taylor series expansion of $S(x)$ at S^M [5] (see Appendix 4).

$$\begin{aligned} \bar{S}(x^M + \Delta x) &= S^M + p\Delta x^T BR \\ &+ 0.5p(p-1)\Delta x^T BDB^T \Delta x + pY^T CR \\ &+ 0.5p(p-1)Y^T CDC^T Y \\ &+ p(p-1)\Delta x^T BDC^T Y \end{aligned} \quad (6)$$

where

$$\begin{aligned} R &= [(e_1^M)^{p-1}, (e_2^M)^{p-1}, \dots, (e_m^M)^{p-1}] \\ D &= \text{diag} [(e_1^M)^{p-2}, (e_2^M)^{p-2}, \dots, (e_m^M)^{p-2}] \\ Y &= [\Delta x_1^2, \Delta x_2^2, \dots, \Delta x_n^2], \quad B = [b_{ij}]_{n \times m}, \\ C &= [c_{ij}]_{n \times m}. \end{aligned}$$

The minimum point of \bar{S} can be found by equating the derivative of \bar{S} with respect to Δx to zero

$$g(\Delta x) = \frac{\partial \bar{S}(x^M + \Delta x)}{\partial \Delta x} = 0. \quad (7)$$

From (6) we have

$$\begin{aligned} g(\Delta x) &= pBR + p(p-1)BDB^T \Delta x + 2pZCR \\ &+ p(p-1)BDC^T Y \\ &+ 2p(p-1)ZCDB^T \Delta x \\ &+ 2p(p-1)ZCDC^T Y = 0 \end{aligned} \quad (8)$$

where $Z = \text{diag} [\Delta x_1, \Delta x_2, \dots, \Delta x_n]$. Δx can be solved by using a globally convergent modified Newton's method [6], and the parameter vector can be modified by

$$x^{\text{new}} = x^M + \Delta x. \quad (9)$$

Thus the optimum solution x^* of S is further approached by x^{new} . The modified Newton's iteration can be written as

$$\Delta x^{k+1} = \Delta x^k - \lambda [Q(\Delta x^k)]^{-1} g(\Delta x^k) \quad (10)$$

where

$$Q(\Delta x) = \frac{\partial g(\Delta x)}{\partial \Delta x} \\ = p(p-1)BDB^T + 2pV + 2p(p-1)G \quad (11)$$

where $V = \text{diag}[C_1R, C_2R, \dots, C_nR]$, $G = \text{diag}[C_1DC^TY, C_2DC^TY, \dots, C_nDC^TY]$, and λ can be found by backtrack linear search [6] such that

$$S(\Delta x^{k+1}) < S(\Delta x^k) - \alpha\lambda [g(\Delta x^k)]^T \\ [Q(\Delta x^k)]^{-1} \cdot g(\Delta x^k) \quad (12)$$

where $\alpha = 0.0001$ [6]. Note that there is only a simple polynomial calculation rather than a complicated objective function evaluation required for the linear search employed here, which relieves the computation load substantially. Moreover, if the Hessian matrix $Q(\Delta x) = \nabla^2 S(x)$ is nonpositive definite, we can convert it to a positive definite one by substituting $Q(\Delta x)$ by $[Q(\Delta x) + \gamma I]$ ($\gamma \geq 0$) [6] to avoid the possible convergence at the maximum or saddle point.

Once convergence of Newton's iteration is reached, (i.e., x^{new} could be found) we calculate $S^{\text{new}} = S(x^{\text{new}})$ and compare it with S^{max} and S^M .

If $S^{\text{new}} < S^{\text{max}}$, i.e., the current iteration is successful, we update the super-polygon by replacing x^{max} with x^{new} ; further if $S^{\text{new}} < S^M$, we update the super-polygon by replacing x^{max} with x^M and substitute x^{new} for x^M . After

$$\begin{array}{ll} x_i^0(1.02 + \xi), & k = i, & x_i^0 \neq 0, & k \leq n \\ (1.02 + \xi), & k = i, & x_i^0 = 0, & k \leq n \\ x_i^k = x_i^0(0.98 - \xi), & (k - n) = i, & x_i^0 \neq 0, & n < k \leq 2n \\ (0.98 - \xi), & (k - n) = i, & x_i^0 = 0, & n < k \leq 2n \\ x_i^0, & k \neq i, & (k - n) \neq i & \end{array}$$

the reference point x^{max} is determined from the new super-polygon, the next optimization iteration starts until the convergence condition is satisfied. Note POSM only evaluates the objective function once in the successful iteration.

If $S^{\text{new}} > S^{\text{max}}$, the current iteration fails. The remedy for the failure case is a crucial point in this algorithm. If $S^{\text{new}} > S^{\text{max}}$ is the case, we apply the modified simplex method by finding the weighted center \bar{x} of the super-polygon with $2n$ vertices (with x^{max} excluded).²

$$\bar{x} = \frac{1}{SD} \sum_{\substack{k=1 \\ k \neq \text{max}}}^{2n+1} \frac{x^k}{S^k} \quad (13)$$

²Note that the weighted center of the super-polygon is chosen as new reference point in MSM employed here, instead of the geometric center in conventional SM [2].

where

$$SD = \sum_{\substack{k=1 \\ k \neq \text{max}}}^{2n+1} \frac{1}{S^k}.$$

Then a certain reflection point of x^{max} with respect to \bar{x} is chosen as the new point, i.e.,

$$x^{\text{new}} = \bar{x} + \beta(\bar{x} - x^{\text{max}}), \quad \beta \in (0, 1]. \quad (14)$$

If $S^{\text{new}} = S(x^{\text{new}}) < S^M$ or $S^{\text{new}} < S^{\text{max}}$, the same procedure for successful iteration mentioned above can be resumed.

If $S^{\text{new}} > S^{\text{max}}$ still holds, we can apply the quadratic interpolation scheme through the three known points x^{max} , x^M , and x^{new} to find a new point \bar{x}^{new} , since $S^M < S^{\text{max}} < S^{\text{new}}$ in this case. If the value of the objective function at \bar{x}^{new} is smaller than S^{max} , x^{new} is replaced by \bar{x}^{new} . In case $S^{\text{new}} = S(\bar{x}^{\text{new}})$ is still greater than S^{max} , which rarely happens, the minimum point of S may be inside the super-polygon. If this happens, we can shrink the size of the super-polygon to locate the minimum point more accurately [2].

However, based on our experience, the odds of needing to shrink the super-polygon are quite rare. As a result, POSM needs evaluations of objective functions no more than twice for any failed iteration except in some extreme cases.

The algorithm as stated above can be summed up in the following algorithmic procedure:

Algorithm POSM2

(1) Initialize a super-polygon from the $2n + 1$ points picked around the initial point x_i^0 .

where ξ is the spreading coefficient³ used to determine the size of the super-polygon.

(2) Evaluate the error functions $e_j = (j = 1, 2, \dots, m)$ and the objective functions S^k .

(3) Select the point with minimum error $x^M = x^{\text{min}}$ among $2n + 1$ points $\{S^M = S(x^M)\}$.

(4) Determine the point with maximum error x^{max} among $2n + 1$ points $\{S^{\text{max}} = S(x^{\text{max}})\}$.

(5) Calculate pseudo objective function \bar{S} .

(6) Solve Δx using a globally convergent modified Newton method [6], and update $x^{\text{new}} = x^M + \Delta x$.

(7) If the optimization iteration converges, then stop.

(8) If $S^{\text{new}} < S^M$, then update the super-polygon by replacing x^{max} with x^M , substitute x^{new} for x^M , and go to (4).

³Selecting 1.02 and 0.98 instead of 1.0 makes points $x(k = 1, 2, \dots, 2n)$ distribute in a more random way.

(9) If $S^{\text{new}} < S^{\text{max}}$, then update the super-polygon by replacing x^{max} with x^{new} and go to (4).

(10) (In this case, $S^{\text{new}} > S^{\text{max}}$ means the current iteration fails.) Find x^{new} by the modified simplex method (MSM) and calculate $S^{\text{new}} = S(x^{\text{new}})$.

(10.1) If $S^{\text{new}} < S^M$, then update the super-polygon by replacing x^{max} with x^M , substitute x^{new} for x^M , and go to (4).

(10.2) If $S^{\text{new}} < S^{\text{max}}$, then update the super-polygon by replacing x^{max} with x^{new} , and go to (4).

(10.3) Calculate a minimum point x^{new} by quadratic interpolation through the three points $(x^{\text{new}}, S^{\text{new}})$, (x^M, S^M) , and $(x^{\text{max}}, S^{\text{max}})$, then replace x^{new} by x^{new} and calculate $S^{\text{new}} = S(x^{\text{new}})$.

(10.4) If $S^{\text{new}} < S^{\text{max}}$, then go to (8), otherwise go to (11).

(11) Shrink the size of the super-polygon, i.e., calculate [1]

$$x^k = x^M + \frac{(S^M)^{1/p}}{(S^k)^{1/p} + (S^M)^{1/p}} (x^k - x^M).$$

(12) Then go to (2).

Notes:

(1) In step (1), users only need to provide an initial point x^0 . The other $2n$ points will be chosen by moving x along positive and negative directions on each coordinate axis, and the distance is determined by the spreading coefficient. Results show that POSM is not sensitive to the selection of the initial super-polygon.

(2) In step (7), if (1) $|S^{\text{max}} - S^M| \leq \epsilon_1 S^M + \epsilon_2$ and (2) $|x_i^{\text{max}} - x_i^M| \leq \epsilon_1 x_i^M + \epsilon_2$ ($i = 1, 2, \dots, n$), then the iteration stops. Here, ϵ_2 is the absolute error tolerance and ϵ_1 is the relative error tolerance which are given by the user ($\epsilon_2 = \epsilon_1^2 = 10^{-12}$ by default). For the examples in Section III, the stopping criterion is set as $\|g\| < \epsilon_1$ or $|S| < \epsilon_1$ in order to have fair comparisons with the results in [1] and [7].

(3) In step (10.3), the quadratic interpolation function is applied to the three points $(x^{\text{new}}, S^{\text{new}})$, (x^M, S^M) , and $(x^{\text{max}}, S^{\text{max}})$ and yields

$$\begin{aligned} SI(x) &= S^{\text{max}} \frac{(x - x^M)^T (x - x^{\text{new}})}{(x^{\text{max}} - x^M)^T (x^{\text{max}} - x^{\text{new}})} \\ &+ S^M \frac{(x - x^{\text{max}})^T (x - x^{\text{new}})}{(x^M - x^{\text{max}})^T (x^M - x^{\text{new}})} \\ &+ S^{\text{new}} \frac{(x - x^{\text{max}})^T (x - x^M)}{(x^{\text{new}} - x^{\text{max}})^T (x^{\text{new}} - x^M)}. \end{aligned}$$

The minimum point of $SI(x)$ can be expressed as

$$x^{\text{new}} = \frac{(S^{\text{max}}BC + S^{\text{new}}AB)x^M + (S^M AC + S^{\text{new}}AB)x^{\text{max}} + (S^{\text{max}}BC + S^M AC)x^{\text{new}}}{2(S^{\text{max}} + S^M + S^{\text{new}})}$$

where

$$\begin{aligned} A &= (x^{\text{max}} - x^M)^T (x^{\text{max}} - x^{\text{new}}) \\ B &= (x^M - x^{\text{max}})^T (x^M - x^{\text{new}}) \\ C &= (x^{\text{new}} - x^{\text{max}})^T (x^{\text{new}} - x^M) \end{aligned}$$

(4) From a number of examples in the following section, we will find that the case of (11) occurs only when x^M is very close to x^* (the optimal point). In general, if this happens, unless very high accuracy is needed, the iteration can be terminated because the improvement of $|S(x)|$ will be very little if the iteration keeps going.

(5) If Chen's method is employed to calculate Δx , in which a linear approximation of e_j and a second-order approximation of $S(x^M + \Delta x)$ are assumed, and the steps (10) and (11) are adopted for processing the failed iteration instead of Chen's strategy [1], we would call this modified algorithm the first-order POSM (POSM1), and the algorithm mentioned above the second-order POSM (POSM2) (or abbreviated to POSM).

(6) It is evident that the POSM needs at least $2n + 1$ initial objective function calculations, while Chen's method needs only $n + 1$ initial objective function calculations. In order to circumvent this shortcoming a variable order POSM scheme has been proposed in which the first-order POSM is applied in the first n iterations without discarding the replaced points; then the second-order POSM is initialized through the super-polygon formed by the accumulated $2n + 1$ points automatically.

III. NUMERICAL EXAMPLES AND COMPARISONS WITH OTHER ALGORITHMS

First, we will present the computation results of some numerical examples to show the advantage of the high efficiency embodied in the POSM in comparison with other existing methods.

Example 1: Rosenbrock's Parabolic Valley problem ($p = 2$):

$$S = 100(x_2 - x_1^2)^2 + (1 - x_1)^2.$$

The objective function has a minimum value of zero at $(1, 1)$. The initial point is set at $(-1.2, 1)$. The results are listed in Tables I and II, where ΔS is the change of the objective function.

As seen in the results, the POSM is superior to other well known methods in terms of a minimum number of objective function evaluations. Also, it is an obvious advantage that POSM is insensitive to the spreading coefficient ξ .

The objective function and the POSM optimization process are illustrated in Figs. 1 and 2 by showing contours of constant values of objective function and the evaluated variable loci of this example as the optimization proceeds. It is clearly found that the variable loci move downward

towards the local bottom of the objective function valley at the first step, then continuously move along the minimum objective function valley toward the optimal point with fast monotonic decrease in objective function value.

Example 2: Colville's four-dimensional banana prob-

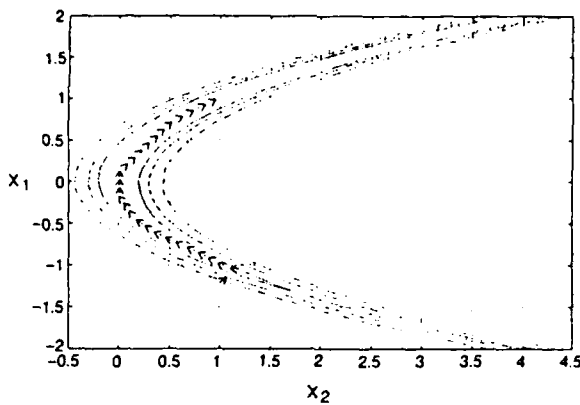


Fig. 1. The objective function contours of Example 1 showing the fast monotonic decrease in objective function value at consecutive optimization steps by POSM; $-$: OFV = 5, $- -$: OFV = 10, \cdots : OFV = 15, $- \cdot -$: OFV = 20.

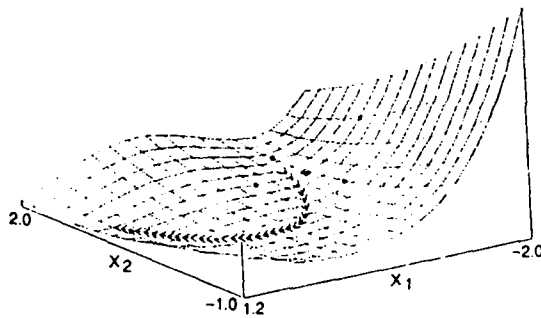


Fig. 2. A three-dimensional plot of variable loci illustrating the optimization path of Rosenbrock's parabolic valley problem by POSM, and * symbols indicating the initial super-polygon.

TABLE I

Method	Stopping Criterion	Ns (Nsg) ‡
Fletcher-Powell	$S < 10^{-12}$	120 - 380*[1]
Jacobson-Oksman	$\Delta S < 10^{-8}$	(39) [1]
Powell	$S < 10^{-8}$	70 [1]
Peckham	$S < 4 \times 10^{-10}$	12 [1]
Hooke-Jeeves	$S < 2 \times 10^{-7}$	353 [7]
Nelder-Mead	$S < 10^{-7}$	300 [7]
Powell	$S < 10^{-14}$	150 - 1500*[7]
Newton	$S < 10^{-13}$	98 [7]
D-S-C	$S < 10^{-7}$	187 [7]
Simplex	$S < 10^{-20}$	133 - 161*
Chen [1]	$S < 10^{-20}$	7 - 135*
POSM	$S < 10^{-20}$	15 - 17*

*Spreading coefficients (ξ) 0.1, 0.4, 1.0, 2.0 are used for these results.
 ‡Ns is the total number of objective function evaluations; Nsg is the total number of objective function calculations and its associated derivatives.

TABLE II

Algorithm	$\xi = 0.1$	0.4	1.0	2.0
Simplex	161	137	133	140
Chen	68	135	71	7
POSM	16	15	17	16

lem ($p = 2$):

$$S = 100(x_1^2 - x_2)^2 + (1 - x_1)^2 + 90(x_3^2 - x_4)^2 + (1 - x_3)^2 + 10.1[(x_2 - 1)^2 + (x_4 - 1)^2] + 19.8(x_2 - 1)(x_4 - 1).$$

Note that this objective function is not an explicit sum of p th error terms in real numbers, but it can be rearranged in a least p th approximation form with $p = 2$ like [1]

$$S = \sum_{j=1}^7 e_j^2$$

where the error terms are defined as

$$\begin{aligned} e_1 &= 10(x_1^2 - x_2) \\ e_2 &= (1 - x_1) \\ e_3 &= \sqrt{90}(x_3^2 - x_4) \\ e_4 &= (1 - x_3) \\ e_5 &= \sqrt{0.2}(x_2 - 1) \\ e_6 &= \sqrt{0.2}(x_4 - 1) \\ e_7 &= \sqrt{9.9}(x_2 + x_4 - 2). \end{aligned}$$

The objective function has a minimum value of zero at (1, 1, 1, 1) and a stationary point at (-0.9679, 0.9471, -0.9695, 0.9512). The evaluation results of POSM with various initial points are summarized in Table III for comparison with other methods.

It is interesting to point out that the POSM2 algorithm has a convergence rate faster than that of any other methods even when the initial point happens to be the nonoptimal stationary point. In addition, the results show that the location of the initial point does not affect the convergence rate much in POSM2.

Example 3: Powell's Function problem ($p = 2$):

$$S = (x_1 + 10x_2)^2 + 5(x_3 - x_4)^2 + (x_2 - 2x_3)^4 + 10(x_1 - x_4)^4.$$

The objective function has a minimum value of zero at (0, 0, 0, 0) where the Hessian matrix is singular. Table IV shows the results calculated by POSM in contrast with those obtained by other methods.

Even though the POSM does not employ an exact second-order formulation by neglecting the mixed terms for reducing the complexity of objective function evaluation in the error function approximation, the performance of the POSM is still superior to other methods, since the results from the preceding examples, where there are mixed terms involved only in the error functions e_3 and e_4 of Example 3, show that the inclusions of the mixed terms in the error function has only a minor influence on the convergence rate. Thus we trade the accuracy in the error function approximation, where higher accuracy in approximation may lead to faster convergence, for a less

TABLE III [1]

Method	Jacobson -Oksman	Fletcher -Powell	Simplex	Chen	POSM
Initial Point	$\ g\ \leq 10^{-4}$	$\ g\ \leq 10^{-4}$	$\Delta S \leq 10^{-4}$	$\ g\ \leq 10^{-6}$	$\ g\ \leq 10^{-6}$
(-3,-1,-3,-1)	135	161	694	26	25
(-3,1,-3,1)	134	595	549	31	26
(-1,2,1,-1,2,1)	194	648	573	107	30
stationary point	fail	fail	382	231	41

TABLE IV [1]

Method	Fletcher -Powell	Jacobson -Oksman	Rank-one	Project- tion	Huang	Chen	POSM
Initial Point	$\ g\ \leq 10^{-4}$	$\ g\ \leq 10^{-4}$	$\ g\ \leq 10^{-6}$				
3,-1,0,1	80	64				28	21
10,10,10,-10			378-925	286-660	172-663	28	43

computation load of objective function evaluation in order to maximize the overall performance.

IV. CIRCUIT DESIGN EXAMPLES

Due to its inherent high efficiency advantage, POSM is highly suitable for applications in the optimization of complicated integrated circuit designs. As a rule, the more complex the IC is the more efficient it appears.

Example 4: AC optimization of a second-order active low-pass filter:

The circuit schematic is shown in Fig. 3 and the input circuit description codes are listed in (1) of Appendix 2.

Fig 4 illustrates the frequency response of the circuit at different optimization stages. As seen, a significant discrepancy exists between the corresponding frequency response (#2) for the initial parameter vector and the desired frequency response (#1). In a few iterations, the intermediate optimized response (#3) has been very close to the desired response. Finally, a fairly good agreement between the desired response and the optimized response (#4) is observed with reasonable optimized parameter values. The quantitative details that include iteration statistics, objective function values, and parameter vectors are listed in Table V and compare with the results obtained by Chen's method [1], (run on IBM 4381, the same hereafter) where the performances are evaluated in terms of the following:

- N_i the number of iterations,
- N_c the number of objective function evaluations,
- N_a the number of additional objective function evaluations while iteration fails, and
- IVOF, FVOF, IPV, FPV stand for initial value and final value of objective function, initial and final parameter vector, respectively,
- p is the order of least p th approximation.

From Table IV, it is found that Chen's method is sensitive to p (large variation on the number of iterations

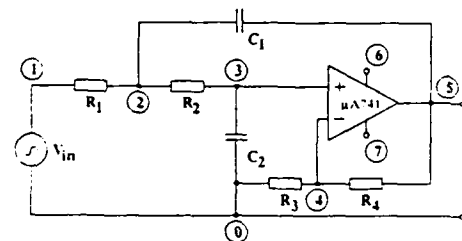


Fig. 3. The circuit schematic of an active low-pass filter.

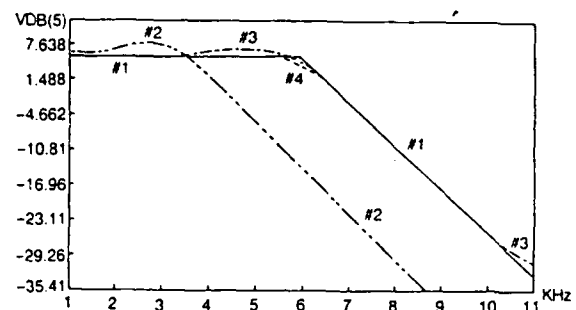


Fig. 4. The simulated frequency responses of the active low-pass filter shown in Fig. 3. #1 the desired ac response; #2 #4 the initial calculated frequency response and the improved frequency responses obtained at successive optimization stages.

with respect to p), while POSM is not, and POSM is more effective than Chen's no matter what the p value is.

Moreover, the final row in Table V shows if linear search (as in Chen's method) is adopted instead of MSM in step (10) in the algorithm POSM2, then the number of iteration and failed iteration increases. It is apparent that the low efficiency inherent in the linear search strategy causes the degradation in the performance of Chen's method.

Example 5: Parameter extraction of MOS device:

Because of technological limitations, the final values of the devices' parameters will not match the design values exactly especially for small size devices. In order to pre-

TABLE V

Method	Ni	Nc	Na	p	IVOF	FVOF	IPV	FPV	CPU time
Chen	43	211	165	2	3.120×10^3	4.29	C1=10U C2=1U	C1=0.82U C2=0.315U	83.37 S
POSM	20	25	0	2	3.120×10^3	0.0987	C1=10U C2=1U	C1=3.02U C2=0.097U	12.37 S
Chen	16	23	4	4	1.736×10^6	0.082	C1=10U C2=1U	C1=3.17U C2=0.095U	11.30 S
POSM	14	19	0	4	1.736×10^6	0.071	C1=10U C2=1U	C1=3.16U C2=0.092U	9.870 S
Chen	34	77	40	6	4.167×10^9	23.98	C1=10U C2=1U	C1=3.481U C2=0.083U	31.34 S
POSM	21	28	2	6	4.169×10^9	0.39	C1=10U C2=1U	C1=3.25U C2=0.094U	13.30 S
POSM*	24	33	4	6	4.169×10^9	0.41	C1=10U C2=1U	C1=3.29U C2=0.091U	14.05 S

*For the handling of iteration failure here, Chen's method is used rather than the Modified Simplex Method as in step (10) of POSM2.

pare a more accurate empirical device model, the devices' effective parameters (e.g., channel length) must be extracted from measured data. To this end, the output characteristics of device are measured first and taken as the given requirement; then the dc optimization is performed.

The circuit for parameter extraction of a MOS device is depicted in Fig. 5, and its input codes are listed in (2) of Appendix 2. The results as compared with those obtained by Chen's method, shown in Table VI, show that if the initial value $L = 10U$ is selected, the number of iterations by Chen's method increases, while the number of iterations in POSM does not change whether $L = 9U$ or $L = 10U$. The results of POSM are not sensitive to the initial value of parameters.

Example 6: Transient characteristic optimization of a circuit simulating a low power position-follow system:

In this example, the objective is to make the rise and fall times of the TR response shorter and its overshoot smaller. The results compared with those obtained by Chen's method are shown in Table VII, and the transient characteristics in Figs. 7-10. The circuit schematic is shown in Fig. 6.

As shown in Table VII, POSM comes up with a better performance than Chen's method, which has very often been involved with linear searching and simplex shrinking, and the number of additional objective function evaluations is enormous. Therefore, POSM is preferable. Initially in this example, the circuit was optimized using POSM with weight as 1 (default value). The output waveform of this optimization as shown in Fig. 8 did not meet the design goal; therefore, the optimization was further carried out interactively by altering the weights (i.e., reducing the weight at the sampling point where the deviation is small and increasing it at the point where the deviation from the desired value is large). For example, the weights of 2nd-6th and 13th-17th points are raised to 10. The optimization process is stopped once the output characteristic comes closest to the desired response. The results are shown in Fig. 9. The initial calculated voltage waveform of $v(21, 0)$ in the circuit as shown in Fig. 10 is

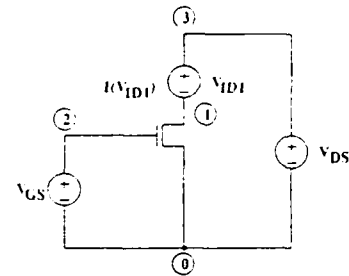


Fig. 5. The MOS circuit used for effective device parameter extraction.

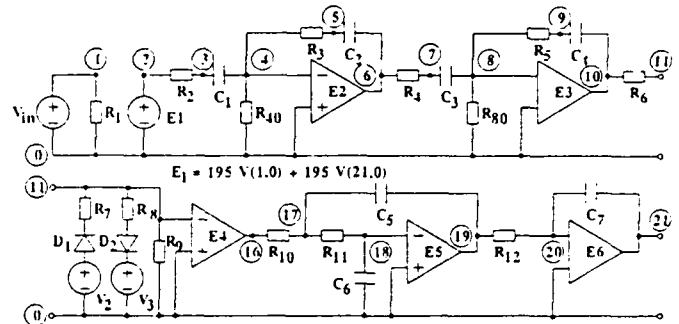


Fig. 6. The equivalent circuit of a low power position-follow system.

TABLE VI

Method	Ni	Nc	Na	IVOF	FVOF	IPV	FPV	CPU time
Chen	8	11	1	1.5287	4.3×10^{-3}	L=9U	L=6.00U	5.86 S
POSM	4	7	0	1.5287	4.3×10^{-3}	L=9U	L=6.00U	4.26 S
Chen	9	12	1	1.5287	4.3×10^{-3}	L=10U	L=6.00U	7.06 S
POSM	4	7	0	1.5287	4.3×10^{-3}	L=10U	L=6.00U	4.24 S

TABLE VII

Method	Ni	Nc	Na	IVOF	FVOF	IPV	FPV	CPU time
Chen	18	76	48	0.2548	0.2398	R2=100k R3=100k R4=50k R5=100k	R2=413K R3=92K R4=50.7K R5=126K	1836 S
POSM with uniform weight 1	18	27	0	0.2548	0.067	R2=400k R3=100k R4=50k R5=100k	R2=411.1K R3=97.7K R4=31.3K R5=99.6K	575 S
POSM with variable weights	17	26	0	7.918	0.2663	R2=400k R3=100k R4=50k R5=100k	R2=679K R3=128.6K R4=16.2K R5=86.6K	389 S

illustrated in Fig. 7. The waveform obtained by Chen's method is shown in Fig. 10. It is evident that the overshoot as well as the rise and fall times are reduced remarkably after POSM optimization application.

Example 7: Optimization of a high-order bandpass filter design

As shown in Fig. 11, the circuit consists of an active 7-order low-pass filter and an active 5-order high-pass filter. The specification of the design requires that the attenuation in stop-band should be greater than 45 dB. There are 22 design parameters assigned. The input circuit de-

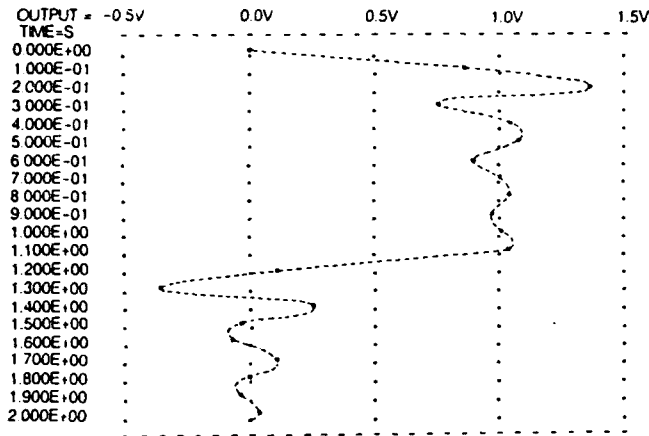


Fig. 7. The initial voltage transient response at $v(0, 21)$ of the circuit shown in Fig. 6.

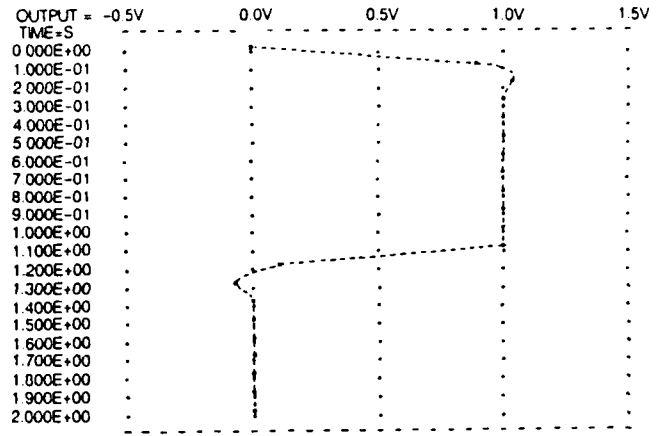


Fig. 9. The optimized transient response at $v(0, 21)$ of the circuit shown in Fig. 6 using the POSM with variable weights.

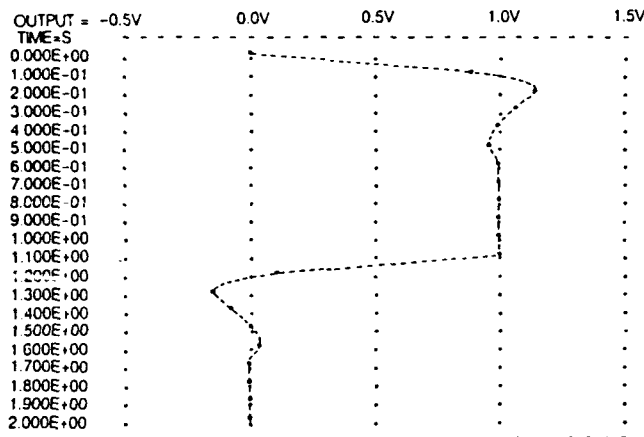


Fig. 8. The optimized transient response at $v(0, 21)$ of the circuit shown in Fig. 6 using the POSM with uniform weights 1's.

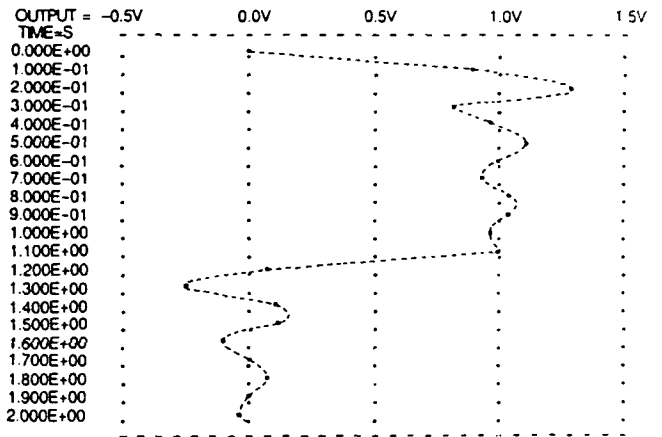


Fig. 10. The optimized transient characteristic calculated by Chen's Method.

scription codes are listed in (4) of Appendix 2. The optimization results are shown in Table VIII.

IPV for both are:

R4 = 100K	R15 = 100K	R28 = 100K
R5 = 100K	R19 = 100K	R29 = 91K
R6 = 80K	R20 = 100K	R30 = 50K
R7 = 10K	R21 = 50K	R34 = 100K
R8 = 50K	R22 = 100K	R35 = 81K
R12 = 100K	R26 = 100K	R36 = 10K
R13 = 100K	R27 = 100K	R37 = 50K
R14 = 50K		

FPV for Chen's method are:

R4 = 157.8K	R15 = -36.3K	R28 = 176.6K
R5 = 144.8K	R19 = 36.52K	R29 = -47.0K
R6 = 41.21K	R20 = 64.57K	R30 = 25.24K
R7 = 8.35K	R21 = 56.05K	R34 = 287.5K
R8 = 46.45K	R22 = 34.57K	R35 = 82K
R12 = 20.6K	R26 = 194.8K	R36 = -9.09K
R13 = 98.32K	R27 = 319.2K	R37 = 159.7K
R14 = 59.03K		

FPV for the POSM are:

R4 = 118.7K	R15 = 30.51K	R28 = 104.9K
R5 = 100.6K	R19 = 126.0K	R29 = 84.59K
R6 = 92.11K	R20 = 124.1K	R30 = 31.79K
R7 = 7.71K	R21 = 8.64K	R34 = 98.98K
R8 = 49.97K	R22 = 90.74K	R35 = 82.71K
R12 = 24.34K	R26 = 90.83K	R36 = 24.99K
R13 = 94.65K	R27 = 97.86K	R37 = 66.44K
R14 = 1000K		

Notice that the results shown in Table VIII by the POSM were summarized from a convergent computer run, whereas those by the Chen's method were extracted from intermediate optimization results, which are not acceptable due to unrealistic resistances because it fails to converge after a long-time computer run.

This fact shows that for large size optimization problems, the POSM basically runs in time proportional to the dimensions of the parameter vector and always obtains convergent results, while, on the contrary, Chen's method often fails to reach a reasonable solution because it easily becomes trapped in the linear searching and simplex shrinking loop.

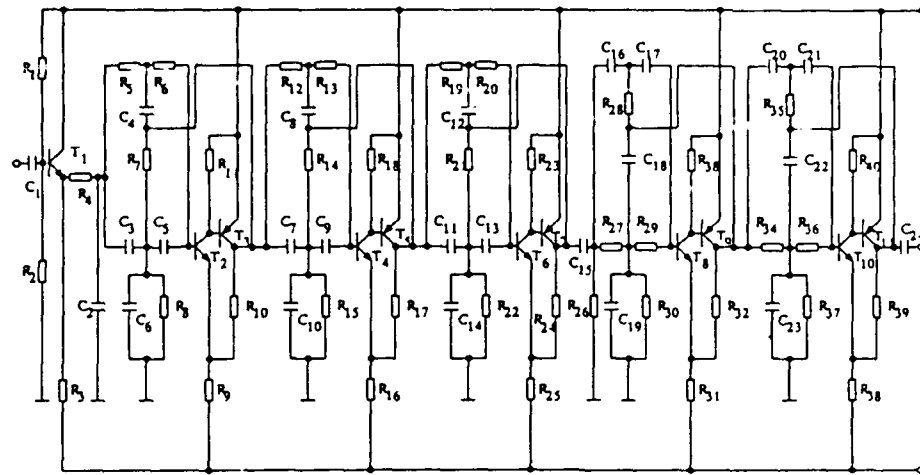


Fig. 11. The circuit diagram of a high-order bandpass filter.

TABLE VIII

Method	Ni	Nc	Na	IVOF	FVOF	CPU Time
POSM	56	101	0	16350	4562	560 S
Chen	131	707	553	16350	5655	2645 S

Example 8: Constrained optimization on the transient response of an inverter chain [8]:

In this example, the signal delay is subjected to minimization under the constraint that transient power is less than 2 mW. The channel lengths of PMOS's and widths of NMOS's are designated as adjustable parameters with a total number of 10. The circuit schematic is shown in Fig. 12. The results are shown in Table IX and the initial and optimized output responses, where the signal delay is reduced from $t_d = 148$ ns to $t_d = 80$ ns, are plotted in Figs. 13-14, respectively.

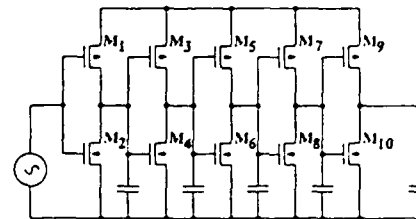


Fig. 12. The circuit schematic of an inverter chain.

V. CONCLUSIONS

We have presented an unconstrained optimization algorithm suitable for integrated circuit design applications. The algorithm has been implemented in the general-purpose analysis and design program for integrated circuit application ADIC. To show the effectiveness and efficiency of this algorithm, we have evaluated it by a number of typical numerical examples which are commonly examined by other existing optimization methods as well as some practical IC designs. As a result, the POSM has proved to be more effective and efficient than other methods in terms of the number of iterations, objective function evaluations, the chance of needing super-polygon shrinkage, and CPU time. The high efficiency is attributed to 1) POSM adopts high order approximations for error function, 2) the modified simplex method is used for handling the failed iteration during optimization, and 3) a globally convergent modified Newton method is used for obtaining the minimum point of \hat{S} . By this sort of combination, POSM reduced both the number of objective function calculations and the chance of shrinking poly-

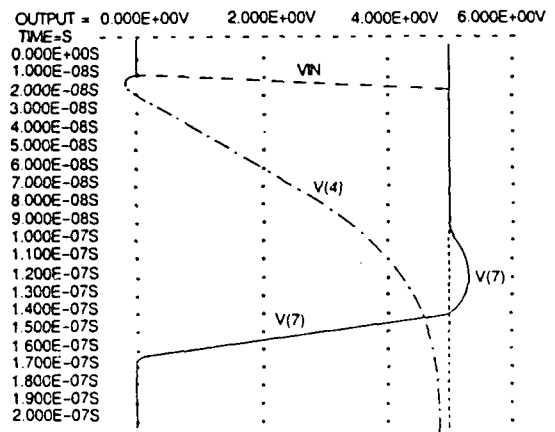


Fig. 13. The initial output response of an inverter chain ($t_d = 148$ ns).

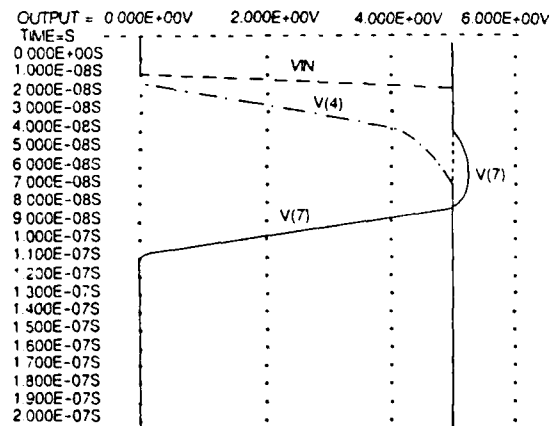


Fig. 14. The optimized output response of an inverter chain ($t_d = 80$ ns).


```

R4 4 5 10K
C1 2 5 10U
C2 3 0 1U
X1 4 3 7 6 5 MACRO OP-UA741
VCC 6 0 DC 15
VEE 7 0 DC -15
VIN 1 0 AC 1
.AC DEC 5 100 10K
.PRINT AC VM(5) VDB(5) VDB(3)
.PLOT AC VDB(5)
.MIN AC OBJT(VDB(5)) W=1 6.054 6.054 6.054 6.054 6.054 6.054,
0.1
+ -0.3955 -7.960 -16.00 -24.05 -32.07 X1=0.5 EPS=0.0001
.PARA C1(100P,20U) C2(100P,10U)
.END

```

In this example, the adjustable parameters are $C1$, $C2$ (.PARAM statement). .MIN statement designates ac optimization; the output to be optimized is $V(5)$; there are 11 sampling points⁶ that are determined by the ac statement, and the weight of every sample point is default value 1 except the sixth point whose weight is 0.1.

The macro-model [11] of $\mu A741$ is included for modeling the operational amplifier in this circuit. $X1 \dots$ MACRO OP-UA471 statement⁷ is used for calling in the macro-model of the $\mu A741$ from the macro-model library and its parameters can be modified during the optimization if they are specified in the .PARAM statement.

(2) MOS Output Characteristics

```

MOS OUTPUT CHARACTERISTICS
.WIDTH IN =80 OUT=80
VDS 3 0
VGS 2 0
X11 1 2 0 SUBTEST1
.SUBCKT SUBTEST1 1 2 4
M1 1 2 4 MOD1 L=10U W 10U
+ AD=10P AS=10P
.MODEL MOD1 NMOS (VTO=-1.5
+UO=550 KP=3.OE-5 NSUB=1.E15
+ LAMBDA=0.02 PHI=0.65)
.ENDS
VID1 3 1
.DC VDS 0 8 .5 VGS 0 4 1
.PRINT DC I(VIDI) V(2)
.PLOT DC I(VIDI)
.MIN DC OBJT(I(VIDI))
+W=1000 0.0 3.16E-5 ... (total 85
+ideal values at sampling points) ...
+X1=0.5 EPS=0.0001
.PARA X11,M1,L(2E-6,20E-6)
.END

```

(3) Transient Characteristics Optimization Example

```

TRANSIENT ANALYSIS EXAMPLE
R1 1 0 1K
R2 2 3 400K
R3 4 5 100K
R4 6 7 50K
R5 8 9 100K
R10 16 17 1.1571MEG
R11 17 18 2.8692K
R12 19 20 1000K
R40 4 0 1E8
R80 8 0 1E8
C1 3 4 1U

```

⁶Here, the sample points are the output points of response $V(5)$.

⁷In ADIC-2.C, the subcircuit calling statement can have real parameters, i.e., "XXXXXXXX N1(N2 N3...)SUBNAM [REAL-PARAMETER]".

```

C2 5 6 1U
C3 7 8 1U
C4 9 10 1U
C5 17 19 1U
C6 18 0 0.1U
C7 20 21 1U
VIN 1 0
+ PULSE(0 1 0 0.10 0.10 1.0 2.2)
E1 2 0
+ POLY(2) 1 0 21 0 0 195 195
E2 0 6 4 0 1E10
E3 0 10 8 0 1E10
E4 16 0 11 0 4.75
E5 19 0 18 0 1
E6 0 21 20 0 1E10
R6 10 11 100K
R7 11 12 10
R8 11 14 10
R9 11 0 100K
V2 0 13 DC 6
V3 15 0 DC 6
D1 13 12 DWY
D2 14 15 DWY
.MODEL DWY D
.TRAN 0.10 2.0 UIC
.PLOT TRAN V(0,21)
.PRINT TRAN V(2) V(4) V(6) V(8)
+ V(11) V(19) V(21)
.MIN TRAN OBJT(V(0,21)) W=1 0 1 1 1
+ 1 1 1 1 1 1 1 0 0 0 0 0 0 0 0
+ X1=0.5 EPS=0.001
.PARA R2 R3 R4 R5
.END

```

(4) A High-Order Filter

```

A HIGH-ORDER FILTER
C1 1 2 30U
R1 3 2 220K
R2 2 0 91K
R3 4 40 15K
Q1 3 2 4 QMOD1
***FIRST***
R4 4 5 100K
R5 5 6 100K
R6 6 9 80K
R7 7 8 10K
R8 8 0 50K
R9 11 0 10K
R10 7 11 51
R11 3 10 10K
C2 5 0 280P
C3 5 8 280P
C4 6 7 250P
C5 8 9 1300P
C6 8 0 110P
Q2 10 9 11 QMOD1
Q3 7 1^ 3 QMOD2
***SECOND***
C7 7 14 438P
C8 12 13 2120P
C9 14 15 1062P
C10 14 0 624P
R12 7 12 100K
R13 12 15 100K
R14 13 14 50K
R15 14 0 50K
R16 18 40 10K
R17 13 18 51
R18 3 16 10K
Q4 16 15 18 QMOD1
Q5 13 16 3 QMOD2
***THIRD***
C11 13 21 638P
C12 19 20 2020P
C13 21 22 1010P
C14 21 0 372P
R19 13 19 100K

```

```

R20 19 22 100K
R21 20 21 50K
R22 21 0 100K
R23 24 40 10K
R24 20 24 50
R25 3 23 10K
Q6 23 22 24 QMOD1
Q7 20 23 3 QMOD2
***FOURTH***
C15 20 25 700P
C16 25 26 700P
C17 26 29 4000P
C18 27 28 60000P
C19 28 0 5000P
R26 25 0 100K
R27 25 28 100K
R28 26 27 100K
R29 28 29 91K
R30 28 0 10K
R31 31 40 10K
R32 27 31 50
R33 3 30 10K
Q8 30 29 31 QMOD1
Q9 27 30 3 QMOD2
***FIFTH***
C20 27 32 4000P
C21 32 35 4000P
C22 33 34 6600P
C23 34 0 1300P
R34 27 34 100K
R35 32 33 18K
R36 34 35 10K
R37 34 0 50K
R38 37 40 10K
R39 33 37 50
R40 3 36 10K
Q10 36 35 37 QMOD1
Q11 33 36 3 QMOD2
C24 33 38 30U
RL 38 0 200K
*****
.MODEL QMOD1 NPN BF=80 VAF=200
+CJE=1P CJC=1P TF=0.1N TR=100N
.MODEL QMOD2 PNP BF=80 VAF=200
+CJE=1P CJC=1P TF=0.1N TR=10N
VIN 1 0 AC
VCC 3 0 DC 12
VEE 40 0 DC -12
.WIDTH IN=80 OUT=80
.AC DEC10 100 20K
.PLOT AC VDB(38)
.MIN AC OBJT(VDB(7), VDB(13),
+ VDB(20),VDB(27),VDB(38))
+W=1 -.52 -.52 -.52 -.52 -.52 -.52
+-.52 -.52 -.52 -.52 -.52 -.52
+-.20 -.40 -.83 -.14.5 -.22.4 -.33.1
+-40.0 -.40.0 -.40.0 -.40.0 -.40.0 -.40.0
+W=1 -.48 -.48 -.48 -.48 -.48 -.48
+-.48 -.48 -.48 -.48 -.53 -.70 -.90
+-1.2 -1.5 -8.7 -26.0 -47.0 -47.0
+-47.0 -47.0 -47.0 -47.0 -47.0 -47.0
+W=1 -.47 -.47 -.47 -.47 -.47 -.47
+-.47 -.47 -.47 -.47 -.50 -.60 -.90
+-1.7 -2.4 -4.0 -50.0 -50.0 -50.0
+-50.0 -50.0 +-50.0 -50.0 -50.0 -50.0
+W=1 -41.3 -41.3 -41.3 -41.3 -41.3
+-41.3 -41.3 -16 -10 -6 -3 -2 -1.3
+-.77 -.38 -2.4 -52 -52 -52 -52
+-52 -52 -52 -52 -52
+W=1 -52 -52 -52 -52 -52 -52 -52
+-21 -4 -.2 -.2 -.2 -.2 -.2 -4 -21
+-52 -52 -52 -52 -52 -52 -52 -52
+-52 XI=0.1 LT=130 ORDER=3
.PARA R4 R5 R6 R7 R8 R12 R13 R19
+R14 (10K, 1000k) R15 (10K, 2000K) R20
+R21 R22 R26 R27 R28 R30 R34 R37
+R29 (10K, 2500K) R35 R36(3K, 2000K)
.END

```

(5) An Inverter Chain

```

CIRCUIT OF INVERTER CHAIN
.WIDTH IN=80 OUT=80
M1 3 2 1 1 MOD1 L=20U W=6U
+ AS=40P AD=20P
M2 3 2 0 0 MOD2 L=6U W=16U
+ AS=30P AD=30P
.MODEL MOD2 NMOS(LEVEL=2 VTO=+1.5
+KP=0.8E-5 LAMBDA=0.02 CGSO=2E-12
+CGDO=2E-12 CGBO=3E-11 NSUB=1E15
+C1=2E-7 TOX=8E-8 XJ=1U LD=0.5U)
CL1 3 0 5E-14
CL2 4 0 5E-14
M3 4 3 1 1 MOD1 L=20U W=6U
+ AS=40P AD=20P
M4 4 3 0 0 MOD2 L=6U W=16U
+ AS=30P AD=30P
M5 5 4 1 1 MOD1 L=20U W=6U
+ AS=40P AD=20P
M6 5 4 0 0 MOD2 L=6U W=16U
+ AS=30P AD=30P
M7 6 5 1 1 MOD1 L=20U W=6U
+ AS=40P AD=20P
M8 6 5 0 0 MOD2 L=6U W=16U
+ AS=30P AD=30P
M9 7 6 1 1 MOD1 L=20U W=6U
+ AS=40P AD=20P
M10 7 6 0 0 MOD2 L=6U W=16U
+ AS=30P AD=30P
.MODEL MOD1 PMOS (LEVEL=2 VTO=-1.5
+ KP=0.4E-5 LAMBDA=0.02 CGSO=2E-12
+CGDO=2E-12 CGBO=3E-11 NSUB=1E15
+ CJ=2E-7 TOX=8E-8 XJ=1U LD=0.5U)
CL3 5 0 5E-14
CL4 6 0 5E-14
CL5 7 0 5E-14
VDD 1 0 DC 5
VIN 2 0 PWL(0 0 10N 0 20N 5 200N 5)
.PLOT TRAN V(3) V(4) V(5) V(6) V(7)
.TRAN 10NS 200NS
.MIN TRAN OBJT(V(3), V(4), V(5), V(6),
+ V(7)) XI=0.3 P=4
+W=5 5 5 0 0 0 (21 points) 0 0 0 0 0
+W=4 0 0 5 5 5 (21 points) 5 5 5 5 5
+W=3 5 5 0 0 0 (21 points) 0 0 0 0 0
+W=2 0 0 5 5 5 (21 points) 5 5 5 5 5
+W=1 5 5 0 0 0 0 0 0 0 0 0 0 0 0
+0 0 0 0 0 CONT(PW*(2^M/W))
.PARA M1,L(5U,40U) M2,W(5U,40U)
+ M3,L(5U,40U) M4,W(5U,40U)
+ M5,L(5U,40U) M6,W(5U,40U)
+ M7,L(5U,40U) M8,W(5U,40U)
+ M9,L(5U,40U) M10,W(5U,40U)
.END

```

APPENDIX 3

THE EXTENSION OF POSM TO CONSTRAINED OPTIMIZATION APPLICATIONS

The optimization problems encountered in the field of circuit and system design are generally cataloged as the constrained optimization type. By using the Lagrange multiplier method (the *PHR* algorithm in [10]), a constrained optimization problem can always be decomposed to a series of unconstrained problems.

The following algorithm summarizes the proposed procedures to deal with the constrained optimization problems by employing the *PHR* method.

(1) Select a nondecreased sequence of $\{\mu^{(k)}\}$ of penalty function factors and initialize the process by setting initial point x^0 , initial multiplier $\lambda^{(1)}$, error tolerance ϵ , and $k = 1$.

(2) Use the proposed unconstrained optimization algorithm POSM2 to solve the decomposed unconstrained optimization problem ((A2) in Appendix 1).

(3) Update multiplier by

$$\begin{aligned}\lambda_i^{(k+1)} &= \lambda_i^{(k)} + \mu^{(k)} \max \{L_i(x^k), -\lambda_i^{(k)}/\mu^{(k)}\} \\ &= \max \{0, \lambda_i^{(k)} + \mu^{(k)}L_i(x^k)\}, \\ & \quad i = 1, 2, \dots, I.\end{aligned}\quad (A3)$$

(4) IF

$$\sum_{i=1}^I [\max \{L_i(x^k), -\lambda_i^{(k)}/\mu^{(k)}\}]^2 < \epsilon^2. \quad (A4)$$

THEN STOP (x^k is the approximation solution of the problem)

ELSE $k = k + 1$, GO TO (2).

APPENDIX 4

THE DERIVATION OF $\tilde{S}(x)$

Let $\Delta x_i = x_i - x_i^M$, and based on the second-order error function approximation the objective function can be written in implicit sum notation as

$$\begin{aligned}S(x) &= \sum_{j=1}^m [e_j(x)]^p \\ &= \sum_{j=1}^m (e_j^M + b_{ij}\Delta x_i + c_{ij}\Delta x_i^2)^p.\end{aligned}$$

This equation can be expanded into binomial series like

$$\begin{aligned}S(x) &= \sum_{j=1}^m \left\{ (e_j^M)^p + p(e_j^M)^{p-1}(b_{ij}\Delta x_i + c_{ij}\Delta x_i^2) \right. \\ & \quad \left. + \frac{p(p-1)}{2!} (e_j^M)^{p-2} \right. \\ & \quad \left. \cdot (b_{ij}\Delta x_i + c_{ij}\Delta x_i^2)^2 + \dots \right\} \\ &= S^M + \sum_{j=1}^m \left\{ p(e_j^M)^{p-1} b_{ij} + p(e_j^M)^{p-1} c_{ij}\Delta x_i^2 \right. \\ & \quad \left. + 0.5p(p-1)(e_j^M)^{p-2} b_{ij}\Delta x_i b_{ij}\Delta x_i \right. \\ & \quad \left. + 0.5p(p-1)(e_j^M)^{p-2} c_{ij}^2 \Delta x_i^2 \right. \\ & \quad \left. + p(p-1)(e_j^M)^{p-2} b_{ij}\Delta x_i c_{ij}\Delta x_i^2 + \dots \right\}.\end{aligned}$$

Neglecting the higher order terms, we can express $\tilde{S}(x)$ in a more compact form as

$$\begin{aligned}S(x) &= S^M + p\Delta x^T B R + 0.5p(p-1)\Delta x^T B D B^T \Delta x \\ & \quad + pY^T C R + 0.5p(p-1)Y^T C D C^T Y \\ & \quad + p(p-1)\Delta x^T B D C^T Y.\end{aligned}\quad (A5)$$

If the Taylor series expansion is assumed, the objective function will be

$$\begin{aligned}S(x) &= \sum_{j=1}^m (e_j^M + b_{ij}\Delta x_i + c_{ij}\Delta x_i^2)^p \\ &\cong S^M + \frac{\partial S}{\partial x_i} \Big|_{\Delta x=0} \Delta x_i + \frac{1}{2} \frac{\partial^2 S}{\partial x_i \partial x_i} \Big|_{\Delta x=0} \Delta x_i \Delta x_i \\ &= S^M + \frac{\partial S}{\partial e_j} \frac{\partial e_j}{\partial x_i} \Big|_{\Delta x=0} \Delta x_i + \frac{1}{2} \left(\frac{\partial S}{\partial e_j} \frac{\partial^2 e_j}{\partial x_i \partial x_i} \right. \\ & \quad \left. + \frac{\partial^2 S}{\partial e_j^2} \frac{\partial e_j}{\partial x_i} \frac{\partial e_j}{\partial x_i} \right) \Big|_{\Delta x=0} \Delta x_i \Delta x_i \\ &= S^M + \sum_{j=1}^m p e_j^{p-1} (b_{ij} + 2c_{ij}\Delta x_i) \Big|_{\Delta x=0} \Delta x_i \\ & \quad + \frac{1}{2} \sum_{j=1}^m p e_j^{p-1} 2c_{ij} \delta_{ij} \Big|_{\Delta x=0} \Delta x_i \Delta x_i \\ & \quad + \frac{1}{2} \sum_{j=1}^m p(p-1) e_j^{p-2} (b_{ij} + 2c_{ij}\Delta x_i) \\ & \quad \cdot (b_{ij} + 2c_{ij}\Delta x_i) \Big|_{\Delta x=0} \Delta x_i \Delta x_i \\ &= S^M + p\Delta x^T B R + 0.5p(p-1) \\ & \quad \cdot \Delta x^T B D B^T \Delta x + pY^T C R\end{aligned}\quad (A6)$$

where δ_{ij} is Dirac δ function. (A5) is identical to (A6) except for the inclusion of two additional high order terms which usually do not introduce too much difference and little improvement on approximation. Thus we adopted (A5) rather than (A6) in this algorithm for more accurate approximation.

ACKNOWLEDGMENT

The authors would like to acknowledge helpful discussions with Yan-Jun Liu, Min-Qiang Wang, and Ping Tang. The authors are grateful to C. Payne and K. Zirk for manuscript preparations and proofreading.

REFERENCES

- [1] R. M.-M. Chen, "A least p th optimization algorithm without calculating derivatives," *IEEE Trans. Circuits Syst.*, vol. CAS-28, pp. 331-337, Apr. 1981.
- [2] J. A. Nelder and R. Mead, "A simplex method for function minimization," *Comput. J.*, vol. 7, pp. 308-313, Jan. 1965.
- [3] G. C. Temes and D. Y. F. Zai, "Least p th approximation," *IEEE Trans. Circuit Theory*, vol. CT-16, pp. 235-237, May 1969.
- [4] R. M.-M. Chen, "New matrix inversion algorithm based on exchange method," *IEEE Trans. Comput.*, vol. C-22, pp. 885-890, Oct. 1973.
- [5] Gen-Lin Tan, Yang Sheng, and Bing-Ren Lu, "A novel optimization algorithm," *Acta Electronica Sinica*, vol. 14, no. 4, pp. 91-96, 1986.
- [6] J. E. Dennis, Jr., *Numerical Methods for Unconstrained Optimization and Nonlinear Equations*. Englewood Cliffs, NJ: Prentice-Hall, 1983.
- [7] D. M. Himmelblan, *Applied Nonlinear Programming*. New York: McGraw-Hill, 1972.
- [8] S. R. Nassif, A. J. Strojwas, and S. W. Director, "A methodology for worst-case analysis of integrated circuits," *IEEE Trans. Computer-Aided Design*, vol. CAD-5, pp. 104-112, Jan. 1986.
- [9] "General Purpose Circuit Analysis and Design Program ADIC-2.C User's Manual," Institute of CAD, Beijing Polytechnic University, 1986.
- [10] D. P. Bertsekas, *Constrained Optimization and Lagrange Multiplier Methods*. New York: Academic, 1982.

- [11] G. R. Boyle, B. M. Cohn, and D. O. Pederson, "Macromodeling of integrated circuit operational amplifiers," *IEEE J. Solid-State Circuits*, vol. SC-9, pp. 353-364, Dec. 1974.



Gen-Lin Tan graduated from Department of Engineering Physics, Qinghua University, China, in 1961. Since then he has been engaged in teaching and research at the Department of Electrical Engineering, Beijing Polytechnic University, Beijing, China, where he is now a Professor.

His research concerns microcomputer application, circuit analysis and optimization, and semiconductor device simulation. He is the author or co-author of several technical papers and three books. He has been with University of California,

San Diego, as a visiting scholar since 1987. His current research interests include simulation of III-V compound semiconductor device and integrated circuit and layout optimization of IC design.



Shao-Wei Pan received the B.S. degree in the electrical engineering from Beijing Institute of Posts and Telecommunications in 1982 and the M.S. degree in electrical engineering from Beijing Polytechnic University, Beijing, in 1986. He is currently a student for Ph.D. in the Department of Electrical and Computer Engineering, University of Wisconsin-Madison.

From 1982 to 1984, he worked at Research Institute of Semiconductor, Ministry of P. and T., China. From 1986 to 1987, he was on the faculty

of electrical engineering at Beijing Polytechnic University. His research interests include computer-aided design and simulation of VLSI circuits.



Walter H. Ku received the B.S. degree (with Honors) in electrical engineering from the Moore School of Electrical Engineering, University of Pennsylvania, Philadelphia, in 1957, and the M.S. and Ph.D. degrees in electrical engineering from the Polytechnic Institute of Brooklyn, N.Y., in 1958 and 1962, respectively. From 1957 to 1960, he held a Research Fellowship at the Polytechnic Institute of Brooklyn.

From 1962 to 1969, Dr. Ku was with the Applied Research Laboratory (ARL) of the GT&E

Sylvania Electronic Systems, Waltham, MA. He joined the faculty of the School of Electrical Engineering of Cornell University, Ithaca, New York, in 1969, and was Professor of Electrical Engineering. In 1973-74, he was on leave from Cornell and was a Visiting Associate Professor at the Department of Electrical Engineering and Computer Sciences of the University of California, Berkeley. For the 1977 academic year, he was on sabbatical leave from Cornell University and was the first occupant of the Naval Electronic Systems Command (NAVELEX) Research Chair Professorship at the Naval Postgraduate School, Monterey, California. For the 1983-1984 academic year, he was the Distinguished Visiting Professor in the Department of Electrical Engineering and Computer Sciences of the University of California, San Diego (UCSD), La Jolla, CA. Since September 1985, Dr. Ku has been Professor of Electrical and Computer Engineering at UCSD, and is currently directing a research group in Electronic Systems and VLSI. His current research interests are in the areas of design and fabrication of submicron gate-length MOS and GaAs FETs, HEMTs and heterojunction bipolar transistors, integrated circuit design and digital signal processing (DSP) algorithms, chip architectures, and gigabit logic.

Dr. Ku was an Associate Editor of the *IEEE TRANSACTIONS ON CIRCUITS AND SYSTEMS*, the co-chairman of the technical committee on optical, microwave and acoustical circuits of the *IEEE Circuits and Systems Society*, and a co-chairman of the technical committee on computer-aided design of the *IEEE Microwave Theory and Techniques Society*. He is presently an Associate Editor of the *JOURNAL OF THE FRANKLIN INSTITUTE* and member of the editorial board of the *IEEE TRANSACTIONS ON MICROWAVE THEORY AND TECHNIQUES*. He is a member of the *IEEE Defense R&D Committee*. He is also a member of Eta Kappa Nu, Tau Beta Pi, Sigma Tau, Phi Tau Phi and Sigma Xi.



An-Jui Shey received the B.S. and M.S. degrees in electronic engineering from the National Chiao Tung University, Hsinchu, Taiwan, in 1979 and 1981, respectively. He is now working toward the Ph.D. degree at the University of California, San Diego.

In the summer of 1984, he held a position at TRW, working in the area of VLSI digital design. Currently, he is engaged in the development of CAD tools for GaAs device and integrated circuit design.